

# **Imaging, Scattering, and Spectroscopic Systems for Biomedical Optics: Tools for Bench Top and Clinical Applications**

By

William J. Cottrell

Submitted in Partial Fulfillment  
of the  
Requirements for the Degree  
Doctor of Philosophy

Supervised by  
Professor Thomas H. Foster

The Institute of Optics  
The College  
School of Engineering and Applied Sciences

University of Rochester  
Rochester, New York

2008

*To my friends and family...*

## Curriculum Vitae

William J. Cottrell was born in Burlington, VT on March 13, 1978. He attended the University of Rochester as a Rush Rhees Scholar from 1996 to 2000, and graduated with a Bachelor of Science in Optics in 2000. Immediately following graduation, he worked for TeraComm Research, Inc., developing advanced transceiver technologies for the telecommunications and defense industries. In 2002, he returned to the University of Rochester and continued studies at The Institute of Optics. He pursued research in biomedical optics under the guidance and direction of Professor Thomas H. Foster. He was supported by a National Institutes of Health training grant from 2004 to 2007 and received a Master of Science degree in Optics in 2004.

## Publications

### Peer-reviewed

Wang K.K.-H., Cottrell W.J., Mitra S., Oseroff A.R., and Foster T.H. (2008). Simulations of measured photobleaching kinetics in human basal cell carcinomas suggest blood flow reductions during ALA-PDT. *Phys. Med. Biol.* (submitted).

Cottrell W.J., Paquette A.D., Keymel K.R., Foster T.H., and Oseroff A.R. (2008). Irradiance-dependent photobleaching and pain in  $\delta$ -aminolevulinic acid-photodynamic therapy of superficial basal cell carcinomas. *Clin. Cancer Res.* **14**: 4475-4483.

Hak Won J., Cottrell W.J., Foster T.H., and Yule D.I. (2007).  $\text{Ca}^{2+}$  release dynamics in parotid and pancreatic exocrine acinar cells evoked by spatially limited flash photolysis. *Am. J. Physiol. Gastrointest. Liver Physiol.* **293**: G1166-G1177.

Cottrell W.J., Wilson J.D., and Foster T.H. (2007). Microscope enabling multimodality imaging, angle-resolved scattering, and scattering spectroscopy. *Opt. Lett.* **32**: 2348-2350.

Wilson J.D., Cottrell W.J., and Foster T.H. (2007). Index of refraction-dependant sub-cellular light scattering observed with organelle-specific dyes. *J. Biomed. Opt.* **12**: 014010.

Cottrell W.J., Oseroff A.R., and Foster T.H. (2006). Portable Instrument that integrates irradiation with fluorescence and reflectance spectroscopies during clinical photodynamic therapy of cutaneous disease. *Rev. Sci. Instrum.* **77**: 064302.

### Conference Proceedings

Cottrell W.J., Oseroff A.R., and Foster T.H. (2006). System for providing simultaneous PDT delivery and dual spectroscopic monitoring in clinical basal cell carcinoma therapy. *Proc. SPIE.* **6139**: 613918.

## **Conference Presentations**

Cottrell W.J., Oseroff A.R., and Foster T.H. Fluorescence and reflectance spectroscopies inform the choice of optimal treatment parameters in a clinical trial of ALA-PDT in superficial basal cell carcinoma. Photonics West BiOS, January 20-25, 2007, San Jose, CA. Book of Abstracts, p. 56.

Cottrell W.J., Wilson J.D., and Foster T.H. Scattering spectroscopy with novel darkfield microscope instrumentation. Optical Society of America Annual Meeting, October 8-12, 2006, Rochester, NY. Conference Program, p. 106.

Cottrell W.J., Oseroff A.R., and Foster T.H. System for providing simultaneous PDT delivery and dual spectroscopic monitoring in clinical basal cell carcinoma therapy. Photonics West BiOS, January 21-26, 2006, San Jose, CA. Book of Abstracts, p. 239.

Cottrell W.J., Oseroff A.R., and Foster T.H. Spectroscopic monitoring during ALA-PDT of human basal cell carcinoma. 11th Congress of the European Society for Photobiology, September 3-8, 2005, Aix-les-Bains, FR. Programme, p. 39.

Cottrell W.J., Oseroff A.R., and Foster T.H. Photodynamic therapy dosimetry by fluorescence and reflectance spectroscopies. Poster presentation. The 88th Optical Society of America Annual Meeting, October 10-14, 2004, Rochester, NY. Conference Program, p. 72.

Cottrell W.J., Oseroff A.R., and Foster T.H. Compact system for simultaneous PDT delivery and dual spectroscopic monitoring. Poster presentation. 32nd Annual Meeting of the American Society for Photobiology, July 10-14, 2004, Seattle, WA. Book of Abstracts, p. 47.

## **Published patent applications**

US20070282404      Side-firing linear optic array for interstitial optical therapy  
WO/2007/120678A2: and monitoring using compact helical geometry.

WO/2006/025940A2: Photodynamic therapy with spatially resolved dual spectroscopic monitoring.

## **Grants**

Packaged side-firing fiber-optic probe for interstitial photodynamic therapy with radial-resolved spectroscopies. NSF/DARPA Photonics Technology Access Program, 2005, \$10,000.

Packaged MEMS for photodynamic therapy instrumentation using dual spectroscopy. NSF/DARPA Photonics Technology Access Program, 2004, \$10,000.

# Acknowledgements

I would like to acknowledge the many people whose support throughout the last several years has made this thesis possible.

First, I would like to thank my thesis advisor, Professor Thomas H. Foster. I have been extremely fortunate to have had the opportunity to work with someone whose research interests span physics, medicine, and biology and who continually finds innovative synergies between these disciplines. He shows an uncommon attention to his students and has guided many aspects of my own graduate and personal development. He has always demanded my highest level of performance and allowed me to build on my strengths while bolstering my weaknesses.

I would also like to give my sincere thanks to Dr. Allan R. Oseroff at Roswell Park Cancer Institute. Allan has been pivotal to the research presented in Chapters 2 and 3 of this thesis. In addition to allowing access to his patients, his knowledge about photodynamic therapy and engineering has played an important role in the success of this research and steering my graduate studies.

There have been several graduate students in the Foster Lab who have made a range of contributions to the research presented here and have offered daily insight and support. Specifically, I would like to thank Jarod Finlay, Chad Bigelow, Soumya Mitra, Jeremy Wilson, Tammy Lee, and Ken Kang-Hsin Wang. Chapter 2 of this thesis builds on fundamental groundwork developed by Jarod in his research at the Foster Lab. The work presented here brings that research from bench top to bedside. Chad similarly provided specific optical knowledge and contributions useful in engineering all the systems presented in this thesis. In addition, Soumya's detailed knowledge of biology and biophysics, as well as his day-to-day experimental insights, were extremely helpful in making experimental progress. I had the privilege of working closely with Jeremy on the instrumentation presented in Chapter 4 of this thesis. His intuitive understanding of scattering phenomena drove the architecture and design specifications, while his pragmatic suggestions kept implementations simple. Ken has developed very rigorous biophysical and pharmacokinetic models which have also provided deep insight into the clinical data presented in Chapter 3 and which will undoubtedly drive future clinical experimentation and analyses. I am very grateful to Tammy, who has enthusiastically picked up the clinical research started in this thesis and is working to improve system functionality, clinical acceptance, and its range of application. I would also like to thank Benjamin Giesselman who provided cell culture and biological support



and David Conover, whose initial and continued guidance in machining and electronics supported the realization of the instrumentation presented here.

There have been a number of collaborators outside of the Foster Lab who deserve recognition as well. Several individuals contributed to the clinical work at Roswell Park Cancer Institute. In addition to the leadership of Dr. Allan Oseroff, I would like to thank Kenneth Keymel, who provided engineering suggestions for the clinical instrumentation and supported it in the clinic. Additionally, I would like to thank Anne Paquette and Sari Fein, who helped drive the interface and probe designs of the instrumentation in Chapters 2 and 3. They were also responsible for treating and monitoring the patients included in these studies, which they did with great care.

At the University of Rochester, I would like to thank Professor David Yule. He provided innovative concepts for the focal photolysis instrumentation presented in Chapter 5 and, along with postdoctoral student Jong Hak Won, designed and implemented experiments around the capabilities of that instrumentation.

I also gratefully acknowledge the financial support of the National Institutes of Health, without which none of this research would have been possible.

Specifically, the work presented in this thesis was supported by NIH grants P01 CA55719, CA122093, and T32 HL66988.

Finally, I need to thank my family and my friends, to whom this thesis is dedicated. I would not have been able to complete this work without the full support of my parents, Dr. Peter and Patricia Cottrell and the encouragement of my sisters, Dr. Caroline Cottrell and Dr. Elizabeth Stevenson. They have always put their faith in me and buoyed my spirits when I needed it most. To the many unmentioned friends and unsung supporters, I thank you.

# Abstract

Optical advances have had a profound impact on biology and medicine. The capabilities range from sensing biological analytes to whole animal and subcellular imaging and clinical therapies. The work presented in this thesis describes three independent and multifunctional optical systems, which explore clinical therapy at the tissue level, biological structure at the cell/organelle level, and the function of underlying fundamental cellular processes.

First, we present a portable clinical instrument for delivering  $\delta$ -aminolevulinic acid photodynamic therapy (ALA-PDT) while performing noninvasive spectroscopic monitoring *in vivo*. Using an off-surface probe, the instrument delivered the treatment beam to a user-defined field on the skin and performed reflectance and fluorescence spectroscopies at two regions within this field. The instrument was used to monitor photosensitizer fluorescence photobleaching, fluorescent photoproduct kinetics, and blood oxygen saturation during a clinical ALA-PDT trial on superficial basal cell carcinoma (sBCC). Protoporphyrin IX and photoproduct fluorescence excited by the 632.8 nm PDT treatment laser was collected between 665 and 775 nm. During a series of brief treatment interruptions at programmable time points, white-light reflectance spectra

between 475 and 775 nm were acquired. Fluorescence spectra were corrected for the effects of absorption and scattering, informed by the reflectance measurements, and then decomposed into known fluorophore contributions in real time using a robust singular-value decomposition fitting routine. Reflectance spectra additionally provided information on hemoglobin oxygen saturation.

We next describe the incorporation of this instrument into clinical trials at Roswell Park Cancer Institute (Buffalo, NY). In this trial we examined the effects of light irradiance on photodynamic efficiency and pain. The rate of singlet-oxygen production depends on the product of irradiance and photosensitizer and oxygen concentrations. High irradiance and/or photosensitizer levels cause inefficient treatment from oxygen depletion in preclinical models. This trial established the irradiance-dependence of patient tolerability to ALA-PDT of sBCC and a pain-threshold irradiance, below which patients did not experience significant pain or require anesthetic. The irradiance-dependence of sensitizer photobleaching was also used to determine an optimal irradiance that maximized treatment efficiency. The optimal fluence at a single low irradiance is yet to be determined.

We additionally report the design, construction, and initial characterization of two optical systems used for cellular scattering measurements: a forward scattering white-light spectroscopy system used to characterize lysosomal refractive index and a multifunctional scattering and fluorescence microscope that exploited an angle-resolved forward-scattering geometry. The multifunctional scattering and fluorescence microscope employed brightfield, Fourier-filtered darkfield, direct imaging of the Fourier plane, angle-resolved scattering, and white-light scattering spectroscopy while preserving a fluorescence imaging channel.

Lastly, we report on the development of a microscope-based system used for high-powered, focal laser photolysis. This system was used with cell-permeable caged messenger molecules and analyte specific fluorophores to provide local stimulation of intact cells and subsequent analyte monitoring. This provided a high-precision, non-invasive means for studying  $\text{Ca}^{2+}$  dynamics between cell types and between sub-cellular regions within a single cell type. The resulting studies compared the mechanisms underlying the  $\text{Ca}^{2+}$  signal globalization in these individual exocrine cell types and under regional messenger release.

# Table of Contents

1	Introduction.....	1
1.1	Introduction to photodynamic therapy .....	4
1.1.2	Photophysical and photochemical kinetics.....	8
1.1.3	Implicit PDT dosimetry.....	10
1.1.4	ALA-PDT .....	11
1.1.5	Optical properties of tissue.....	16
1.2	Introduction to cellular scattering.....	22
1.3	Introduction to fluorescence calcium monitoring.....	27
1.3	References.....	33
2	Portable instrumentation for photodynamic therapy of cutaneous disease .....	44
2.1	Introduction.....	44
2.2	Methods and instrumentation .....	49
2.2.1	Instrument specification .....	52
2.2.2	Probe specification .....	53
2.2.3	Switch design.....	56
2.2.4	System control and operation .....	60
2.2.5	System upgrades.....	62
2.3	Data analysis .....	63
2.3.1	Reflectance .....	63
2.3.2	Nonlinear fitting of reflectance data.....	65
2.3.2.1	Monte Carlo for arbitrary absorption and scattering .....	66
2.3.2.2	Iterative fitting algorithm .....	71
2.3.2.2	Sampling depth.....	75
2.3.3	Fluorescence .....	77
2.4	Discussion.....	84
2.5	References.....	89

3	Clinical assessment of irradiance-dependent photobleaching and pain in $\delta$ -aminolevulinic acid-photodynamic therapy of superficial basal cell carcinoma.....	94
3.1	Introduction.....	94
3.2	Materials and methods.....	97
3.2.1	Patients .....	97
3.2.2	ALA administration.....	98
3.2.3	Irradiation .....	98
3.2.4	Pain assessment .....	99
3.2.5	Clinical follow up.....	101
3.2.6	Instrumentation.....	101
3.2.7	Data analysis.....	102
3.2.8	Statistics.....	103
3.3	Results.....	105
3.3.1	Lesions and patients .....	105
3.3.2	PpIX photobleaching.....	105
3.3.3	Pain .....	107
3.3.4	Reflectance .....	117
3.4	Discussion.....	123
3.5	References.....	134
4	Multi-modality imaging and scattering spectroscopy .....	139
4.1	Introduction.....	139
4.2	Darkfield microscope scattering spectroscopy for subcellular observation.....	140
4.2.1	Darkfield scattering spectrometer instrumentation .....	140
4.2.2	Sample preparation and measurement.....	142
4.2.3	Analysis .....	143
4.2.4	Experimental verification .....	145
4.2.4	Discussion.....	148
4.3	Inverted scattering microscope .....	149
4.3.1	Instrumentation.....	149
4.3.2	Results .....	158
4.3.3	Design considerations.....	164
4.3.4	Discussion.....	169
4.4	References.....	171

5	Focal flash photolysis instrument for <i>in vitro</i> $\text{Ca}^{2+}$ release studies .....	174
5.1	Introduction.....	174
5.2	Materials and methods.....	176
5.2.1	Design and characterization of focal laser photolysis instrument.....	176
5.2.2	Experimental setup .....	184
5.3	Results.....	186
5.4	Discussion.....	189
5.5	References.....	191



# List of Tables

Table 3.1	The $D_{80}$ fluence and $T_{80}$ time required for each of the low-irradiance groups to bleach PpIX by 80%.....	112
Table 3.2	Irradiance-dependent pain experienced during ALA-PDT of sBCC .....	114
Table 3.3	Likely PDT treatment depth compared to sampling depths of reflectance and fluorescence spectroscopies .....	129
Table 4.1	Optical prescription for the scattering microscope.....	168
Table 5.1	Optical prescription for focal flash photolysis system .....	180

# List of Figures

Figure 1.1	Jablonski diagram of photodynamic therapy photochemistry .....	9
Figure 1.2	Excitation and emission spectra of PpIX in EMT6 cells.....	13
Figure 1.3	Biosynthetic pathway for the production of PpIX from ALA.....	15
Figure 1.4	Reduced scattering spectrum in tissue.....	20
Figure 1.5	Absorption spectra for oxyhemoglobin, deoxyhemoglobin, water, and melanin.....	21
Figure 1.6	Cellular processes that regulate the increase and decrease of $[Ca^{2+}]_i$ .....	29
Figure 2.1	Schematic illustration and photograph of the computer-controlled clinical instrumentation developed for Roswell Park Cancer Institute .....	51
Figure 2.2	Photograph and illustration of the off-surface fiber optic probe ...	54
Figure 2.3	Custom 2x1 and 2x2 fiber optic switches.....	57
Figure 2.4	Switch driver circuitry .....	59
Figure 2.5	Treatment and measurement cycles during clinical PDT system operation.....	61
Figure 2.6	Reflectance monitored from a superficial sBCC lesion .....	64
Figure 2.7	Scaled Monte Carlo path length distributions .....	68
Figure 2.8	Flow diagram of the scaled-MC fitting routine .....	72
Figure 2.9	White-light reflectance spectrum $\pm$ SEM acquired from a sBCC lesion prior to therapy and the resulting nonlinear fit using the scaled MC algorithm.....	74

Figure 2.10	MC-modeled photon density as a function of tissue depth for recovered photons during reflectance spectroscopy .....	76
Figure 2.11	Normalized fluorescence emission curves for PpIX and photoproduct I .....	78
Figure 2.12	Fluorescence spectrum measured from a sBCC lesion.....	81
Figure 2.13	PpIX and photoproduct I fluorescence amplitudes detected in the lesion field throughout a single PDT treatment.....	83
Figure 2.14	MC-modeled detected fluorescence as a function of tissue depth for photons recovered during fluorescence spectroscopy .....	85
Figure 3.1	MC-modeled fluence distribution of PDT therapy.....	100
Figure 3.2	Representative sBCC lesions and treatment fields.....	104
Figure 3.3	Comparison of the averaged $\pm$ SEM, normalized PpIX contribution to the corrected fluorescence as a function of total fluence between lesion and margin fields .....	106
Figure 3.4	Averaged $\pm$ SEM PpIX initial bleaching rate during ALA-PDT of sBCC .....	108
Figure 3.5	Averaged $\pm$ SEM, normalized PpIX contribution to the corrected fluorescence as a function of delivered fluence from the (A) lesion and (B) margin fields during ALA-PDT .....	109
Figure 3.6	$D_{80} \pm$ SEM for irradiances of 10, 20, 40, 50, and 60 mW cm <sup>-2</sup> .....	111
Figure 3.7	VAS pain scores $\pm$ SEM experienced with ALA-PDT of sBCC.....	115
Figure 3.8	Representative reflectance spectra taken from an sBCC lesion and margin undergoing ALA-PDT .....	118
Figure 3.9	Blood oxygen saturation $\pm$ SEM during the course of ALA-PDT for each irradiance group .....	119

Figure 3.10	Treatment-induced change to PpIX fluorescence measured at 150 mW cm <sup>-2</sup> for the lesion and margin.....	121
Figure 4.1	Schematic of the darkfield spectrometer .....	141
Figure 4.2	Relative NAs of darkfield condenser, collection objective, and fiber collector.....	144
Figure 4.3	Darkfield spectra for NPe6-loaded and control cells .....	147
Figure 4.4	Scattering microscope in imaging and spectroscopy modes .....	150
Figure 4.5	Representative data from 4 μm diameter fluorescent polystyrene microspheres .....	159
Figure 4.6.	Fluorescence images of EMT6 cell monolayers .....	161
Figure 4.7	Ray intercept plots and spot diagrams of the optical response of the external optics in both the image and Fourier modes of the scattering microscope .....	163
Figure 4.8	Ray intercept plots and spot diagrams for the optics in image and Fourier modes, including Nikon side-port optics .....	165
Figure 4.9	Ray trace through scattering microscope upgrade in imaging mode .....	167
Figure 5.1	Experimental setup for focal laser photolysis and optical characterization.....	178
Figure 5.2	Modeled optical performance of the focal flash photolysis instrument.....	181
Figure 5.3	Experimental setup for focal laser photolysis PSF characterization.....	183
Figure 5.4	Photolysis of Ci-InsP3 in parotid acinar cells .....	187

# Chapter 1

## Introduction

This thesis is the result of three independent studies. Each investigation included the development of and experiments with a novel optical instrument. Each system explored a fundamentally different biological level. Clinical instrumentation was developed that delivered and monitored therapy using both reflectance and fluorescence spectroscopy in highly scattering tissues. A multifunctional microscope combined fluorescence, darkfield, brightfield and scattering imaging. This allowed advanced studies of cell populations, governed primarily by single scattering events. Finally, a focal photolysis instrument was built, which explored the fundamentals of calcium signaling in single cells.

The first system, presented in Chapter 2, was a multifunctional clinical instrument, which delivered aminolevulinic acid-photodynamic therapy (ALA-PDT) while performing non-invasive spectroscopic monitoring *in vivo*. The

system was built around fluorescence and reflectance measurements. Many of the design principles and much of the functionality on which this instrumentation was built had been developed in this laboratory over the past decade. This instrumentation was developed primarily to provide advanced treatment and PDT dose metric monitoring capabilities into a clinical instrument that was affordable, portable, and easy to use. The result was a push-button system, which could deliver the PDT treatment source and perform fluorescence and reflectance spectroscopies. Feedback from the spectroscopy was used to control treatment duration and the treatment irradiance without intervention. Much of Chapter 2 has been published in Cottrell *et al.* (2006), and co-authorship with Allan R. Oseroff and Thomas H. Foster is gratefully acknowledged.

Chapter 3 of this thesis subsequently describes the incorporation of this instrument into clinical trials at Roswell Park Cancer Institute in Buffalo, New York. This trial successfully established the irradiance-dependence of patient tolerability to ALA-PDT of superficial basal cell carcinoma (sBCC) and a pain-threshold irradiance, below which patients did not experience significant pain or require anesthetic. The irradiance-dependence of sensitizer photobleaching was also monitored and was used to determine a likely optimal irradiance that maximized treatment efficiency. Reflectance spectroscopy was collected in

order to correct the measurements for optical properties and also provided information on blood oxygen saturation, which is currently being used to inform future studies and delivery concepts as well as an anticipated clinical trial of low-irradiance PDT. Portions of the research presented in Chapter 3 have been published in Cottrell *et al.* (2008), and was co-authored by Anne D. Paquette, Kenneth R. Keymel, Thomas H. Foster, and Allan R. Oseroff. Additional material is being published in Wang *et al.* (2008), co-authored by Kenneth K.-H. Wang, Soumya Mitra, Allan R. Oseroff, and Thomas H. Foster.

We additionally report the design, construction, and characterization of two optical systems used for cellular scattering measurements in Chapter 4. The multifunctional scattering and fluorescence microscope described in this chapter employed co-registered brightfield, Fourier-filtered darkfield, and fluorescence imaging. Additionally, it provided imaging of the sample Fourier plane, which was used to extract angle-resolved scattering information. Finally, it allowed white-light spectroscopy of the region imaged in the other modalities. A system with enhanced performance was then modeled. The research in Chapter 4 can be found in Wilson *et al.* (2007) and Cottrell *et al.* (2007). Co-authorship with Thomas H. Foster and Jeremy D. Wilson is gratefully acknowledged for both of these papers.

Lastly, we report on the development of a microscope-based system used for focal laser photolysis. This system was used with cell-permeable caged messenger molecules and analyte specific fluorophores to provide local stimulation of intact cells and subsequent analyte monitoring. This provided a high-precision, non-invasive means for studying  $\text{Ca}^{2+}$  dynamics between cell types and between sub-cellular regions within a single cell type. The resulting studies compared the mechanisms underlying the  $\text{Ca}^{2+}$  signal globalization in these individual exocrine cell types and under regional messenger release. This work was originally presented in Hak Won *et al.* (2007), for which co-authorship with Jong Hak Won, Thomas H. Foster, and David I. Yule is gladly acknowledged.

## **1.1 Introduction to photodynamic therapy**

Photodynamic therapy (PDT) is a selective, three-part therapy using a combination of photosensitizer, light, and oxygen to generate singlet oxygen in tissues. Singlet oxygen reactions lead to cell death, vascular shutdown, and host inflammatory and immune responses (Dougherty *et al.*, 1998; Zeitouni *et al.*, 2003). Over the last several decades, PDT has become an established treatment modality for a variety of medical conditions including actinic keratosis, Barrett's esophagus, and most notably, several types of cancer (Moan and Peng, 2003;



Salva, 2002). During PDT, a photosensitizer is administered to either cancerous tissues or benign lesions in an activatable form or as a prodrug, a photosensitizer precursor metabolized by the body into a photosensitizer. Irradiation with visible or near-infrared light excites the photosensitizer, leading to a molecular energy transfer and creation of singlet oxygen, a short lived and highly reactive cytotoxic species (Reszka *et al.*, 1992).

Soon after its accidental discovery in the 19<sup>th</sup> century, where a combination of acridine orange dye and light was observed to kill paramecia, PDT was explored for medical applications, being used to treat skin cancer as early as 1904 (Ackroyd *et al.*, 2001). Studies carried out in the 1960s by Lipson showed that hematoporphyrin and hematoporphyrin derivative (HPD), a porphyrin mixture, could be useful in medical applications for selective fluorescence photodetection of neoplastic tissues (1967). PDT was revived as a cancer treatment in modern medicine primarily by Dougherty, who exploited HPD's innate selectivity with localized illumination to treat tumors (1978a; 1978b). Treatment modalities utilizing PDT have since emerged for numerous medical conditions and employing a variety of newly developed photosensitizers (Moan and Peng, 2003).

PDT has demonstrated significant benefits over radiotherapy and chemotherapy for many indications. The main advantage of this therapy in oncology is that it is comparatively selective for cancerous tissues. Preferential drug accumulation in neoplastic tissues has been observed for several sensitizers, attributed primarily to cancer histology (Lopez *et al.*, 2004), though most of the selectivity comes from the careful application of the treatment light and local drug application. Additionally, PDT benefits from minimal side effects, demonstrating extremely favorable cosmetic results, important to epithelial treatments. It also has no known cumulative or mutagenic effects, which allows nearly unlimited tumor re-treatment and salvage of tumors which have failed to respond to other primary therapies (Lou *et al.*, 2004; Yano *et al.*, 2005).

Nevertheless, despite these clear benefits there are limitations to PDT, which have slowed its general acceptance by the medical community as a standard of care. The long lasting skin photosensitivity and other shortcomings of the first-generation photosensitizers (Gomer, 1991) have been reduced using new photosensitizers, such as  $\delta$ -aminolevulinic acid (ALA)-induced protoporphyrin IX (Allison *et al.*, 2004; Moan and Peng, 2003). Chapters 2 and 3 of this thesis address two of the other limitations to PDT: complex dosimetry and treatment-induced pain. As with any medical treatment, high efficacy relies on the delivery of the appropriate dose to the treatment area. Therefore, making

accurate and real-time determinations of therapeutic dose delivered by PDT an area of active research with clinical importance. PDT dose has historically been determined using the concentration of the photosensitizing agent in the target tissue, the fluence of treatment light, and the time between when the sensitizer is delivered and when it is irradiated. This time is referred to as the drug-light interval and accounts for the sensitizer pharmacokinetics. The complicated interaction among light, drug, and tissue environment in PDT makes dosimetry a dynamic problem. A mounting understanding of fundamental PDT mechanisms and the advancement of tissue optics, however, promises *in vivo* optical monitoring capable of performing real-time dosimetry in the clinical setting.

In Chapter 2, we present instrumentation that translates dosimetry research from this and other laboratories from bench top to bedside, incorporating treatment with fluorescence and reflectance spectroscopies. Although spectroscopy has been used in clinical settings during PDT (Johansson *et al.*, 2006; Thompson *et al.*, 2005), we are aware of no devices that combine these spectroscopies with the delivery of the PDT treatment laser in a single, compact system. The instrumentation and related analyses allow real-time photosensitizer photobleaching measurements and characterization of blood oxygen during PDT of cutaneous disease. The functionality of this instrumentation is presented in Chapter 3, in which we describe a clinical trial employing this instrumentation

during ALA-PDT of superficial basal cell carcinoma (sBCC). This clinical trial established the irradiance-dependence of patient tolerability to ALA-PDT of sBCC and a pain-threshold irradiance, below which patients did not experience significant pain or require anesthetic. The irradiance-dependence of PpIX fluorescence photobleaching may be used in a future clinical trial to establish an optimal irradiance for efficient pain-free therapy.

### **1.1.2 Photophysical and photochemical kinetics**

The fundamental photophysics of PDT can be understood by examining the interaction between the photosensitizer and light to produce singlet oxygen, denoted  $^1\text{O}_2$ , which is universal among second-generation photosensitizers such as ALA-induced protoporphyrin IX (PpIX). In this interaction the combination of light, photosensitizer, and ground-state oxygen,  $^3\text{O}_2$ , within a cellular environment, produces  $^1\text{O}_2$ .  $^1\text{O}_2$  is the lowest-lying electronic excited-state of  $^3\text{O}_2$  and is believed to be the species responsible for necrosis and apoptosis generated with PDT (Reszka *et al.*, 1992). The energy required for the transition from  $^3\text{O}_2$  to  $^1\text{O}_2$  corresponds to a 1270 nm photon. The spectroscopic transition between these states, however, is forbidden by quantum selection rules (Adamson, 1979). Direct optical pumping of  $^3\text{O}_2$  for treatment is therefore prohibited, necessitating the intermediary photosensitizer. The photochemical kinetics of PDT can be understood by considering the photochemistry by which

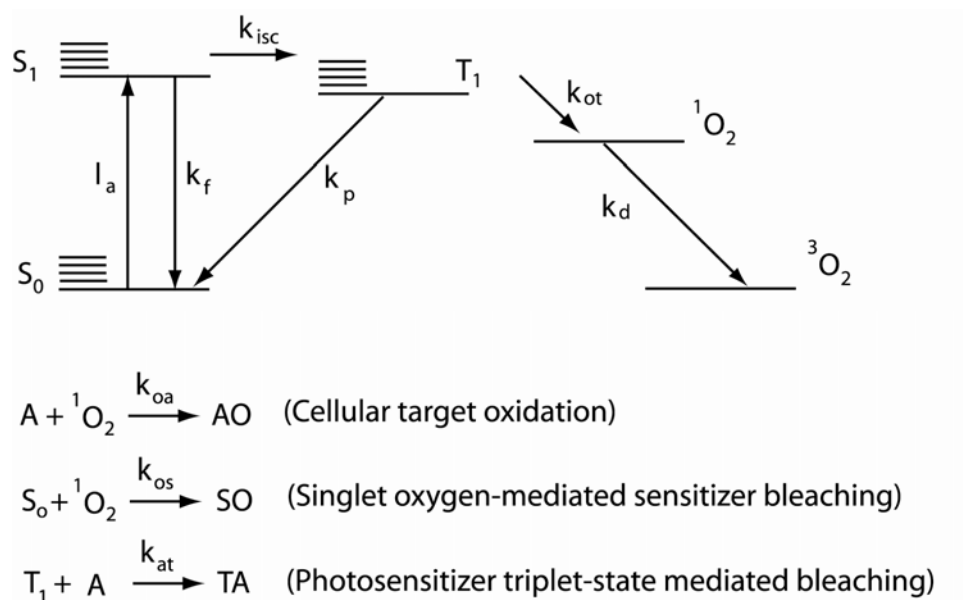


Figure 1.1: Jablonski diagram of photodynamic therapy photochemistry. The photosensitizer excited singlet-state  $S_1$  is populated at a rate  $I_a$  by photon absorption of the ground state photosensitizer,  $S_0$ , which spontaneously decays back into the ground state at the rate  $k_f$ . The excited photosensitizer can alternatively undergo intersystem crossing to produce the triplet photosensitizer state  $T_1$  at the rate  $k_{\text{isc}}$ . The triplet state is either quenched by ground-state oxygen at a rate  $k_{\text{ot}}$ , producing  ${}^1\text{O}_2$ , or returns to its ground state at a rate  $k_p$ . Similarly,  ${}^1\text{O}_2$  either transfers back to its ground state at  $k_d$ , oxidizes an endogenous molecule,  $A$ , or bleaches the photosensitizer itself at a rate of  $k_{\text{os}}$ . Photosensitizer triplet-state-mediated bleaching occurs at a rate  $k_{\text{at}}$ .

an incident photon interacts with a photosensitizer to produce  $^1\text{O}_2$ , as illustrated by way of a Jablonski energy diagram as shown in Figure 1.1. The photosensitizer excited singlet-state  $S_1$  is populated at a rate  $I_a$  by photon absorption of the ground state photosensitizer,  $S_0$ , which spontaneously decays back into the ground state at the rate  $k_f$ . The excited photosensitizer can alternatively undergo intersystem crossing to produce the triplet photosensitizer state  $T_1$  at the rate  $k_{isc}$ . The triplet state is either quenched by ground-state oxygen at a rate  $k_{ot}$ , producing  $^1\text{O}_2$ , or returns to its ground state at a rate  $k_p$ . Similarly,  $^1\text{O}_2$  either transfers back to its ground state at  $k_d$ , oxidizes an endogenous molecule, A, or bleaches the photosensitizer itself at a rate of  $k_{os}$ . Photosensitizer triplet-state-mediated bleaching occurs at a rate  $k_{at}$ . Bleaching appears to be dominated by a  $^1\text{O}_2$  mechanism under most relevant conditions for several photosensitizers (Georgakoudi and Foster, 1998).

### 1.1.3 Implicit PDT dosimetry

Several researchers have used fluorescence photobleaching for ‘implicit’ PDT dosimetry. In implicit dosimetry a surrogate dose metric, which is accessible and quantifiable, is measured and indirectly reports on a dose metric which is not directly observable (Wilson *et al.*, 1997a). Photobleaching is an attractive surrogate dose metric, as it is mediated by mechanisms similar to oxidation of cellular targets and is accessible through non-invasive fluorescence spectroscopy

(Georgakoudi *et al.*, 1997). Photobleaching therefore indirectly reports on unobservable  $^1\text{O}_2$  reactions. *In vivo* photobleaching has been explored by a number of investigators who have demonstrated that the photosensitizer bleaching rate is related to oxygen availability, is predictive of therapeutic outcome (Boere *et al.*, 2002; Robinson *et al.*, 1998; Robinson *et al.*, 1999), and has an irradiance dependence, showing more efficient bleaching at lower irradiances (Finlay *et al.*, 2001; Langmack *et al.*, 2001).

Chapters 2 and 3 of this thesis present results of *in vivo* photobleaching measurements during ALA-PDT of human basal cell carcinomas. In this study we found an irradiance-dependent photobleaching that was consistent with  $^1\text{O}_2$ -mediated bleaching. Though the high baseline efficacy of this therapy may obviate correlation of photobleaching rates to efficacy, photobleaching may be employed as feedback in future PDT regimens designed to deliver the therapy quickly and painlessly. This idea is explored further in Chapter 3.

#### **1.1.4 ALA-PDT**

Though first-generation photosensitizers have been successfully used in a wide variety of applications, second-generation photosensitizers have been developed which limit a patient's photosensitivity. The expanding variety of photosensitizers available for cutaneous PDT ranges from systemically-injected

vascular targeting to topically administered agents (Allison *et al.*, 2006). For the majority of sensitizers, the activatable sensitizer is delivered and redistributes in the tissue between delivery and treatment (drug-light interval). Treatment with ALA, however, represents a different approach in which a photosensitizer precursor naturally occurring in the heme biosynthesis pathway is administered, and the photosensitizer PpIX is subsequently synthesized by the tumor cells. Though ALA is an endogenous compound which has been studied for decades, the introduction of ALA-PDT is credited to Malik and Lugaci, who used ALA-PDT *in vitro* (1987). This modality was expanded to PDT using topical drug administration by Kennedy and Pottier (1992).

The excitation and fluorescence spectra of PpIX are shown in Figure 1.2. The excitation spectrum is dominated by strong Soret absorption at 403 nm and several smaller peaks in the visible wavelengths between 514 and 632.8 nm. The bluer absorption bands are often exploited for very thin lesions, such as actinic keratosis, whereas thicker tumors are treated using the 632.8 nm band, allowing deeper light penetration. The fluorescence spectrum is similarly dominated by a primary peak at 635 nm and a secondary, smaller peak at 705 nm.



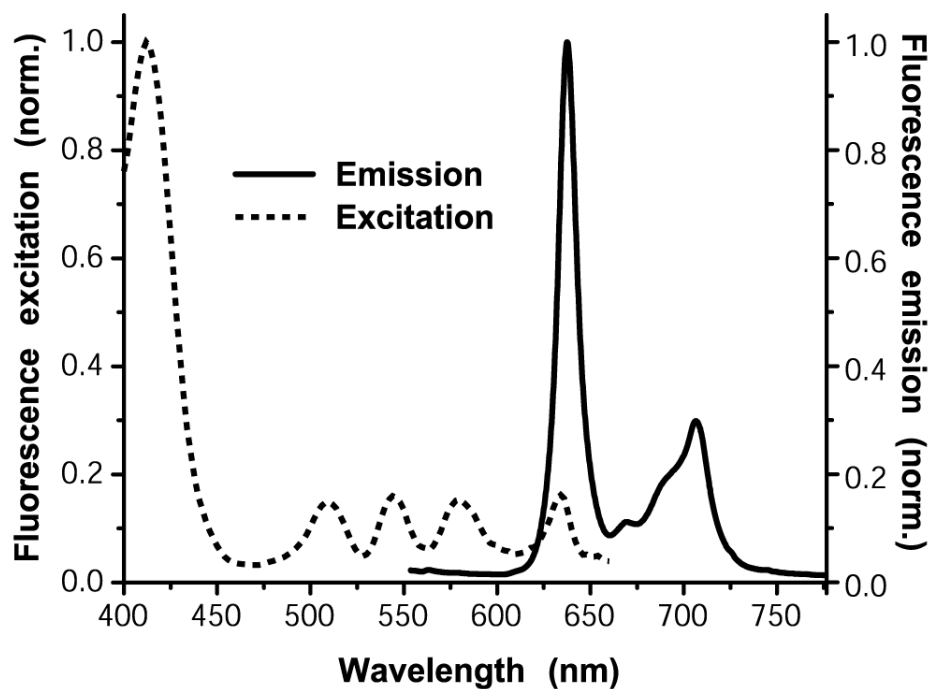


Figure 1.2: Excitation and emission spectra of PpIX in EMT6 cells. The excitation spectrum is dominated by strong Soret absorption at 403 nm and several smaller peaks in the visible wavelengths between 514 and 632.8 nm. The fluorescence spectrum is dominated by a primary peak at 635 nm and a secondary, smaller peak at 705 nm.

The conversion of ALA to PpIX within the cell takes place using the heme cycle within the cell cytosol and mitochondria, as illustrated in Figure 1.3. ALA in the cell cytosol undergoes a cascade of reactions which includes the production of uroporphyrinogen III and coproporphyrinogen III. The latter re-enters the mitochondria where it is converted to PpIX before the enzyme ferrochelatase adds iron, producing heme. Heme consequently inhibits the transcription of ALA-synthase and the action of the existing ALA-synthase, acting as a negative feedback control on ALA production. The addition of exogenous ALA bypasses this feedback control, and the process becomes rate-limited by ferrochelatase, resulting in accumulation of PpIX and other downstream metabolites.

Sensitizer localization both in specific tissues and in subcellular components determines to a large degree the efficacy of treatment and the mechanisms of cellular death. ALA-induced PpIX localizes primarily near mitochondria where it is produced (Wilson *et al.*, 1997b). The spectroscopic signatures of uroporphyrin and coproporphyrin have been identified in normal rat skin after treatment with ALA-PDT (Finlay *et al.*, 2001), and water-soluble porphyrins have formed during tumor PDT treatment (Dietel *et al.*, 1997). The buildup of these chemicals suggests a possible disruption of the heme synthesis pathway, indicating primary damage to mitochondria and also suggests that secondary porphyrins may be useful as reporters of cellular damage (Finlay *et al.*, 2001).

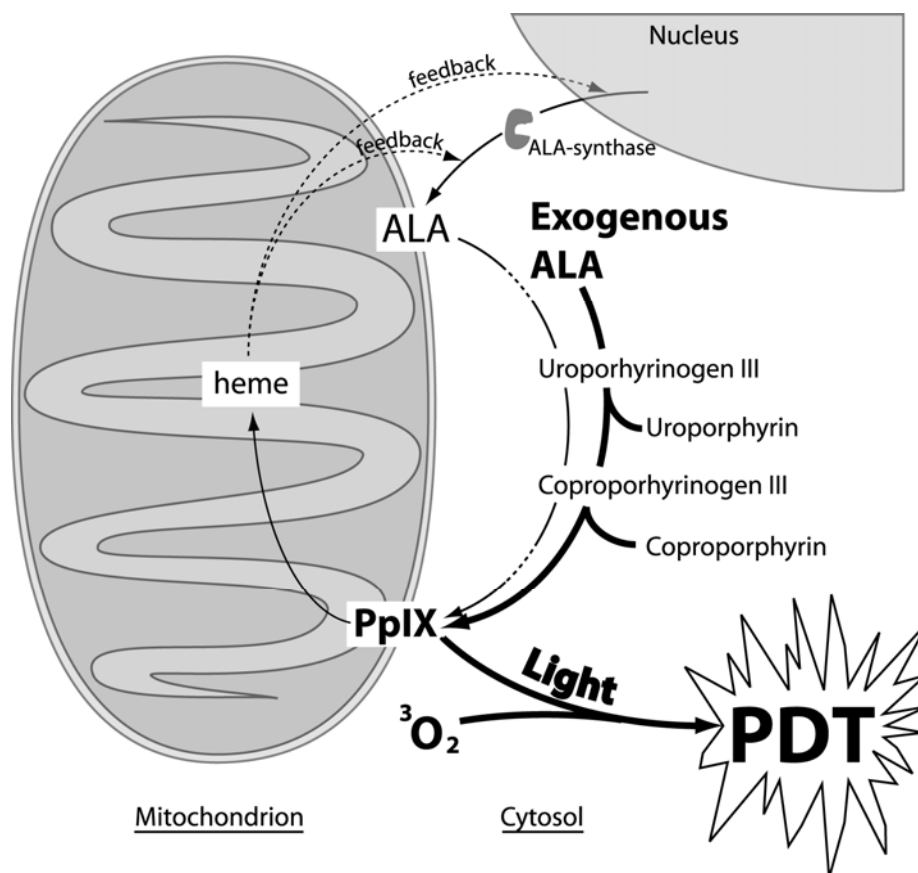


Figure 1.3: Biosynthetic pathway for the production of PpIX from ALA. The enzymes and metabolites in this reaction are located in mitochondrion and the cytosol. Heme negatively regulates ALA-synthase at two points, in its transcription and its production of ALA. Exogenous ALA induces excess formation of heme precursors, including the photosensitizer PpIX.

The observed preferential accumulation of ALA in neoplastic tissues is suspected to be caused primarily by physiological differences between cancerous and normal tissues. This accumulation has been linked to enzyme profiles, leaky vasculature, newly formed collagen, a lower extracellular pH, and abnormal stroma with large interstitial space (Freitas, 1990; Moan and Peng, 2003; Musser *et al.*, 1980). The interstitial distribution of sensitizer is also largely dependent on the drug-light interval used. Prodrug sensitizers such as ALA must have sufficient time to metabolize into PpIX but be irradiated before completely metabolized into heme, which is not photoactive (Stefanidou *et al.*, 2000). Methods of increasing the limited drug penetration depth of ALA, which has restricted the use of this drug beyond cutaneous applications, are also being investigated. These methods include variations to the drug formulation, compound alteration, and physical manipulation (Lopez *et al.*, 2004).

### **1.1.5 Optical properties of tissue**

The work in Chapters 2 and 3 of this thesis involves spectroscopic measurements in tissue, where the effects of the optical properties on the measured spectra must be taken into account. Two effects govern the propagation of light in tissue: absorption and scattering. There are several biological sources of absorption which include water, melanin, oxy- and deoxyhemoglobin, and a host of other molecules. Similarly, cellular scattering

is dominated by mitochondria, lysosomes, nuclei, and membranes. Though there have been a variety of investigations in this laboratory and others which have explicitly investigated light scattering from individual organelles and cells modeled with Mie theory and other tools (Drezek *et al.*, 1999; Wilson and Foster, 2005), the problem of determining exact solutions becomes intractable when considering tissue and other ensembles of heterogeneous scatterers. Alternatively, the medium is treated as a homogenous material characterized by bulk absorption and scattering coefficients. The absorption coefficient,  $\mu_a$ , has units of inverse length and describes a medium containing many absorbers at a fixed concentration. For a photon traveling in this medium a distance  $l_a$ , the chance that it is unabsorbed and transmitted,  $t_a$ , is

$$t_a = \exp(-\mu_a l_a). \quad [1.1]$$

Similarly, the scattering coefficient  $\mu_s$  describes the scattering effects of a medium with many scatterers. Like absorption, the probability  $t_s$  of a photon traveling a distance  $l_s$  without being deflected from its initial trajectory by scattering is

$$t_s = \exp(-\mu_s l_s). \quad [1.2]$$

Scattering is further described by the scattering phase function  $p(\hat{s}, \hat{s}')$ , which defines the probability that a photon incident from direction  $\hat{s}'$  will be scattered

into direction  $\hat{s}$ . Typically, phase functions are approximated by simple analytical forms in terms of the anisotropy,  $g$ , the average cosine of the scattering angle,

$$g = \int_{4\pi} p(\hat{s}, \hat{s}') (\hat{s} \cdot \hat{s}') d\Omega. \quad [1.3]$$

If  $g = 0$  the scattering is isotropic, whereas  $g = 1$  describes complete forward scattering. Though there are several phase functions which have been used to approximate scattering in tissue and other turbid media, the Henyey-Greenstein function,

$$p_{\text{HG}}(\hat{s} \cdot \hat{s}') = \frac{1 - g^2}{4\pi[1 + g^2 - 2g(\hat{s} \cdot \hat{s}')]^{\frac{3}{2}}}, \quad [1.4]$$

(Henyey and Greenstein, 1941) is important to note since it is a simple analytical function which dominates in the literature and is used in the simulations described in this thesis. In skin, light scattering dominates the effect of absorption and can dramatically affect light propagation. The transport mean free path  $\frac{1}{\mu'_s}$ , where  $\mu'_s = \mu_s(1 - g)$ , describes the distance a photon travels in the medium before its direction has been randomized. The degree to which scattering dominates absorption in tissue is characterized by the albedo,

$$a = \frac{\mu_s}{\mu_s + \mu_a}. \quad [1.5]$$

For a wide variety of tissues, the wavelength-dependent reduced scattering spectrum,  $\mu'_s(\lambda)$ , can be approximated with the simple form

$$\mu'_s(\lambda) = A \left( \frac{\lambda}{\lambda_0} \right)^{-b}, \quad [1.6]$$

where A is the value of  $\mu'_s$  at  $\lambda_0$  and b is typically between 1.5 and 2 (Finlay and Foster, 2004b; Mourant *et al.*, 1998). Figure 1.4 shows a typical scattering spectrum of this form, which is representative of tissue scattering spectra measured in this laboratory.

Tissue absorption between 450 nm and 900 nm is dominated by chromophores oxy- (HbO) and deoxyhemoglobin (Hb), water (H<sub>2</sub>O), and melanin (Mel), the extinction coefficients of which are shown in Figure 1.5. This allows the absorption in tissue as a function of wavelength to be approximated as

$$\mu_a(\lambda) = [\text{HbO}] \varepsilon_{\text{HbO}} + [\text{Hb}] \varepsilon_{\text{Hb}} + [\text{H}_2\text{O}] \varepsilon_{\text{H}_2\text{O}} + [\text{Mel}] \varepsilon_{\text{Mel}}, \quad [1.7]$$

where  $\varepsilon_{\text{HbO}}$ ,  $\varepsilon_{\text{Hb}}$ ,  $\varepsilon_{\text{H}_2\text{O}}$ , and  $\varepsilon_{\text{Mel}}$  are the wavelength-dependent molar extinction coefficients of HbO, Hb, water, and melanin, and [HbO], [Hb], [H<sub>2</sub>O], and [Mel] represent their respective concentrations. Hemoglobin oxygen saturation,  $\text{SO}_2$ , is consequently found using

$$\text{SO}_2 = \frac{[\text{HbO}]}{[\text{HbO}] + [\text{Hb}]}. \quad [1.8]$$

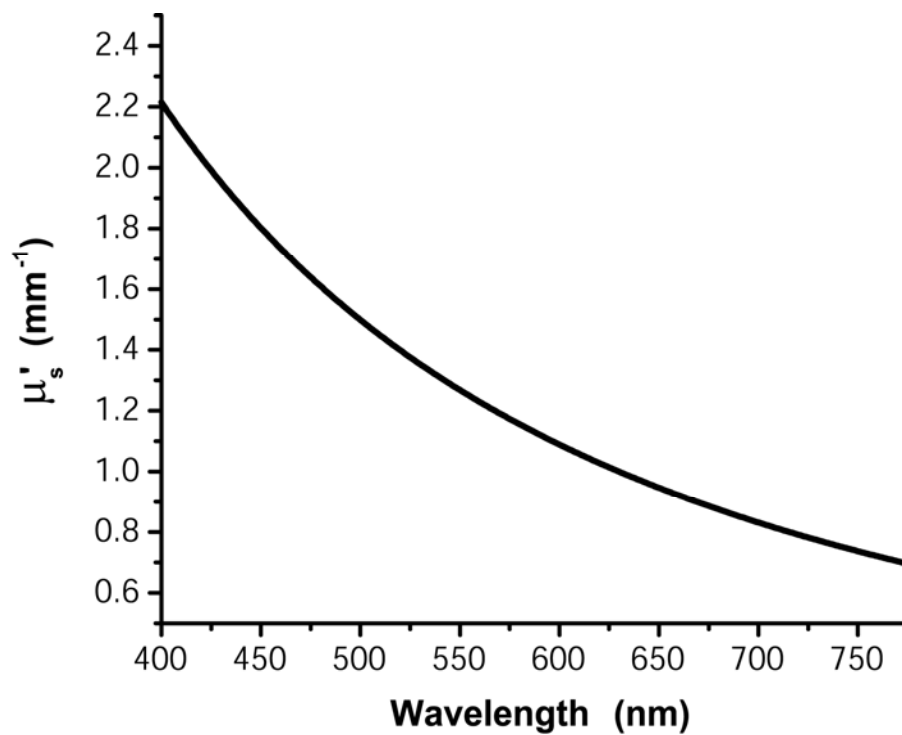


Figure 1.4: Reduced scattering spectrum in tissue. Typical reduced scattering spectrum found with Equation 1.6 using the physiologically realistic constants of  $A = 1 \text{ mm}^{-1}$  and  $b = 1.75$  and  $\lambda_0 = 632.8 \text{ nm}$ .



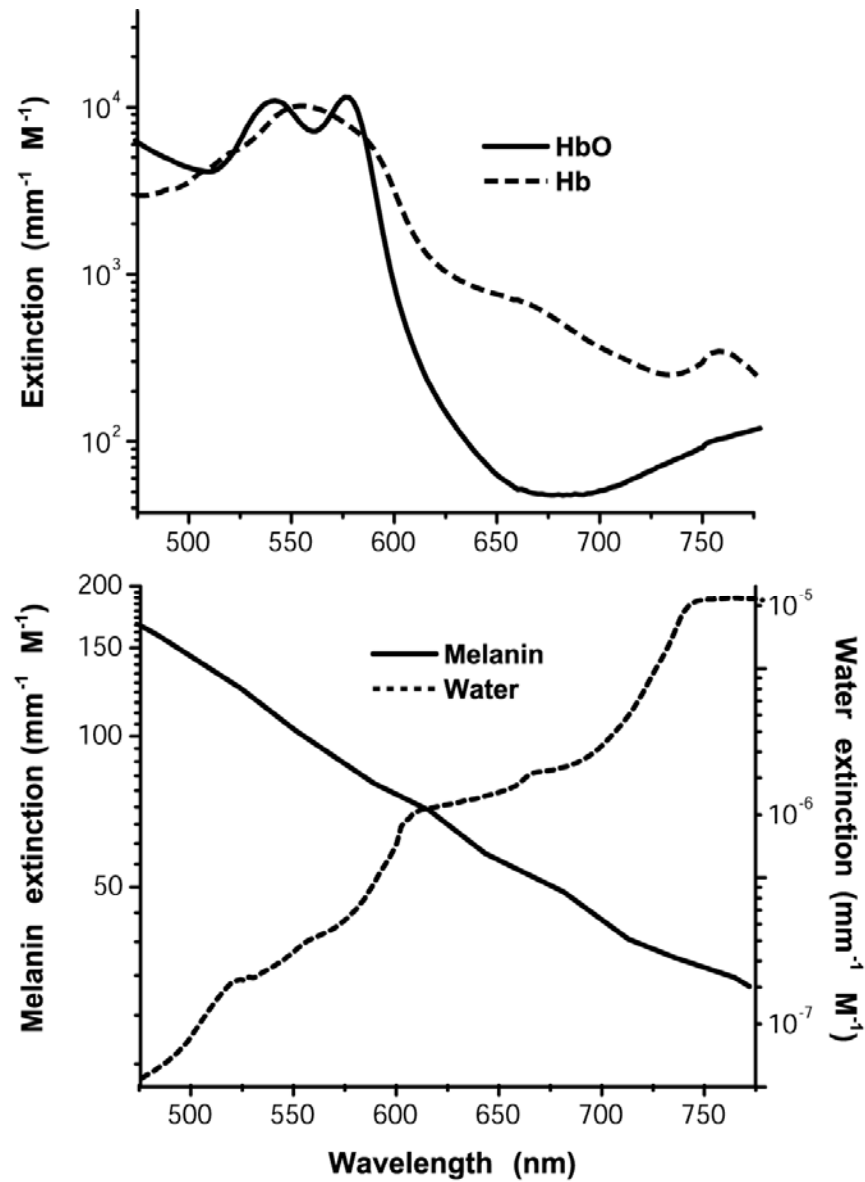


Figure 1.5: Absorption spectra for (top) oxyhemoglobin, deoxyhemoglobin, (bottom) water (Donze *et al.*, 1994), and melanin (Jacques and Mcauliffe, 1991). The oxy- and deoxyhemoglobin spectra shown were taken from a variety of sources and include the effects of pigment packaging in red blood cells (Finlay and Foster, 2004a).

In addition to affecting the measurement of absorbers in tissue, as described above, tissue optical properties distort measured fluorescence spectra. Therefore, quantitative or comparative fluorescence measurements must take into account the background of tissue optical properties and any changes thereto between measurements in order to account for the absorption and scattering effects of the measurement volume. Several researchers have developed solutions to the problem of extracting intrinsic fluorescence measurements from turbid media (Finlay and Foster, 2005; Gardner *et al.*, 1996; Muller *et al.*, 2001). In the tissue fluorescence results presented in Chapter 3, we do not quantify fluorophore concentrations directly, but instead rely on quantitative comparisons of fluorescence spectra intensity during the course of ALA-PDT. We therefore employ an empirical correction to *in vivo* fluorescence spectra, in which the influence of optical properties on fluorescence is informed by reflectance spectroscopy of the same tissue (Wu *et al.*, 1993). This correction is implemented by dividing the measured fluorescence spectrum by the white-light reflectance spectrum measured in the same test geometry and in the same spectral window.

## **1.2 Introduction to cellular scattering**

In Chapter 4 of this thesis we explore biological scattering dominated by single scattering events. In biology and medicine, these single-scatterer measurements

have enabled the measurement of intracellular organelle size distributions in intact cells (Mourant *et al.*, 2002; Yu *et al.*, 2006) as they are sensitive to particle sizes and relative changes in particle sizes that are smaller than the diffraction limit of an optical microscope. There is an increasing body of work in the literature on scattering from intact cultured cells and in tissue to quantify sub-cellular morphology. These reports initially focused on wavelength-resolved and angularly-resolved backscattering measurements from tissues, where nuclear sizes could be extracted for use in histology and identification of neoplastic tissues (Backman *et al.*, 1999; Perelman *et al.*, 1998; Wax *et al.*, 2002). When using cultured cells, however, scattering measurements are free from complications involving the diffusive background present in tissues. This has enabled a variety of reports demonstrating light scattering sensitivity to smaller organelles, particularly demonstrating mitochondrial morphology changes induced by a variety of stresses (Boustany *et al.*, 2004; Schuele *et al.*, 2005; Wilson *et al.*, 2005). Boustany used an optical scatter imaging microscope to observe mitochondrial swelling from intact cells in response to calcium insult (2002) as well as from cells undergoing apoptosis by staurosporine exposure (2004). Schuele was able to observe heat-induced mitochondrial morphology changes using wavelength-resolved backscattering measurements in cultured cells (2005). Studies in this lab have demonstrated

that angularly-resolved light scattering could monitor oxidative-stress-induced changes in mitochondrial morphology (Wilson *et al.*, 2005).

In principle, light scattering also has the ability to report both organelle sizes and relative changes to organelle size below the diffraction limit of an optical microscope in addition to organelle refractive index. While light scattering from cells has been modeled using a variety of methods (Boustany *et al.*, 2002; Drezek *et al.*, 1999), the majority of organelles of interest have dimensions between 0.1 and 10 times the wavelength of visible light. This has resulted in a number of researchers using Mie theory-based models to extract morphological information from scattering measurements. This theory provides exact solutions to the scattering of an infinite plane wave by a homogeneous sphere. Small-particle sizing was demonstrated by Fang, who used wavelength-resolved backscattering measurements with 450-750 nm light to size polystyrene microspheres as small as 175 nm with 20-nm accuracy (2003). They were able to size zymogen granules, extracted from cells, with length scales as small as 150 nm. These results were confirmed using electron microscopy.

Mie theory incorporates the parameters of particle size, particle refractive index, wavelength of light, and the refractive index of the surrounding medium, and it is able to capture the complex resonance behavior seen in light scattering. It has

been shown that for organelle sizes smaller than nuclei and for refractive indices of organelles in cytoplasm reported in the literature (Beuthan *et al.*, 1996; Liu *et al.*, 1996), the shape of both angularly-resolved (Mourant *et al.*, 2002) and wavelength-resolved (Fang *et al.*, 2003) light scattering distributions from a single particle depend strongly on particle size and weakly on the refractive index. The relative refractive index of the particle primarily affects the total scattering cross section. Because of this, many studies assumed that all organelles have identical refractive indices in their respective inversion algorithms.

For measurements using an ensemble of particles, such as the organelle populations within whole cells, it has also been shown that the observable signal is governed by the product of the number density of particles of a particular size and their scattering cross sections (Wilson and Foster, 2005). In an angularly resolved measurement, our laboratory showed that we were sampling a phase function,  $P(\theta)$ , which when measured from a collection of particles obeying a size distribution  $\rho(r)$ , was written

$$P_{\text{total}}(\theta) = \frac{\int \sigma(r) \rho(r) P(r, \theta) dr}{\int \sigma(r) \rho(r) dr}, \quad [1.9]$$

where  $\sigma(r)$  is the scattering cross section. There is an analogous expression for a wavelength-resolved measurement. Because each particle's scattering cross

section is dependent on its index of refraction, it is clear from Equation 1.9 that a rigorous model of light scattering from cells needs to have *a priori* knowledge of the indices of refraction for different organelle populations that may blend together in size.

Though a number of sizing experiments have been carried out using cellular suspensions and whole tissues have demonstrated impressive results, the majority of cancers form in epithelial cells, which are cultured in the laboratory as adherent monolayers. It is therefore important to adapt scattering measurements to this geometry, which is well-suited to the development of scattering microscopes. Microscope platforms also support multiplexed functionality and benefit from a well-characterized optical system. Several designs have been published recently, many of which are based on measurements of backscattered light (Fang *et al.*, 2007; Liu *et al.*, 2005). Rigorous particle sizing of non-spherical scatterers within a Mie theory model is extremely well-suited to measurements of light scattered into forward angles, where the sensitivity to particle shape is minimal (Mishchenko *et al.*, 2002). In Chapter 4, we report the design, construction, and initial characterization of two optical systems used for cellular scattering measurements: a forward scattered white-light spectroscopy system used to characterize lysosomal refractive index and a multifunctional scattering and fluorescence microscope that exploits an

angle-resolved forward-scattering geometry. The multifunctional scattering and fluorescence microscope likewise employs brightfield, Fourier-filtered darkfield, direct imaging of the Fourier plane, angle-resolved scattering, and white-light scattering spectroscopy while preserving a fluorescence imaging channel.

### **1.3 Introduction to fluorescence calcium monitoring**

In Chapter 5 of this thesis we report on the construction and characterization of optical instrumentation designed to explore calcium ion,  $\text{Ca}^{2+}$ , dynamics *in vitro*. A microscope-based system was developed, which provided focal photolysis of chemically-caged messenger molecules in pancreatic and parotid acinar cells. These polarized cells exhibit large variations between their basal (attached region) and apical (distal) ends. In the resulting studies, local photolysis and release of the messenger molecules, within specific regions of the cells, was used to investigate the cell-specific mechanisms underlying the generation of  $\text{Ca}^{2+}$  signals and their resulting propagation. This allowed the exploration of the specialization of these properties between these cell types and within specific regions of a single cell.

The cation  $\text{Ca}^{2+}$  is a cellular messenger which controls a variety of cellular processes such as muscle contraction, cell death or proliferations, and secretion (Straub *et al.*, 2000), the latter being a primary function of the acinar cells

explored in our studies. Messaging *via* changes to cytosolic free calcium concentrations ( $[Ca^{2+}]_i$ ) are controlled both by allowing the ion to enter from outside the cell and by releasing it from intracellular stores. Primary intracellular stores are the endoplasmic reticulum (ER), sarcoplasmic reticulum (SR), and mitochondria. Similarly,  $[Ca^{2+}]_i$  can be decreased by ATPase pumps, which pump the cation against a gradient outside the cell or into stores (Berridge *et al.*, 1990).

During normal cell function, the binding of an agonist such as a hormone to the cell surface may result in the downstream production of second messenger inositol trisphosphate ( $InsP_3$ ). This messenger can then diffuse to the membrane of the ER and bind to  $InsP_3$  receptors (IPR), opening a  $Ca^{2+}$  channel and initiating  $Ca^{2+}$  release from the ER. Receptors are also sensitive to  $[Ca^{2+}]_i$  and can serve as both positive and negative feedback mechanisms at low and high  $[Ca^{2+}]_i$ , respectively. These mechanisms allow  $Ca^{2+}$  oscillations, which are pivotal in inter- and intracellular signaling. A simple model has been presented in Figure 1.6, which incorporates the messengers and signals stimulated in these studies. Monitoring the dynamics of  $Ca^{2+}$  *in vitro* has been made common only relatively recently with advances in fluorescence sensing (Lakowicz, 1983; Tsien, 1989).



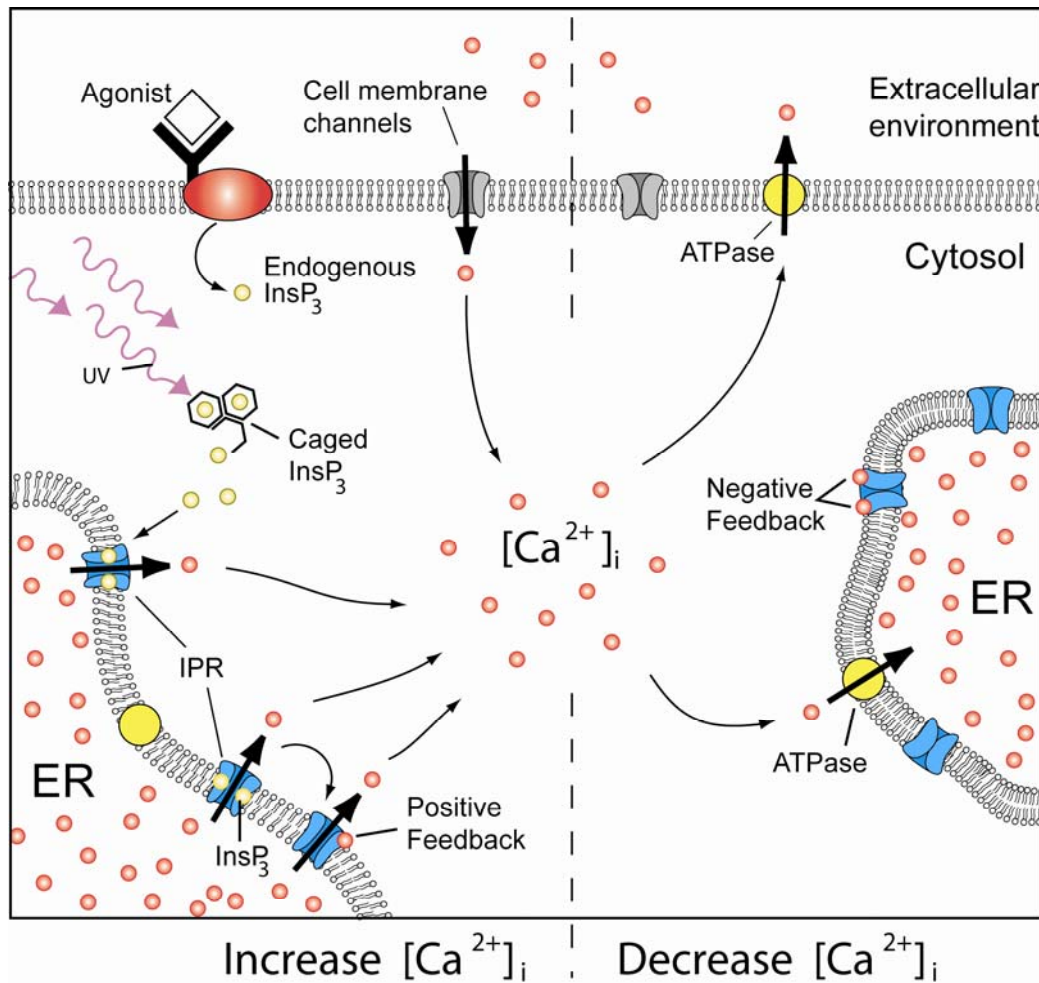


Figure 1.6: Cellular processes that regulate the increase and decrease of  $[Ca^{2+}]_i$ .  $Ca^{2+}$  is supplied to the cytosol from stores located in the endoplasmic reticulum (ER) and extracellular environment and accessed through membrane channels such as inositol trisphosphate receptors (IPR) under stimulation by inositol trisphosphate ( $InsP_3$ ) or  $Ca^{2+}$ . Similarly,  $Ca^{2+}$  is removed from the cytosol via active pumping by ATPase.

Fluorescence sensing for biological applications is an area of continuing research. There are a number of factors driving its use, which include benefits in cost, sensitivity, ease of disposal as compared to radioactive tracers, and the wide variety of potential sensing applications through fluorophore functionalization. For example, fluorescence probes have been designed to measure viscosity, pH, and intermolecular distances. One of the most important functions of fluorescence in biology – the application we explore in Chapter 5 of this thesis – is the detection of biological analytes *in vitro* (Tsien, 1989).

Fluorescence probes can be tailored to vary their fluorescence properties in response to an analyte. Variations can occur in intensity, excitation spectra, emission spectra, anisotropy, and fluorescence lifetime. The most direct sensing method is a change to the fluorescence intensity, which is used in these experiments. Initially developed by Tsien nearly thirty years ago, fluorescent calcium probes allow for optical detection and quantification both inside living cells and in extracellular environments (Tsien, 1989). The fluo-4 probe used in these studies has gained widespread use because of its >100 fold increase in fluorescence upon binding to  $\text{Ca}^{2+}$ , absorption spectrum overlap with common  $\text{Ar}^+$  laser lines, and excellent cell loading properties (Gee *et al.*, 2000).

These investigations also make use of photolabile (caged) compounds. Caged biological compounds have been rendered chemically inert. Irradiating these compounds with light, typically in the ultraviolet (UV) range, can result in a photochemical reaction that releases (uncages) the active form of the molecule. These molecules can therefore be loaded into cells in an inert form and then activated *in situ* to rapidly vary intracellular  $\text{Ca}^{2+}$  concentration as an alternative to monitoring changes using fluorescent indicators alone (McCray and Trentham, 1989).

A wide variety of instrumentation has been used to monitor fluorescence probes. Irradiance-based probes have been used extensively in high-throughput pharmacological screening instruments and plate readers. Increasingly, they have been used in microscope setups ranging from traditional microscopes to confocal and multiphoton systems. These systems allow high-quality imaging that explores heterogeneities in cells and among cell populations. Typically, these instruments employ UV uncaging of the entire sample plane, *via* the illumination port of the microscope. One exception has been the development of regional uncaging, enabled by multimode-fiber-based illumination. This system enabled messenger uncaging in sample regions as small as 100 microns in diameter (Wang and Augustine, 1995). A second design form has also been developed which makes use of the inherent point-illumination platform of a two-

photon confocal microscope. In this embodiment, uncaging is possible in femtoliter volumes *in vitro* (Brown *et al.*, 1999). The system presented in Chapter 5 provides a low-cost system in which UV can either be used to uncage the entire sample plane or in the subcellular focal volume of the imaging objective in a standard inverted microscope. This provides UV uncaging within micron-sized regions of cells and enables advanced exploration of  $\text{Ca}^{2+}$  dynamics.

### 1.3 References

- Ackroyd R., Kelty C., Brown N., and Reed M. (2001). The history of photodetection and photodynamic therapy. *Photochem. Photobiol.* **74**: 656-669.
- Adamson A.W. (1979). Molecular Spectroscopy and Photochemistry, A Textbook of Physical Chemistry, pages 789-848. Academic Press, Inc., New York.
- Allison R.R., Downie G.H., Cuenca R.E., Hu X.H., Childs C.J., and Sibata C.H. (2004). Photosensitizers in clinical PDT. *Photodiag. Photodyn. Ther.* **1**: 27-42.
- Allison R.R., Sibata C.H., Downie G.H., and Cuenca R.E. (2006). A clinical review of PDT for cutaneous malignancies. *Photodiag. Photodyn. Ther.* **3**: 214-226.
- Backman V., Gurjar R., Badizadegan K., Itzkan L., Dasari R.R., Perelman L.T., and Feld, M.S. (1999). Polarized light scattering spectroscopy for quantitative measurement of epithelial cellular structures *in situ*. *IEEE J. Quantum Electron.* **5**: 1019-1026.
- Berridge M.J. (1990). Calcium Oscillations. *J. Biol. Chem.* **265**:9583-9586.
- Beuthan J., Minet O., Helfmann J., Herrig M., and Muller G. (1996). The spatial variation of the refractive index in biological cells. *Phys. Med. Biol.* **41**: 369-382.

- Boere I., de Bruijn R., Robinson D., van den Boogert J., Sterenborg H., de Bruin R., and Tilanus H.W. (2002). Photodynamic therapy of the rat esophagus: Correlation between photobleaching and epithelial ablation. *Cancer Epidemiol. Biomarkers Prev.* **11**: 1184S.
- Boustany N.N., Drezek R., and Thakor N.V. (2002). Calcium-induced alterations in mitochondrial morphology quantified *in situ* with optical scatter imaging. *Biophys J.* **83**:1691-1700.
- Boustany N.N., Tsai Y.C., Pfister B., Joiner W.M., Oyler G.A., and Thakor N.V. (2004). BCL-x(L)-dependent light scattering by apoptotic cells. *Biophys. J.* **87**: 4163-4171.
- Brown E.B., Shear J.B., Adams S.R., Tsien R.Y., and Webb W.W. (1999). Photolysis of caged calcium in femtoliter volumes using two-photon excitation. *Biophys. J.* **76**: 489-499.
- Cottrell W.J., Oseroff A.R., and Foster T.H. (2006). Portable Instrument that integrates irradiation with fluorescence and reflectance spectroscopies during clinical photodynamic therapy of cutaneous disease. *Rev. Sci. Instrum.* **77**: 064302.
- Cottrell W.J., Paquette A.D., Keymel K.R., Foster T.H., and Oseroff A.R. (2008). Irradiance-dependent photobleaching and pain in  $\delta$ -aminolevulinic acid-photodynamic therapy of superficial basal cell carcinomas. *Clin. Cancer Res.* **14**: 4475-4483.
- Cottrell W.J., Wilson J.D., and Foster T.H. (2007). Microscope enabling multimodality imaging, angle-resolved scattering, and scattering spectroscopy. *Opt. Lett.* **32**: 2348-2350.

- Dietel W., Fritsch C., Pottier R.H., and Wendenburg R. (1997) 5-aminolaevulinic-acid-induced formation of different porphyrins and their photomodifications. *Lasers Med.l Sci.* **12**: 226-236.
- Donze M., Hakvoort J.M.H., Buiteveld H., and Jaffe J. S. (1994) The optical properties of pure water. *SPIE Proc. Ocean Opt. XII.* **2258**: 174-183.
- Dougherty T.J., Gomer C.J., Henderson B.W., Jori G., Kessel D., Korbélik M., Moan J., and Peng Q. (1998) Photodynamic therapy. *J. Natl. Cancer Inst.* **90**: 889-905.
- Dougherty T.J., Kaufman J.E., Goldfarb A., Weishaupt K.R., Boyle D., and Mittleman A. (1978). Photoradiation therapy for treatment of malignant-tumors. *Cancer Res.* **38**: 2628-2635.
- Dougherty T.J., Kaufman J.E., Weishaupt K.R., Goldfarb A., Johnson R.J.R., and Lawrence, G. (1978). Photoradiation - new method for treatment of malignant disease. *Proc. Am. Assoc. Cancer Res.* **19**: 88.
- Drezek R., Dunn A., and Richards-Kortum R. (1999) Light scattering from cells: finite-difference time-domain simulations and goniometric measurements. *Appl. Opt.* **38**: 3651-3661.
- Fang H., Ollero M., Vitkin E., Kimerer L.M., Cipolloni P.B., Zaman M.M., Freedman S.D., Bigio I.J., Itzkan I., Hanlon E.B., and Perelman L.T. (2003). Noninvasive sizing of subcellular organelles with light scattering spectroscopy. *IEEE J. Quantum Electron.* **9**: 267-276.

- Fang H., Qiu L., Vitkin E., Zaman M.M., Andersson C., Salahuddin S., Kimerer L.M., Cipolloni P.B., Modell M.D., Turner B.S., Keates S.E., Bigio I., Itzkan I., Freedman S.D., Bansil R., Hanlon E.B., and Perelman L.T. (2007). Confocal light absorption and scattering spectroscopic microscopy. *Appl. Opt.* **46**: 1760-1769.
- Finlay J.C., Conover D.L., Hull E.L., and Foster T.H. (2001) Porphyrin bleaching and PDT-induced spectral changes are irradiance dependent in ALA-sensitized normal rat skin *in vivo*. *Photochem. Photobiol.* **73**: 54-63.
- Finlay J.C., and Foster T.H. (2004). Effect of pigment packaging on diffuse reflectance spectroscopy of samples containing red blood cells. *Opt. Lett.* **29**: 965-967.
- Finlay J.C., and Foster T.H. (2004). Hemoglobin oxygen saturations in phantoms and *in vivo* from measurements of steady-state diffuse reflectance at a single, short source-detector separation. *Med. Phys.* **31**: 1949-1959.
- Finlay J.C., and Foster T.H. (2005). Recovery of hemoglobin oxygen saturation and intrinsic fluorescence with a forward-adjoint model. *Appl. Opt.* **44**: 1917-1933.
- Finlay J.C., Mitra S., and Foster T.H. (2002) *In vivo* mTHPC photobleaching in normal rat skin exhibits unique irradiance-dependent features. *Photochem. Photobiol.* **75**: 282-288.
- Freitas I. (1990). Lipid-Accumulation - the common feature to photosensitizer-retaining normal and malignant-tissues. *J. Photochem. Photobiol. B, Biol.* **7**: 359-361.



- Gardner C.M., Jacques S.L., Welch A.J. (1996). Fluorescence spectroscopy of tissue: Recovery of intrinsic fluorescence from measured fluorescence. *Appl. Opt.* **35**: 1780-1792.
- Gee K.R., Brown K.A., Chen W.N., Bishop-Stewart J., Gray D., and Johnson I. (2000). Chemical and physiological characterization of fluo-4  $\text{Ca}^{2+}$ -indicator dyes. *Cell Calcium*. **27**: 97-106
- Georgakoudi I., and Foster T.H. (1998) Singlet oxygen- versus nonsinglet oxygen-mediated mechanisms of sensitizer photobleaching and their effects on photodynamic dosimetry. *Photochem. Photobiol.* **67**: 612-625.
- Georgakoudi I., Nichols M.G., and Foster T.H. (1997) The mechanism of Photofrin<sup>®</sup> photobleaching and its consequences for photodynamic dosimetry. *Photochem. Photobiol.* **65**: 135-144.
- Gomer C.J. (1991) Preclinical examination of 1<sup>st</sup> and 2<sup>nd</sup> generation photosensitizers used in photodynamic therapy. *Photochem. Photobiol.* **54**: 1093-1107.
- Hak Won J., Cottrell W.J., Foster T.H., and Yule D.I. (2007).  $\text{Ca}^{2+}$  release dynamics in parotid and pancreatic exocrine acinar cells evoked by spatially limited flash photolysis. *Am. J. Physiol. Gastrointest Liver Physiol.* **293**: G1166-G1177.
- Heney L.G., and Greenstein J.L. (1941) Diffuse radiation in the galaxy. *Astrophys. J.* **93**: 70-83.
- Jacques S.L., and Mcauliffe D.J. (1991) The melanosome - threshold temperature for explosive vaporization and internal absorption-coefficient during pulsed laser irradiation. *Photochem. Photobiol.* **53**: 769-775.

- Johansson A., Johansson T., Thompson M.S., Bendsoe N., Svanberg, K., Svanberg S., and Andersson-Engels S. (2006) *In vivo* measurement of parameters of dosimetric importance during interstitial photodynamic therapy of thick skin tumors. *J. Biomed. Opt.* **11**: 34029.
- Kennedy J.C., and Pottier R.H. (1992) Endogenous protoporphyrin-IX, a clinically useful photosensitizer for photodynamic therapy. *J. Photochem. Photobiol. B, Biol.* **14**: 275-292.
- Langmack K., Mehta R., Twyman P., and Norris P. (2001). Topical photodynamic therapy at low fluence rates - theory and practice. *J. Photochem. Photobiol. B, Biol.* **60**: 37-43.
- Lakowicz J.R. (1999). Fluorescence Sensing. In *Principles of Fluorescence Spectroscopy*, pages 531-572. Plenum Press, New York.
- Lipson R.L., Baldes E.J., Gray M.J. (1967). Hematoporphyrin derivative for detection and management of cancer. *Cancer.* **20**: 2255-2257.
- Liu H., Beauvoit B., Kimura M., and Chance B. (1996). Dependence of tissue optical properties on solute-induced changes in refractive index and osmolarity. *J. Biomed. Opt.* **1**: 200-210.
- Liu Y., Li X., Kim Y.L., and Backman V. (2005). Elastic backscattering spectroscopic microscopy. *Opt. Lett.* **30**: 2445-2447.
- Lopez R.F.V., Lange N., Guy R., and Bentley M.V.L.B. (2004) Photodynamic therapy of skin cancer: controlled drug delivery of 5-ALA and its esters. *Adv. Drug Del. R.* **56**: 77-94.

- Lou P.J., Jager H.R., Jones L., Theodosy T., Bown S.G., and Hopper C. (2004). Interstitial photodynamic therapy as salvage treatment for recurrent head and neck cancer. *Br. J. Cancer*. **91**: 441-446.
- Malik Z., and Lugaci H. (1987). Destruction of erythroleukemic cells by photoactivation of endogenous porphyrins. *Br. J. Cancer*. **56**: 589-595.
- McCray J.A., and Trentham D.R. (1989). Properties and uses of photoreactive caged compounds. *Annu. Rev. Biophys. Biophys. Chem.* **18**: 239-270.
- Mishchenko M.I., Travis L.D., and Lacis A.A. (2002). Scattering, absorption, and emission of light by small particles. Cambridge University Press, New York.
- Moan J., and Peng Q. (2003). An outline of the hundred-year history of PDT. *Anticancer Res.* **23**: 3591-3600.
- Mourant J.R., Freyer J.P., Hielscher A.H., Eick A.A., Shen D., and Johnson T.M. (1998). Mechanisms of light scattering from biological cells relevant to noninvasive optical-tissue diagnostics. *Appl. Opt.* **37**: 3586-3593.
- Mourant J.R., Johnson T.M., Carpenter S., Guerra A., Aida T., and Freyer J.P. (2002). Polarized angular dependent spectroscopy of epithelial cells and epithelial cell nuclei to determine the size scale of scattering structures. *J. Biomed. Opt.* **7**: 378-387.
- Muller M.G., Georgakoudi I., Zhang Q.G., Wu J., and Feld M.S. (2001). Intrinsic fluorescence spectroscopy in turbid media: disentangling effects of scattering and absorption. *Appl. Opt.* **40**: 4633-4646.

- Musser D.A., Wagner J.M., Weber F.J., and Dattagupta N. (1980). The binding of tumor localizing porphyrins to a fibrin matrix and their effects following photoirradiation. *Res. Commun. Chem. Pathol. Pharmacol.* **28**: 505-525.
- Perelman L.T., Backman V., Wallace M., Zonios G., Manoharan R., Nusrat A., Shields S., Seiler M., Lima C., Hamano T., Itzkan I., Van Dam J., Crawford J.M., and Feld, M.S. (1998) Observation of periodic fine structure in reflectance from biological tissue: A new technique for measuring nuclear size distribution. *Phys. Rev. Lett.* **80**: 627-630.
- Reszka K.J., Bilski P., Chignell C.F., Hartley J.A., Khan N., Souhami R.L., Mendonca A.J., and Lown J.W. (1992) Photosensitization by anticancer agents. mechanisms of photosensitization of human leukemic-cells by diaminoanthraquinones - singlet oxygen and radical reactions. *J. Photochem. Photobiol. B, Biol.* **15**: 317-335.
- Robinson D.J., de Bruijn H.S., van der Veen N., Stringer M.R., Brown S.B., and Star W.M. (1998). Fluorescence photobleaching of ALA-induced protoporphyrin IX during photodynamic therapy of normal hairless mouse skin: The effect of light dose and irradiance and the resulting biological effect. *Photochem. Photobiol.* **67**:140-149.
- Robinson D.J., de Bruijn H.S., van der Veen N., Stringer M.R., Brown S.B., and Star W.M. (1999). Protoporphyrin IX fluorescence photobleaching during ALA-mediated photodynamic therapy of UVB-induced tumors in hairless mouse skin. *Photochem. Photobiol.* **69**: 61-70.
- Salva K.A. (2002). Photodynamic therapy: Unapproved uses, dosages, or indications. *Clin. Dermatol.* **20**: 571-581.

- Schuele G., Vitkin E., Huie P., O'Connell-Rodwell C., Palanker D., and Perelman L.T. (2005). Optical spectroscopy noninvasively monitors response of organelles to cellular stress. *J. Biomed. Opt.* **10**: 051404.
- Stefanidou M., Tosca A., Themelis G., Vazgiouraki E., and Balas C. (2000). *In vivo* fluorescence kinetics and photodynamic therapy efficacy of delta-aminolevulinic acid-induced porphyrins in basal cell carcinomas and actinic keratoses; implications for optimization of photodynamic therapy. *Eur. J. Dermatol.* **10**: 351-356.
- Straub S.V., Giovannucci D.R., and Yule D.I. (2000). Calcium wave propagation in pancreatic acinar cells: functional interaction of Inositol 1,4,5,-triphosphate receptors, ryanodine receptors, and mitochondria. *J. Gen. Physiol.* **10**: 547-559.
- Thompson M.S., Johansson A., Johansson T., Andersson-Engels S., Svanberg S., Bendsoe N., and Svanberg K. (2005). Clinical system for interstitial photodynamic therapy with combined on-line dosimetry measurements. *Appl. Opt.* **44**: 4023-4031.
- Tsien R.Y. (1989). Fluorescent indicators of ion concentration. In *Fluorescence microscopy of living cells in culture*, pages 127-156. Taylor D.L., and Wang Y., editors. Academic Press, New York.
- Wang K.K-H., Cottrell W.J., Mitra S., Oseroff A.R., and Foster T.H. (2008). Simulations of measured photobleaching kinetics in human basal cell carcinomas suggest blood flow reductions during ALA-PDT. *Phys. Med. Biol.* (submitted).

- Wang S. S-H., and Augustine G.J. (1995). Confocal imaging and local photolysis of caged compounds: dual probes of synaptic function. *Neuron*. **15**: 755-760.
- Wax A., Yang C.H., Backman V., Badizadegan K., Boone C.W., Dasari R.R., and Feld M.S. (2002). Cellular organization and substructure measured using angle-resolved low-coherence interferometry. *Biophys. J.* **82**: 2256-2264.
- Wilson B.C., Olivo M., and Singh G. (1997). Subcellular localization of Photofrin<sup>®</sup> and aminolevulinic acid and photodynamic cross-resistance *in vitro* in radiation-induced fibrosarcoma cells sensitive or resistant to photofrin-mediated photodynamic therapy. *Photochem. Photobiol.* **65**: 166-176.
- Wilson B.C., Patterson M.S., and Lilge L. (1997). Implicit and explicit dosimetry in photodynamic therapy: a new paradigm. *Lasers Med. Sci.* **12**: 182-199.
- Wilson J.D., Bigelow C.E., Calkins D.J., and Foster T.H. (2005). Light scattering from intact cells reports oxidative-stress-induced mitochondrial swelling. *Biophys. J.* **88**: 2929-2938.
- Wilson J.D., and Foster T.H. (2005). Mie theory interpretations of light scattering from intact cells. *Opt. Lett.* **30**: 2442-2444.
- Wilson J.D., Cottrell W.J., and Foster T.H. (2007). Index of refraction-dependant sub-cellular light scattering observed with organelle-specific dyes. *J. Biomed. Opt.* **12**: 014010.
- Wu J., Feld M.S., and Rava R.P. (1993). Analytical Model for Extracting Intrinsic Fluorescence in Turbid Media. *Appl. Opt.* **32**: 3585-3595.

- Yano T., Muto M., Minashi K., Ohtsu A., and Yoshida S. (2005). Photodynamic therapy as salvage treatment for local failures after definitive chemoradiotherapy for esophageal cancer. *Gastrointest. Endosc.* **62**: 31-36.
- Yu C.C., Lau C., Tunnell J.W., Hunter M., Kalashnikov M., Fang-Yen C., Fulghum S.F., Badizadegan K., Dasari R.R., and Feld M.S. (2006). Assessing epithelial cell nuclear morphology by using azimuthal light scattering spectroscopy. *Opt. Lett.* **31**: 3119-3121.
- Zeitouni N.C., Oseroff A.R., and Shieh S. (2003). Photodynamic therapy for nonmelanoma skin cancers - current review and update. *Mol. Immunol.* **39**: 1133-1136.

## Chapter 2

### Portable instrumentation for photodynamic therapy of cutaneous disease

#### 2.1 Introduction

Dosimetry during photodynamic therapy (PDT) is an ongoing challenge.

Despite a number of advantages PDT demonstrates over competing treatment modalities, this obstacle has slowed the general acceptance of PDT into mainstream use in oncology. In contrast to radiotherapy, where dose is specified by energy absorption per unit mass of tissue, the PDT community does not have a generally-accepted definition of dose. Though it is known that reactive oxygen species such as singlet oxygen,  $^1\text{O}_2$ , generated through the PDT reaction,



are the predominant cytotoxic species involved in tumor cell killing, neither monitoring  $^1\text{O}_2$  nor the explicit parameters governing its production are clinically accessible.

Though photodynamic action occurs in all areas where photosensitizer, light, and oxygen are present, the interaction among these quantities complicates quantitative dosimetry, sometimes in counterintuitive ways. For example, it has been demonstrated that as the fluence rate is increased, the PDT reaction is driven faster and more oxygen is consumed (Foster *et al.*, 1991). At sufficiently high fluence rates oxygen consumption can outpace that supplied by diffusion from capillaries. This can consequently produce hypoxic regions and attenuate PDT in these volumes (Foster and Gao, 1992). This effect has been verified in basal cell carcinoma (BCC) patients undergoing Photofrin<sup>®</sup>-PDT, where transient, treatment induced tumor hypoxia was observed during PDT delivered at  $150 \text{ mW cm}^{-2}$ , while oxygenation was maintained with the lower fluence rate of  $30 \text{ mW cm}^{-2}$  (Henderson *et al.*, 2000).

A number of preclinical cancer models used in this laboratory, including spheroid and animal models, have directly investigated the role of oxygen consumption in PDT (Foster *et al.*, 1991; Georgakoudi and Foster, 1998). The resulting oxygen dynamics showed that PDT delivered at lower irradiances and,

alternatively, where fractionated light delivery was used, preserved oxygen and improved treatment efficacy. Nevertheless, as previously mentioned current clinical PDT treatment protocols typically prescribe a photosensitizer concentration, incident fluence, and the drug-light interval. PDT treatments delivered under this prescription, though easy to implement, have proven inconsistent in predicting treatment efficacy (Peng *et al.*, 1997). These protocols fail to account for lesion-to-lesion heterogeneities in both optical properties and lesion histology. They also do not consider that PDT is a dynamic and multivariable process during which oxygen concentrations, photosensitizer concentration, and even the fluence rate within the treatment volume may vary. Furthermore, this definition fails to interpret a host of treatment inconsistencies brought about by treatment fluence rate, delivery fractionation, excitation wavelength, photosensitizer redistribution, and tumor morphology and vascularization.

Alternately, some researchers have used dosimetry based on  $^1\text{O}_2$  directly. Though luminescence from  $^1\text{O}_2$  can be detected at a wavelength of 1270 nm, as mentioned, the transition is forbidden and the resulting weak signal may prove impractical for current clinical application (Adamson, 1979; Niedre *et al.*, 2003).

PDT optimization using explicit dosimetry has been employed in the clinical arena only in limited cases, mainly as the result of the technical complexity of monitoring tissue oxygenation, drug concentration, and the fluence of the treatment source. Measuring optical fluence and fluence rate during therapy has received recent attention because these parameters are easily adjusted in the treatment, are often accessible, and are difficult to accurately gauge *a priori* due to backscattering and reflections (Jacques, 1992). For example, fluence monitoring has been used to help protect healthy tissue in hollow organs during PDT treatments of esophageal cancer and Barrett's esophagus (Bays *et al.*, 1997; Boere *et al.*, 2002; Boere *et al.*, 2003; van Veen *et al.*, 2002), bladder (vanStaveren *et al.*, 1996), and bronchi (Murrer *et al.*, 1997). It has also been used interstitially where the measurements are most accurate (Marijnissen and Star, 2002; Thompson *et al.*, 2005). Tumor oxygenation status has been explored using polarographic needle electrodes (Henderson *et al.*, 2000), phosphorescence quenching (Cerniglia *et al.*, 1997; Vinogradov *et al.*, 1996), and nitroaromatic binding (Nunn *et al.*, 1995). These techniques, however, are complicated and invasive, making them clinically prohibitive.

As mentioned above, photosensitizers typically kill by the production of  $^1\text{O}_2$ . For the majority of photosensitizers, however, excited oxygen species can also act on the sensitizer itself, irreversibly degrading it through the process of

photosensitizer photobleaching. Photobleaching therefore has the potential to indirectly report on unobservable  $^1\text{O}_2$  reactions. This photobleaching dependence on oxygen availability has prompted several studies investigating the irradiance dependence of photobleaching and its relationship to therapeutic outcome (Boere *et al.*, 2002; Finlay *et al.*, 2001; Langmack *et al.*, 2001; Robinson *et al.*, 1998; Robinson *et al.*, 1999).

In addition to providing corrections to fluorescence spectra, reflectance spectroscopy has the ability to monitor tissue absorption and scattering properties. This allows the extraction of oxy- and deoxyhemoglobin concentrations and consequently changes to blood volume and blood oxygenation saturation, which have a direct impact on oxygen availability during PDT (Hull *et al.*, 1999). A variety of instrumentation has been presented by this group and others which is capable of investigating tissue optics for reflectance and fluorescence spectroscopy acquisition. Probes specifically designed for PDT dosimetry have been described for transcutaneous (Marijnissen and Star, 2002) and esophageal measurements (Bays *et al.*, 1997; Murrer *et al.*, 1997; van Veen *et al.*, 2002). In this laboratory, optical properties of tissue have been determined in pre-clinical models through radially-resolved diffuse reflectance (Hull *et al.*, 1999; Nichols *et al.*, 1997), and white-light diffuse reflectance spectroscopy has accurately determined blood oxygen

saturation and blood volume using a single source-detector separation and  $P_3$  theory *in vivo* (Finlay and Foster, 2004). The reflectance measurements presented here make use of large coincident source-detector geometries, which are not addressable using the standard analytical models. A scaled Monte Carlo (MC) stochastic model is therefore employed, which explicitly accounts for the measurement geometry yet allows data fitting in a reasonable timeframe (Kienle and Patterson, 1996).

In this chapter, we describe a portable clinical instrument for delivering PDT while performing non-invasive spectroscopic monitoring *in vivo*. Monitoring PpIX photobleaching and blood oxygen saturation during PDT allows improved interpretation of clinical results and is helping guide the treatment protocol for an anticipated low-irradiance PDT clinical trial of sBCC. The instrumentation has been incorporated into clinical trials at Roswell Park Cancer Institute (RPCI) involving ALA-PDT of sBCC.

## **2.2 Methods and instrumentation**

The design of the instrumentation presented in this chapter was heavily influenced by restrictions imposed by the clinical protocol at RPCI. This protocol required that the treatment beam be delivered through a 600  $\mu\text{m}$ -core fiber, terminated with a GRIN lens and housed in an off-surface probe

positioned 80 mm from the lesion. Additionally, data was acquired at two spatially-resolved measurement fields; one field was located inside the lesion and the other was located within the adjacent perilesion margin. The system was engineered as a portable, cart-based instrument with push-button automation. It captured fluorescence and reflectance spectra during a pilot clinical trial of  $\delta$ -aminolevulinic acid (ALA)-PDT treatment of sBCC.

Using an off-surface probe, the instrument delivered the treatment beam to a user-defined field and performed reflectance and fluorescence spectroscopies. The instrument was used to monitor photosensitizer fluorescence photobleaching, fluorescent photoproduct kinetics, and hemoglobin oxygen saturation. Fluorescence generated from protoporphyrin IX (PpIX) and photoproduct I excited by the 632.8 nm PDT treatment laser was collected between 665 and 775 nm. During a series of brief treatment interruptions at programmable time points, white-light reflectance spectra between 475 and 775 nm were acquired. Fluorescence spectra were corrected for the effects of absorption and scattering, informed by the reflectance measurements. They were then decomposed into known fluorophore contributions in real time using a robust singular-value decomposition (SVD) fitting routine (Press *et al.*, 1992). Analysis of reflectance spectra using a nonlinear fitting algorithm additionally provided information on hemoglobin oxygen saturation.

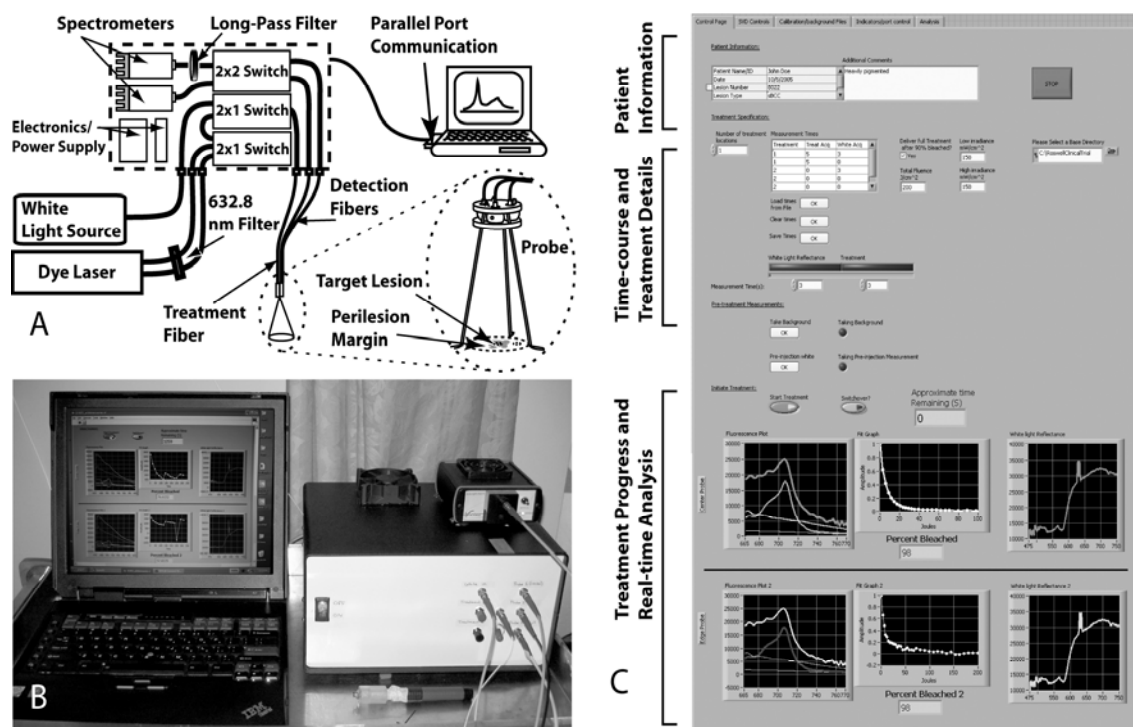


Figure 2.1: (A) Schematic illustration and (B) photograph of the computer-controlled clinical instrumentation developed for Roswell Park Cancer Institute. The instrument consists of two 2x1 opto-mechanical switches that control delivery of the treatment beam and white-light to the tissue through an off-surface probe. A 2x2 switch is also used to direct subsequent fluorescence and reflectance signals to a pair of thermoelectrically-cooled spectrometers. (C) User interface for instrumentation developed in LabVIEW. The user inputs patient information and the PDT treatment time course, consisting of treatment and acquisition intervals in a spreadsheet format. Acquisition of baseline information such as dark signal and initial reflectance spectra are also initiated by the user. During the treatment, white-light reflectance spectra and SVD-analyzed fluorescence spectra are displayed in near real-time to the clinician. Additionally, the program displays the progression of the PpIX bleaching from two detection regions as each fluorescence spectrum is analyzed.

### **2.2.1 Instrument specification**

The system utilized two light sources: the treatment source consisted of an argon-ion-pumped dye laser (Coherent Inc., Santa Clara, CA), which was band-pass filtered (NF01-633U-25, Semrock, Rochester, NY) to operate at 632.8 nm and split into a low- and high-power fiber channel; the white-light reflectance source consisted of a SMA-coupled tungsten-halogen source with an internal TTL shutter (AvaLight-HAL, Avantes, Boulder, CO). Band-pass filtering the treatment source minimized source bleed-through into the fluorescence detection channel when spectra were acquired. Both the low- and high-power output fibers were coupled into a first 2x1 fiber-optic switch. During the initial construction of this instrument, the large-diameter fiber optics switches were manufactured in our laboratory as described below. These switches were subsequently replaced with high performance commercial switches as they became available. The output of the first 2x1 switch and the white-light source were next coupled to a second 2x1 switch whose output channel was the 600  $\mu\text{m}$ -core treatment fiber, the distal end of which was mounted in a tripod probe with a beam-aiming bearing adjustment. Two microlens-terminated detection fibers were also positioned in the probe and coupled into a 2x2 fiber switch, enabling switching between fluorescence and reflectance spectroscopy in both the sBCC lesion and perilesion margin. Fluorescence was transmitted through a 645 nm long-pass filter (E645LP, Chroma Technology Corp.,



Rockingham, VT) and directed to a spectrometer, which measured fluorescence spectra between 665 and 775 nm with 3 nm resolution (BTC-111-OEM, BWTek Inc, Newark, DE). Reflectance spectra taken in the same delivery-detection geometry were similarly directed to a second spectrometer, which measured between 475 and 775 nm with 3 nm resolution. Both spectrometers were thermoelectrically (TE)-cooled, 16-bit devices with 0.22 numerical aperture SMA fiber input couplings. Fluorescence spectra were corrected for dark counts acquired prior to therapy and also corrected for the instrument response using a broadband NIST-traceable calibration lamp (LS-1-Cal, Ocean Optics, Dunedin, FL). A LabVIEW (National Instruments, Austin, TX) program on a laptop computer controlled source delivery, data collection, and performed real-time spectral analysis and display.

### **2.2.2 Probe specification**

The fluorescence/reflectance probe was designed to measure tissue fluorescence and white-light reflectance in identical geometries and is shown in Figure 2.2. The treatment beam was delivered through a 600  $\mu\text{m}$  core, UV-VIS step-index fiber with a numerical aperture of 0.39 (BFH39-600, Thor Labs Inc., Newton, NJ). The distal end of this fiber was coupled to a 1.8 mm diameter, 0.25 pitch GRIN lens optimized for 630 nm (LGI630-3, Newport Corp., Irvine CA) and seated within a 3 mm-diameter aluminum tube. This lens-fiber combination

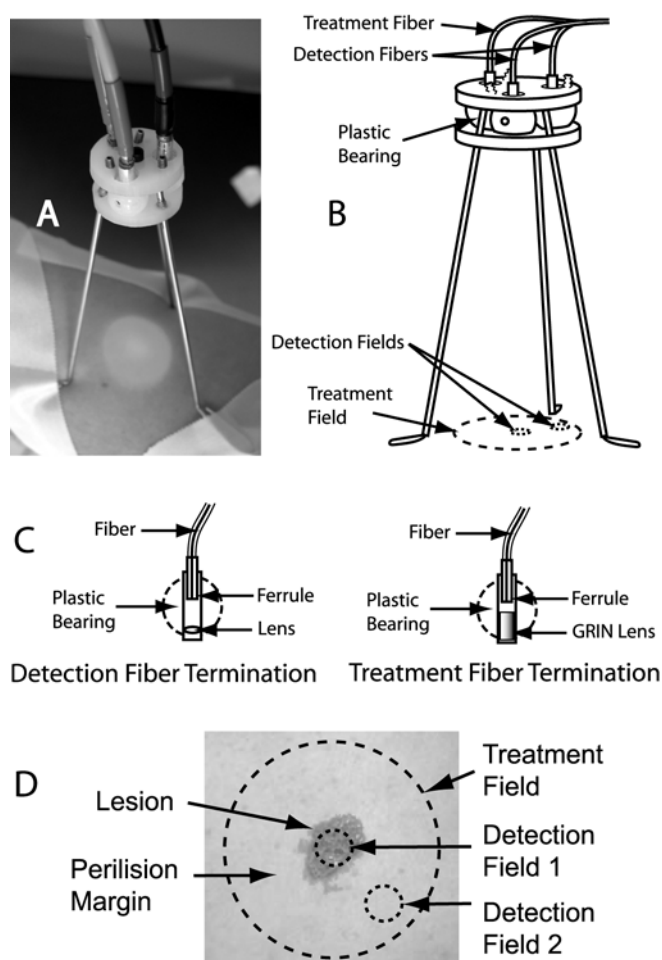


Figure 2.2: (A) Photograph and (B) illustration of the off-surface fiber optic probe. (C) A single GRIN-terminated treatment fiber and two lens-terminated detection fibers are shown housed in plastic bearings, which are used for beam aiming. (D) Representative placement of treatment and detection fields on a depiction of a sBCC lesion with detection from both the cancerous (detection field 1) and normal tissue (detection field 2) in the adjacent perilesion margin.

resulted in a 0.15 NA for the treatment beam. Similarly, the detection channels of the system consisted of 365  $\mu\text{m}$  core, UV-VIS step-index fibers with numerical apertures of 0.22 (BFH22-365, Thor Labs) and terminated with 3 mm diameter, 6.7 mm focal length lenses (Edmund Optics Inc., Barrington, NJ) in 4 mm-diameter aluminum housing tubes. This lens-fiber combination resulted in detection optics with a 0.02 NA. The probe housing consisted of two flat aluminum disks approximately 20 mm in diameter and 2 mm thick, milled with sockets for bearing placement. Three 10 mm-diameter plastic bearings were milled with through holes and compressed between the disks to form a friction fit with the sockets. The treatment and detection fibers were fixed into these bearings to provide continuous aiming adjustments to the detection and source fields. These bearings were locked in place with set screws prior to starting the therapy. Small-gauge steel tubing was used to create three probe legs that were terminated with wire loops and allowed the probe to be fixed to the patient with medical tape. With the probe head positioned 80 mm from the skin the treatment field measured 25 mm in diameter and had uniform irradiance across the field  $\pm 2\%$ . Each detection field measured 4 mm in diameter. The 25 mm treatment field allowed PDT of lesions up to 15 mm across with at least a 5 mm perilesion margin. Prior to treatment, the treatment and detection fields were properly oriented on the lesion using a trace beam, which was generated from a modified laser pointer directed through the treatment and detection fibers.

During alignment the treatment beam was centered on the lesion, and the first of the two detection fields was centered concentrically. The second detection field was placed just outside the primary lesion on normal tissue in the adjacent perilesion margin, as illustrated in Figure 2.2D.

### **2.2.3 Switch design**

In order to maintain identical geometries for fluorescence and reflectance measurements and keep the optical probe simple, the treatment and white-light sources were sent through the same treatment fiber. Similarly, detection of the fluorescence and reflectance signals from the lesion and perilesion fields was performed using only two detection fibers. This increased system functionality was obtained by integrating fiber optic switches into the system. At the time of initial construction, multimode switches compatible with large-core fibers, high power throughput, and good transmission over a wide spectral range were not readily available. We therefore constructed multimode switches of our own design, as illustrated in Figure 2.3.

To build each of the two delivery arm 2x1 switches, three 600  $\mu\text{m}$  core fibers were SMA terminated, and the distal ends were epoxied into small diameter steel tubing, the ends of which were then polished. A 3x5 inch switch housing was machined out of anodized aluminum, and a precision, low friction, micro-

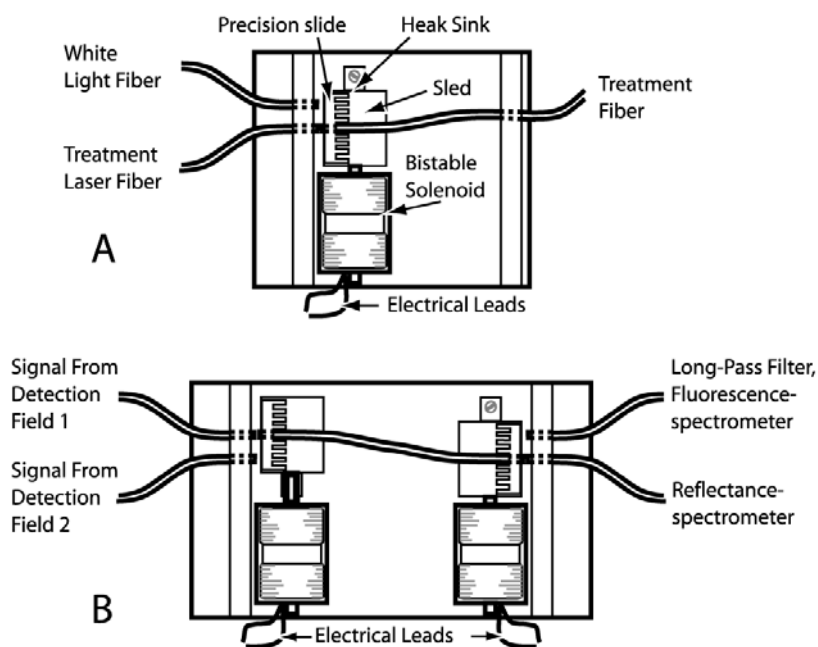


Figure 2.3: Custom (A) 2x1 and (B) 2x2 fiber optic switches. Optical paths are separated by mechanical displacement using latching solenoids to push a sled along a precision slide. High signal to noise switching is repeatable using large core diameter fibers. The addition of a heat-sinking baffle allows high power handling during operation.

slide (DP Miniature, Del-Tron, Bethel, CT) was mounted onto the base. An anodized aluminum sled was attached to the slide and driven with a bi-directional latching solenoid (S-18-100L, Magnetic Sensor Systems, Van Nuys, CA) with approximately 4 mm linear translation. The output fiber was mounted to the sled with clear epoxy, and the first input fiber was aligned with a micrometer while optimizing switch throughput of a coupled HeNe laser beam. The first fiber was then epoxied in place, and the process was repeated for the second fiber with the solenoid in its second stable position. An anodized heat sink was included on the sled in order to reduce fiber cross-talk and misalignment from heating caused by blocking the intense treatment beam during white-light measurements. The 2x2 switch for the detection arm of the system was constructed using similar techniques but required two solenoid switching mechanisms.

Insertion loss of the 2x1 switches using 600  $\mu\text{m}$  core fibers was approximately 1.5 dB for 632.8 nm light, and 2.2 dB for the 365  $\mu\text{m}$  fiber 2x2 switch. In both cases, the cross-talk of the switches was less than -45 dB, and repeatability throughput of the switching cycles was roughly 0.09 dB. The 2x2 switch demonstrated a slightly higher efficiency per single switching unit over the 2x1 switch. This increase was likely due to the lower numerical aperture of the

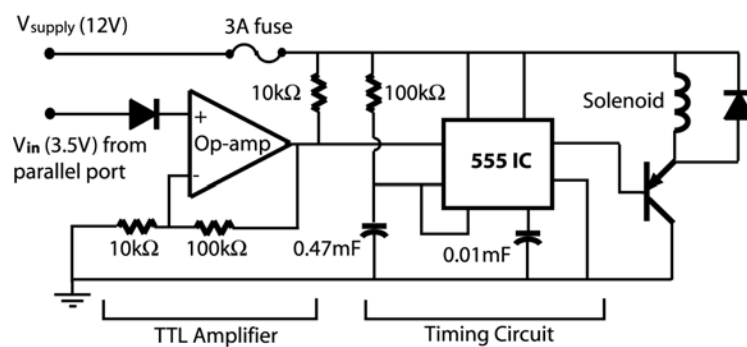


Figure 2.4: Switch driver circuitry. Circuitry used to condition 3.5 V, 50 mA signals received from the laptop computer to produce 50 ms, 12 V, 2 A pulses to drive the fiber switches.

optical fiber since no focusing optics were used. The switching times required to toggle between states was approximately 20 ms.

#### **2.2.4 System control and operation**

A laptop computer (Thinkpad A51, IBM Corp., White Plains, NY) ran a GUI-interfaced LabVIEW system control of our own design. Communication with the two spectrometers was performed through USB ports, while control of the switches and the white-light shutter was accomplished through the computer's parallel port, interfaced to a prototype electronics board with amplification circuitry. The circuit, shown in Figure 2.4, was triggered by the 3.5 V TTL outputs of the parallel port and drove the solenoids with a 12 V, 2 A pulse for a duration of approximately 50 ms.

The LabVIEW interface, shown in Figure 2.1C, contained fields for patient and lesion information as well as a spreadsheet in which the operator specified details of the treatment, including time points for fluorescence and reflectance spectral acquisitions, spectroscopic integration times, and target treatment fluence and fluence rates. After the treatment was initiated, the instrument cycled through several steps, illustrated in Figure 2.5. In the first cycle, the treatment beam was delivered to the entire 25 mm treatment region, including lesion and perilesion margin, while a fluorescence spectrum was collected from



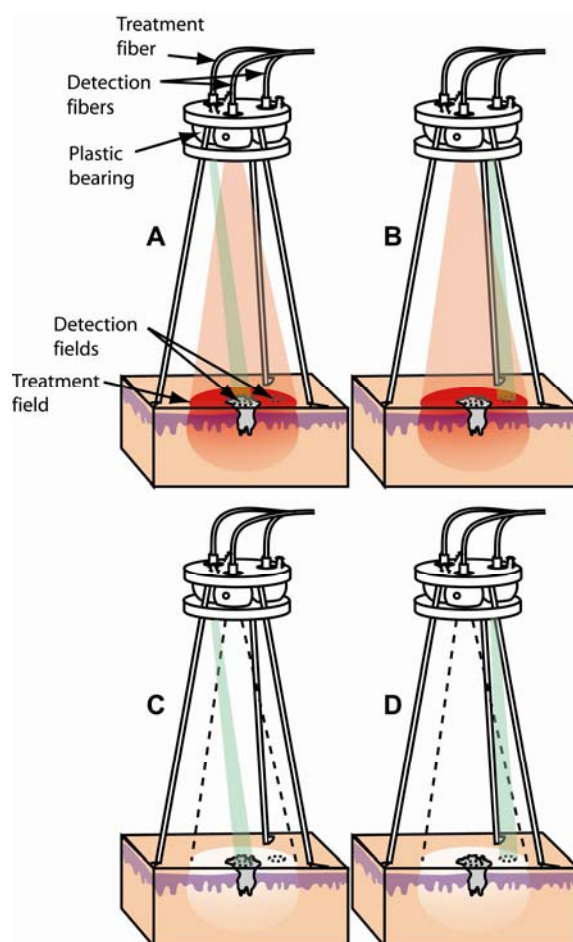


Figure 2.5: Treatment and measurement cycles during clinical PDT system operation include (A) PDT delivery at 632.8 nm (red) with fluorescence monitoring (green) in the lesion, (B) PDT delivery with fluorescence monitoring in the perilesion margin, (C) white-light interrogation (dashed) with reflectance monitoring in the lesion, and (D) white-light interrogation with reflectance monitoring in the margin.

the lesion. In the next cycle, the treatment beam remained on and fluorescence was collected from the margin. For the subsequent two cycles, the white-light channel was opened in the second 2x1 switch, and white-light was delivered to the same treatment region through the treatment fiber. Reflectance spectra were captured from the lesion and perilesion margin, sequentially, by the same detection fibers as used for fluorescence. All spectra were saved to file and displayed to the user in the LabVIEW interface.

### **2.2.5 System upgrades**

Several upgrades were made to the instrumentation during the course of the clinical trial. The most significant modification was the substitution of commercially-manufactured, piezo fiberoptic switches for the custom ones described above. Two 600/660  $\mu\text{m}$  core/cladding 2x1 switches (Piezosystem Jena, Hopedale, MA) were substituted in the delivery arm of the system. Similarly, two 400/440  $\mu\text{m}$  2x1 switches were connected serially to replace the 365  $\mu\text{m}$  2x2 switch. The new switches demonstrated improved operating characteristics, which included a 2 ms switching time, -55 dB crosstalk, repeatability of better than 0.03 dB, and 5 V TTL triggering with 100 mA current consumption. The controlling electronics were appropriately modified and these switches were driven directly from the parallel port TTL output. Additionally, a bias was added to the white-light reflectance source in order to

flatten the spectral output; a cyan filter (Rosco Laboratories, Stamford, CT) compensated for anticipated changes in the spectra due to absorption in the target volume. This reduced the dynamic range of the reflectance spectra in the visible region. The long-pass filter was also upgraded to a 647.1 nm Raman filter, which offered superior throughput and a much steeper spectral cutoff (LP02-647RU-25, Semrock, Rochester, NY). After each modification, the system was re-characterized prior to clinical use.

## **2.3 Data analysis**

### **2.3.1 Reflectance**

White-light reflectance spectroscopy provided a clinically-compatible technique that could be used to determine the optical properties of a volume of tissue and, consequently, provided a means to correct fluorescence spectra and a measure of blood oxygen saturation. Using the system outlined above, reflectance spectra between 475 nm and 775 nm were collected in the clinic separately for both lesion and margin fields. Resulting spectra were immediately used to correct fluorescence spectra, using a technique outlined below, and nonlinear fitting performed after the clinical measurements provided blood oxygen saturation in the sampled volume. White-light reflectance spectra were corrected for instrument effects by subtracting dark signals measured prior to treatment and

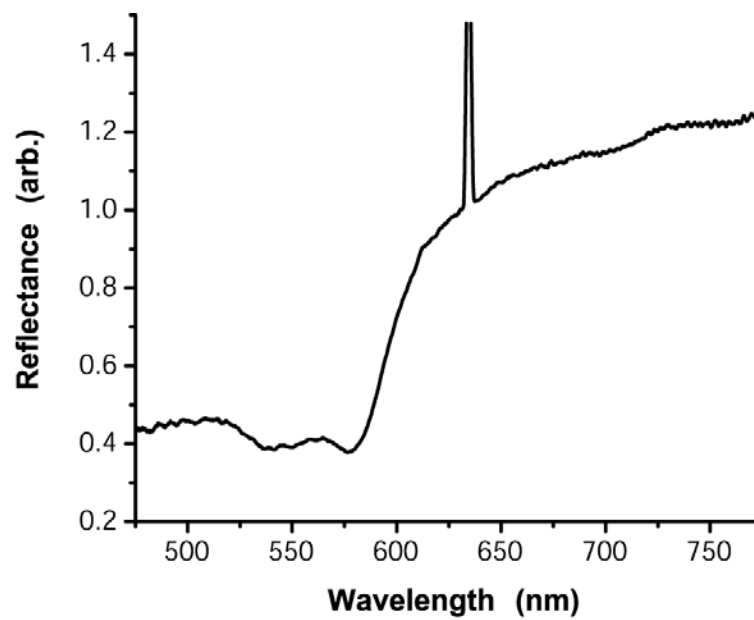


Figure 2.6: Reflectance monitored from a superficial sBCC lesion showing a peak near 632.8 nm resulting from stray laser light in the clinic due to simultaneous PDT treatments of multiple nearby lesions and fiber crosstalk.

dividing by a channel-specific sensitivity spectrum. The sensitivity spectrum was generated with a dark-signal-corrected reflectance measurement made using a diffuse reflectance standard (WS-1, Ocean Optics, Dunedin, FL). Division by this sensitivity spectrum accounted for features of the lamp, fibers, and optical switches in the optical path between the white-light source and spectrometer. A representative reflectance spectrum taken from the center of a sBCC lesion using the instrument is shown in Figure 2.6. The spectrum shows the characteristic absorption of oxyhemoglobin and a sharp peak at 632.8 nm that resulted from stray laser light in the clinic and switch crosstalk.

### **2.3.2 Nonlinear fitting of reflectance data**

Reflectance spectra were used to extract information about blood oxygen saturation. In order to model light propagation in tissue, accounting for the effects of both scattering and absorption, we employed a Monte Carlo (MC) model. MC has become a standard radiation transport model, which can be used for modeling arbitrary optical properties and geometries. Because it is a stochastic model, however, MC requires computation time that can be orders of magnitude in excess of those provided through analytic solutions and is not readily compatible with iterative data fitting routines. Therefore, we employed a scalable library-based fitting method adapted from Kienle and Patterson (1996). This method uses a lookup table and an analytical transformation of previously

generated MC simulation data, which maintains the robustness of MC and is fast enough to be used in an iterative fitting routine.

Using this technique to fit reflectance data first required generating a lookup table. This reference table consisted of absorption-scalable photon path-length distributions, which were generated at a single absorption coefficient for a range of biological reduced scattering values. The probe-specific reflectance for arbitrary absorption and scattering parameters could then be determined using this table, as further outlined below. This allowed a trial reflectance spectrum to be generated in a fitting routine from absorption and scattering spectra produced from trial chromophore concentrations and scattering parameters. Trial reflectance spectra were subsequently fit to normalized measured reflectance data using a downhill simplex algorithm.

#### **2.3.2.1 Monte Carlo for arbitrary absorption and scattering**

The MC algorithm used to propagate photons was a variation of the well-known MCML code (Wang *et al.*, 1995), which used variance reduction in photon capture and has been described in detail by Finlay (2003). After the source-detector geometry was specified, the MC routine launched randomly-distributed simulated photon packets from the specified source. A portion of this unity-weight photon packet was reflected at the air-tissue interface and the remainder

was propagated in the tissue. During propagation, the probability of absorption and scattering events was determined randomly with an exponential distribution using the mean free path. At each event the direction of the packet was randomly changed with a probability governed by the Henyey-Greenstein distribution (Equation 1.4), and the weight was reduced by a factor of the albedo (Equation 1.5). When the weight of the photon packet was below a predetermined threshold, a roulette function either terminated the photon packet (90% chance) or increased its weight by a factor of 10 and re-propagated it from that location (10% chance). This roulette was used in order to limit the simulation time spent tracking low-weight photon packets.

Photons which escaped the tissue surface and were incident on the detector were scored as reflectance photons. Their weights and path-length traveled in the tissue were recorded and provided the photon path-length distribution,  $R_{MC}(l)$ , at reference absorption and reduced scattering coefficients  $\mu_{aMC}$  and  $\mu'_{sMC}$ . Similarly, the position and weight of photons absorbed in the tissue were recorded and contributed to the absorption distribution, which is directly proportional to the fluence distribution. Data was exported to file for both the path-length and fluence distributions. Path-length data was binned by 0.25 mm path-lengths and fluence data was binned by 0.1 mm in depth and radius.

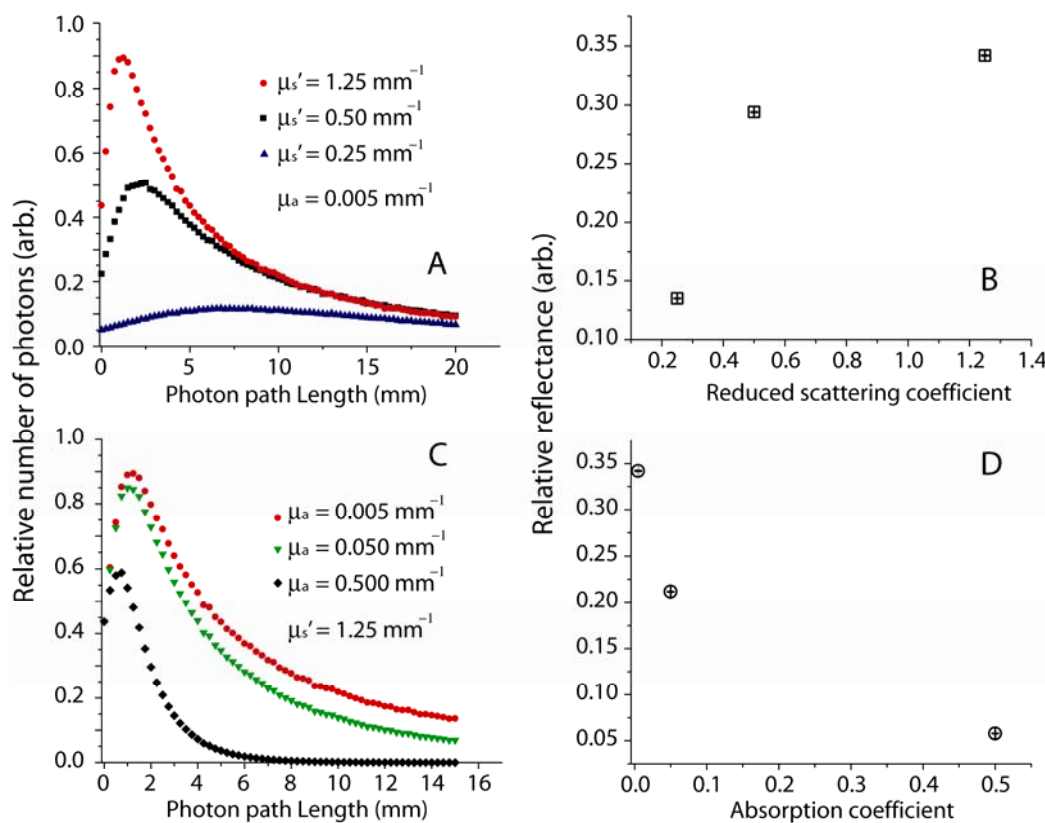


Figure 2.7: Scaled Monte Carlo path length distributions. (A) The relative number of reflectance photons scored in MC runs as a function of photon path-length for several different  $\mu_s'$  coefficients and (B) their relative contribution to the reflectance. (C) The relative number of photons calculated using Beer's law as a function of photon path length for several  $\mu_a$  and (D) their relative reflectance. The standard error bars for the reflectance contribution data are smaller than the symbols.



Representative  $R_{MC}(l)$  distributions are shown in Figure 2.7. The reflectance  $R(\mu_a)$  for arbitrary  $\mu_a$  can subsequently be calculated by applying Beer's law (Equation 1.1) to the path length distribution of  $R_{MC}(l)$  using

$$R(\mu_a) = \int_{l=0}^{\infty} R_{MC}(l) \exp[-l(\mu_a - \mu_{aMC})] dl, \quad [2.1]$$

where  $R_{MC}(l)$  is the MC reflectance signal as a function of traveled photon path length,  $l$ , generated with the absorption coefficient  $\mu_{aMC}$ . In practice MC generates binned path-length distributions and the integration of Equation 2.1 is replaced with a summation. Representative calculated photon path-length distributions for various absorption and scattering coefficients and their relative reflectance values are also shown in Figure 2.7.

Each MC simulation was run at a specific reduced scattering coefficient,  $\mu'_{sMC}$ . Therefore, in order to provide simulated data for a range of scattering coefficients, a library of  $R_{MC}(l)$  distributions was generated for the range of biological  $\mu'_{sMC}$  s. The photon path-length distribution for arbitrary reduced scattering coefficient was then calculated by linear interpolation of the path-length data in this library.

For this probe geometry, the true source of the photons was the 0.15 NA treatment fiber, which projected the 25 mm diameter treatment field on the tissue. Similarly, the detector was the 0.02 NA detector, which collected photons emitted from a 4 mm-diameter field. The etendue of the source was therefore larger than that of the detector by a factor of more than 350. Therefore, we made use of the reciprocity theorem for optical systems in our MC simulations. This theorem states that the radiance at point  $P_1$  in direction  $\mathbf{p}_1$  produced by point  $P_2$  emitting in direction  $\mathbf{p}_2$  is the same as the radiance at point  $P_2$  in direction  $-\mathbf{p}_2$  produced from point  $P_1$  emitting into direction  $-\mathbf{p}_1$ . This suggests that the path-length distribution of scored photons was identical whether photon travel was simulated from the source to the detector or backwards from the detector to the source. The difference in etendue indicated that a photon launched backwards from the detector towards the source has a higher probability of being scored than a photon launched to the detector from the source. Tracking photons in this adjoint direction, i.e. backwards from detector to source, allowed simulated path-length distributions and the resulting lookup table to be generated over 350 times faster (Crilly *et al.*, 1997).

For this probe geometry, our simulation assumed a tissue index of refraction of 1.4 and an anisotropy factor of 0.9. Simulations were run for the source-detector geometries with  $\mu'_{\text{SMC}}$  ranging from 0.25 to 4 mm<sup>-1</sup>, every 0.25 mm<sup>-1</sup>,

and the absorption for the simulation  $\mu_{aMC}$  was set at  $0.005 \text{ mm}^{-1}$ . Simulations were run for each  $\mu'_{sMC}$  until the standard error about the mean (SEM) of the reflectance signal was less than 0.1% of the average. This required launching between 10 and 100 million photon packets for each simulation. Each simulation was run at the low absorption in order to bound the error in calculated reflectance to less than 0.1% after the application of Beer's law to the path length distribution. Therefore, the simulated library values are valid for  $0.25 < \mu'_s < 4 \text{ mm}^{-1}$ , and  $0.005 \text{ mm}^{-1} < \mu_a$ .

### 2.3.2.2 Iterative fitting algorithm

The iterative fitting algorithm used to fit reflectance spectra is illustrated in Figure 2.8 and consisted of three fundamental stages. The first stage of the algorithm was a guess of the fit parameters. This was a 9-dimensional trial vector of the concentrations of oxy- and deoxyhemoglobin, melanin, and water, in addition to two values defining the scattering spectrum, specular reflectance, contribution from fluorescent room lighting, and a scaling factor. Initially, the values were seeded by the user but subsequent iterations were provided by the underlying iterative algorithm, outlined below.

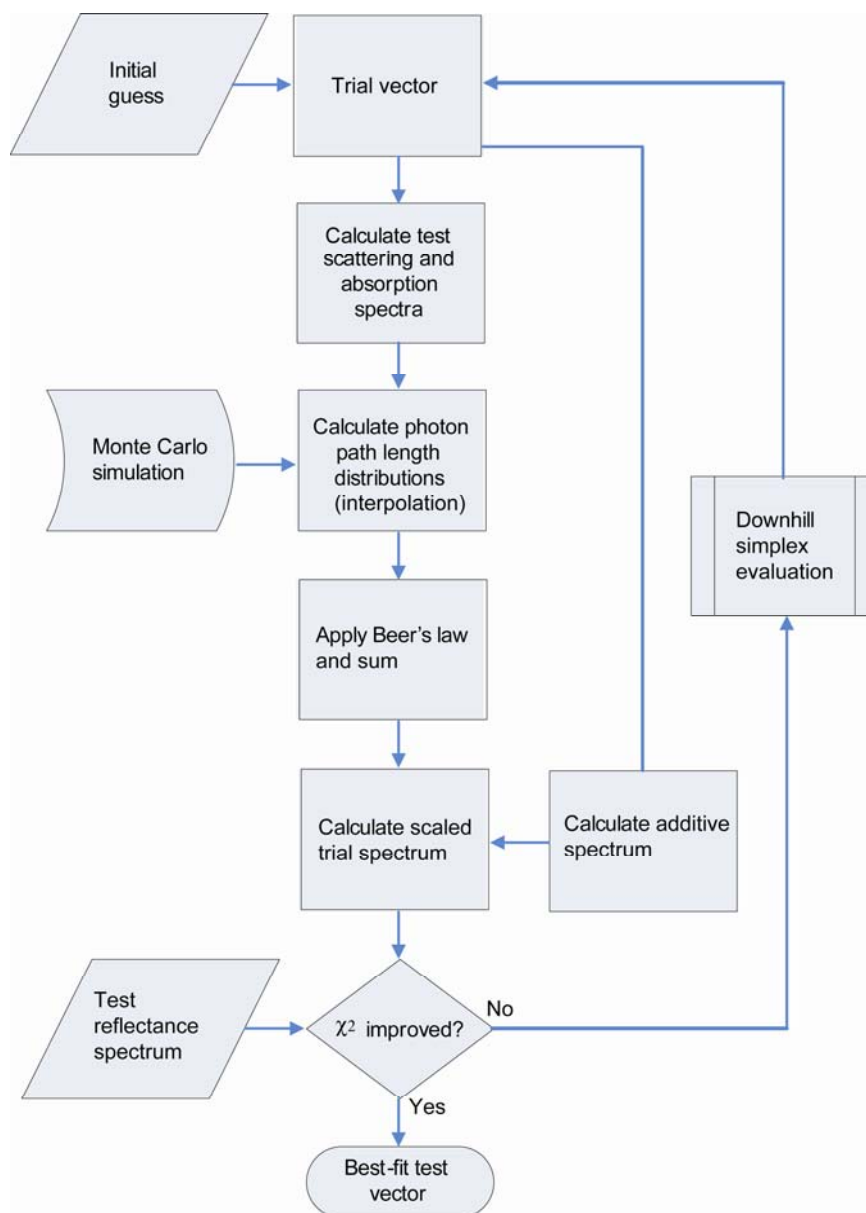


Figure 2.8: Flow diagram of the scaled Monte Carlo (MC) fitting routine. The initial guess solution vector was fed into the downhill simplex algorithm which generated a solution volume. As the simplex collapses onto the best-fit solution, each proposed vector solution was used to generate a test spectrum using Beer's law and a scaled MC library, specific to the test geometry.

In the second stage of the algorithm, the trial vector was used to generate a test reflectance spectrum. This was done in a series of steps. A scattering spectrum and absorption spectrum were constructed using the scattering parameters and chromophore concentrations, according to Equations 1.6 and 1.7. For each wavelength interval in the spectrum, the relative reflectance was calculated using this data. As mentioned previously, this was accomplished by finding the appropriate path length distribution for a particular  $\mu'_s$  using the lookup table, adjusting the reflectance contribution for each path length using Beer's law, and then summing the contribution at each path length. In addition, an additive offset spectrum was included using a trial specular reflectance value that was multiplied by the calibration lamp response and a trial room light value that multiplied by the reference room light spectrum. The resulting trial spectrum was therefore the relative reflectance spectrum added to the offset spectrum and multiplied by the trial vector scaling parameter, which accounted for normalization of the test spectrum.

In the third step of the algorithm, this trial spectrum was compared to the normalized test reflectance spectrum, and the trial vector parameters were adjusted. This algorithm used a multidimensional downhill simplex routine based on function evaluation (Press *et al.*, 1992). When minimizing a function in N-dimensional space, this routine took an initial guess of N+1 vertices

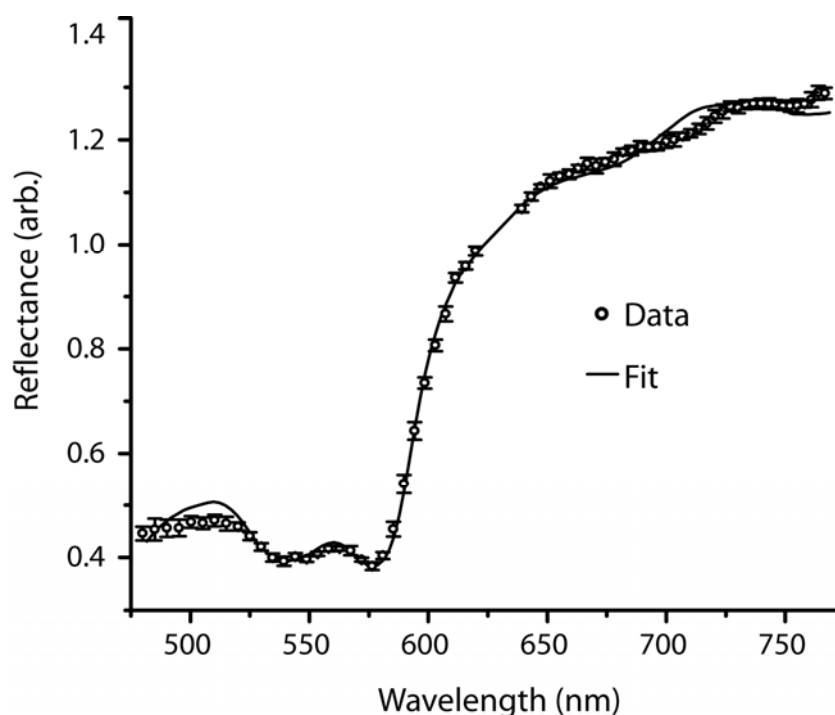


Figure 2.9: White-light reflectance spectrum  $\pm$  SEM acquired from a sBCC lesion prior to therapy and the resulting nonlinear fit using the scaled MC algorithm. This fit accounts for absorption from oxy- and deoxyhemoglobin, melanin, water, two scattering terms and room light contamination. It returned a blood oxygen concentration of 92%. The figure shows every fifth data point for clarity. Data points between 625 and 640 nm have been excluded due to treatment laser spectral contamination.

defining a geometrical space, which was then collapsed through N-dimensional topology to find the function minimum and best-fit vector.

Prior to fitting, test reflectance spectra were normalized at 632.8 nm, and every ten data points from the spectrometer were binned. This provided a spectrum with the 3 nm resolution governed by the spectrometer optics. Additionally, the standard error (SEM) was evaluated for the ten data points within each bin and provided a measure of spectral error.

A representative reflectance fit using this algorithm is shown in Figure 2.9, determining a blood oxygen saturation of 92% for this lesion. Data between 625 and 640 are excluded in the fits due to the narrow-band contamination from the laser source, visible in Figure 2.6.

### **2.3.2.3 Sampling depth**

MC simulations were also run using the probe geometry outlined above in order to assess the sampling depth of the reflectance data. The results of these simulations are shown in Figure 2.10. The first simulation assumed physiologically realistic lower-bound scattering and absorption parameters of  $\mu'_s = 1 \text{ mm}^{-1}$  and  $\mu_a = 0.1 \text{ mm}^{-1}$ . Similarly, the second simulation assumed

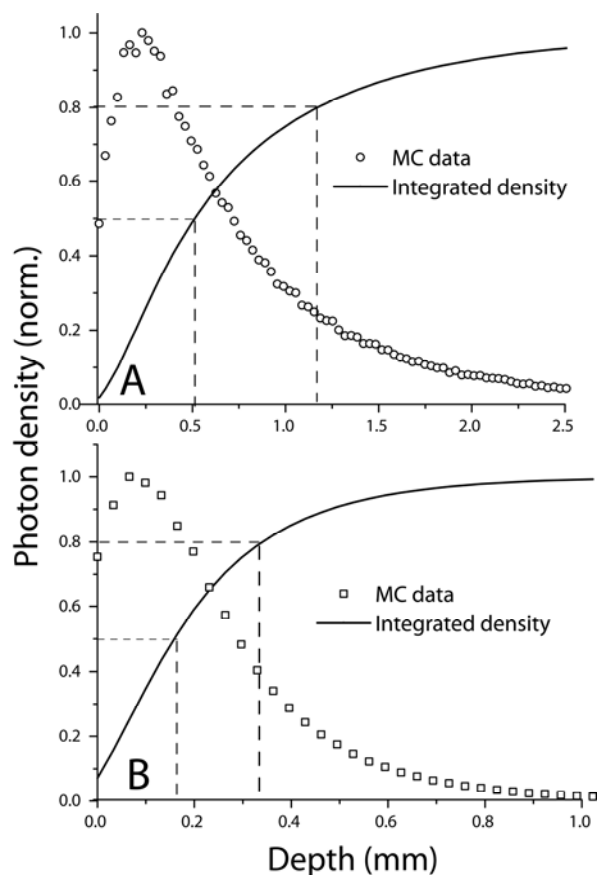


Figure 2.10: MC-modeled photon density as a function of tissue depth for recovered photons during reflectance spectroscopy. The simulations used scattering and absorption parameters of (A)  $\mu'_s = 1 \text{ mm}^{-1}$  and  $\mu_a = 0.1 \text{ mm}^{-1}$  and (B)  $\mu'_s = 1.5 \text{ mm}^{-1}$  and  $\mu_a = 0.5 \text{ mm}^{-1}$ . MC data is shown using open symbols and solid lines represent the integrated density of photons up to the specified depth. Dashed lines locate depths up to which 50 and 80 percent of the photons travel. The simulations indicate that (A) 50 percent of the detected photons sampled a depth up to 0.5 mm and 80 percent sampled up to 1.2 mm in the first case and (B) 50 percent of the detected photons sampled a depth up to 0.19 mm, and 80 percent sampled up to 0.33 mm in the second case.



higher scattering and absorption parameters of  $\mu'_s = 1.5 \text{ mm}^{-1}$  and  $\mu_a = 0.5 \text{ mm}^{-1}$ .

The first simulation indicated that 50 percent of the detected photons sampled a depth up to 0.5 mm and 80 percent sampled up to 1.2 mm. The second simulations similarly indicated that 50 percent of the detected photons sampled a depth up to 0.19 mm, and 80 percent sampled up to 0.33 mm.

### 2.3.3 Fluorescence

In the data shown in this chapter and in Chapter 3, fluorescence was generated by the treatment source at 632.8 nm. As illustrated in Figure 2.11, this treatment wavelength nearly coincides with the fluorescence emission maximum of PpIX at 635 nm. Light entering the detection chain from the treatment source was blocked with a long-pass filter and fluorescence between 665 and 775 nm was monitored, including PpIX's secondary fluorescence peak at 705 nm, autofluorescence, and photoproduct I.

Prior to spectral analysis, fluorescence spectra were corrected for the influence of the instrumentation. Dark signals measured prior to treatment were subtracted from the raw data, and the spectrum was divided by a channel-specific sensitivity function, which was generated by measuring the instrument response to a NIST-traceable calibration lamp (LS-1-CAL, Ocean Optics, Dunedin, FL). In order to obtain intrinsic fluorescence, however, spectra were

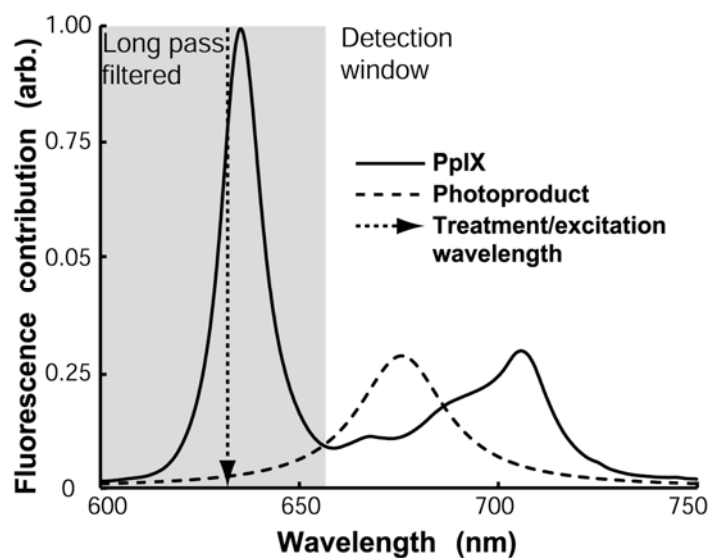


Figure 2.11: Normalized fluorescence emission curves for PpIX and photoproduct I. These curves illustrate the relative location of the 632.8 nm treatment beam to PpIX and photoproduct I fluorescence and the detection window in which fluorescence was monitored with this instrument.

corrected for possible distortions introduced by tissue absorption and scattering. This was accomplished using an empirical correction technique explored by Wu *et al.* (1993), in which the measured spectrum was divided by the white-light reflectance spectrum measured in the same geometry and in the same spectral window. Though this method is easy to employ and provides a more rigorously corrected fluorescence spectrum, in practice we found that reflectance spectra between 655 and 775 nm were relatively flat, consistent throughout treatment, and subsequent corrections did not significantly affect data analysis. This correction was therefore omitted during the real-time data assessment of fluorescence and was only utilized for the more rigorous post-measurement data analysis. Real-time corrections were instead made using representative reflectance spectra averaged from several pre-clinical experiments. In order to accurately analyze fluorescence spectra in real time, LabVIEW called a SVD spectral fitting routine implemented in Matlab (Mathworks, Natick, MA). SVD is superior to the more familiar least squares (LS) minimization in situations where the basis spectra being fit are non-orthogonal. It overcomes the shortcomings of LS by preventing the use of large negative fits, common in LS fitting. Details of the algorithm can be found in Numerical Recipes in C (Press *et al.*, 1992). The fluorescence basis spectra used in these analyses included those of PpIX, a fluorescent photoproduct of PpIX (photoproduct I), tissue autofluorescence, and fiber autofluorescence, all of which are NIST-traceably

calibrated. The tissue autofluorescence basis spectrum used in the fitting is the normalized average of 18 spectra excited by 632.8 nm light measured from the forearms of two volunteers. The fiber autofluorescence basis spectrum is similarly the normalized average of 18 spectra measured by directing 632.8 nm light through the treatment channel of the instrument. The PpIX and photoproduct I basis spectra were obtained in previous work by Finlay *et al.* (2001). A 61-term Fourier series was also included in the spectral basis library to identify unaccounted-for contributions in the measured spectra and any possible autofluorescence changes induced by the therapy. A penalizing weight was given to this series, however, so that fitting preference is given to known spectra. Additionally, by keeping the number of Fourier terms small, only broad fluorescence peaks are detected and noise is not fit. The total spectrum  $F(\lambda)$  is therefore represented by

$$F(\lambda) = \sum_{i=1}^4 A_i w_i f_i(\lambda) + w_2 \times \left[ B_0 + \sum_{k=1}^{61} e^{-\frac{k}{20}} \left\{ B_k \sin\left(\frac{\pi k(\lambda - \lambda_i)}{\lambda_f - \lambda_i}\right) + C_k \cos\left(\frac{\pi k(\lambda - \lambda_i)}{\lambda_f - \lambda_i}\right) \right\} \right] \quad [2.2]$$

where  $w_1$  and  $w_2$  are the user-defined weights of the basis spectra,  $\lambda_i$  and  $\lambda_f$  are the initial and final wavelengths, respectively,  $f_i(\lambda)$  are the spectra from known fluorophores, and  $A_i$ ,  $B_k$ , and  $C_k$  are the spectral amplitudes of the returned fit.

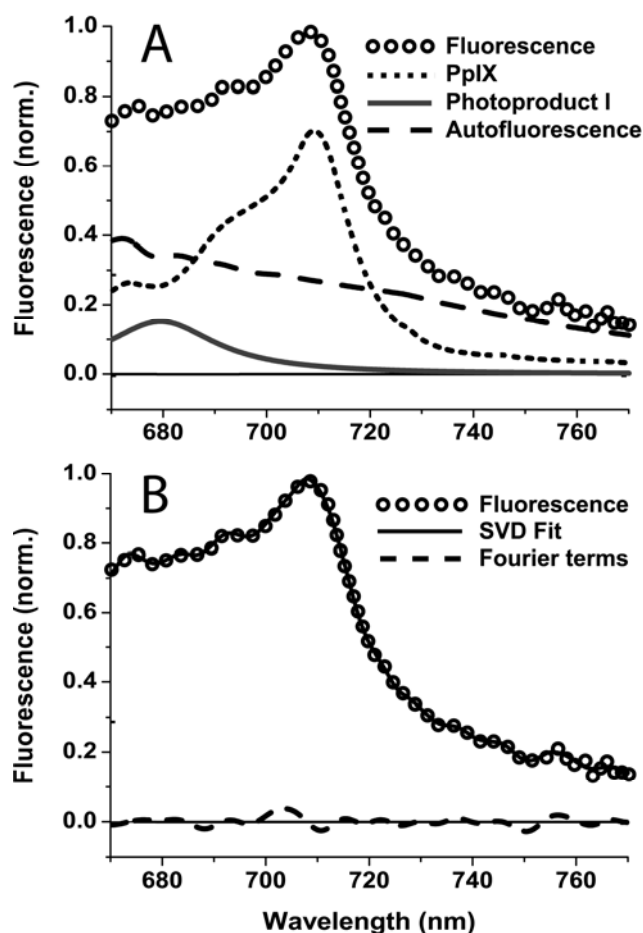


Figure 2.12: Fluorescence spectrum measured from a sBCC lesion after  $3 \text{ J cm}^{-2}$  treatment and decomposed with SVD. (A) The SVD fit shows appreciable contribution to the signal from PpIX, tissue and fiber autofluorescence, and photoproduct I. For clarity, the autofluorescence contribution shown is the sum of the tissue and fiber autofluorescence. Several data points have been removed for clarity. (B) A good fit to the data is achieved with known basis spectra and only a minimal contribution from the 61-term Fourier series.

A representative fluorescence spectrum obtained from an ALA-sensitized sBCC lesion and analyzed with SVD is shown in Figure 2.12. SVD analysis performed on each measured spectrum during the course of a treatment reported the relative amplitudes of the fluorophores represented in the fit. The PpIX and photoproduct I contributions to the fluorescence from the lesion field are monitored throughout PDT, as shown in representative bleaching curves from a lesion treated at  $150 \text{ mW cm}^{-2}$  (Figure 2.13).

MC simulations were also run in order to assess the depth from which detected fluorescence photons originated. In order to model the fluorescence for specific scattering and absorption coefficients, two sets of absorption data had to be generated. One simulation was run in the adjoint sense, as described above, and another simulation was run in the forward direction, with the photons traced from the true source. The absorption data from the simulation in the forward direction generated a distribution of intrinsic fluorescence. Similarly, the absorption data from the simulation run in the adjoint direction represents the probability that a photon generated in that location would be detected, called the importance (Crilly *et al.*, 1997). The overlap integral of these two distributions therefore represents the distribution of detected fluorescence photons. In the simulations presented here, absorption and importance distributions were binned

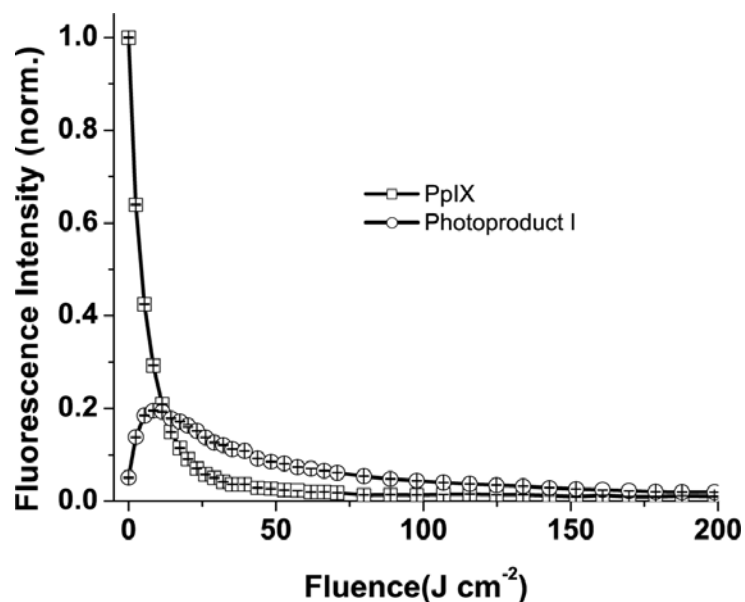


Figure 2.13: PpIX and photoproduct I fluorescence amplitudes detected in the lesion field throughout a single PDT treatment of sBCC of  $200 \text{ J cm}^{-2}$  delivered at  $150 \text{ mW cm}^{-2}$ . The PpIX and photoproduct I amplitudes are normalized to the initial PpIX fluorescence intensity detected from the lesion. Error bars represent uncertainties in the SVD fit.

every 0.1 mm. The relative detected fluorescence distribution was subsequently calculated by multiplying the two distributions.

As before, the first simulations assumed physiologically realistic lower-bound scattering and absorption parameters of  $\mu'_s = 1 \text{ mm}^{-1}$  and  $\mu_a = 0.1 \text{ mm}^{-1}$ , and the second assumed upper-bound absorption parameters of  $\mu'_s = 1.5 \text{ mm}^{-1}$  and  $\mu_a = 0.5 \text{ mm}^{-1}$ . The resulting detected fluorescence distribution and on-axis fluorescence depth results are shown in Figure 2.14. The first simulation indicated that 50 percent of the detected fluorescence photons originated between the surface and 0.7 mm, and 80 percent up to 1.3 mm. The second simulations similarly indicated that 50 percent of the detected fluorescence photons originated between the surface and 0.3 mm, and 80 percent sampled up to 0.6 mm.

## 2.4 Discussion

This instrument has demonstrated the ability to non-invasively measure reflectance and fluorescence spectra during ALA-PDT of human basal cell carcinoma. By keeping the optical probe simple and consistent with current clinical protocol, spectroscopic monitoring was easily incorporated into a clinical trial. To date this trial has accrued 29 patients, representing 31 sBCC



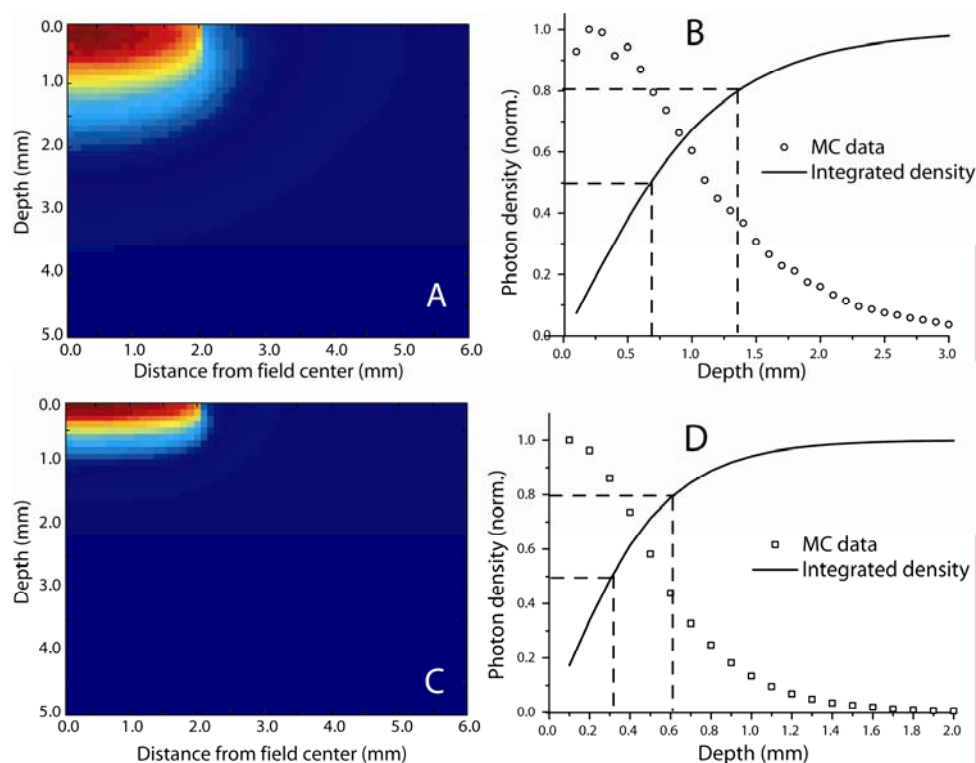


Figure 2.14: MC-modeled detected fluorescence as a function of tissue depth for photons recovered during fluorescence spectroscopy. The simulations used scattering and absorption parameters of (A,B)  $\mu'_s = 1 \text{ mm}^{-1}$  and  $\mu_a = 0.1 \text{ mm}^{-1}$  and (C,D)  $\mu'_s = 1.5 \text{ mm}^{-1}$  and  $\mu_a = 0.5 \text{ mm}^{-1}$ . A and C show resulting fluorescence photon distribution maps. B and D show fluorescence photon density along the center axis. MC data is shown using open symbols and solid lines represent the integrated density of photons up to the specified depth. Dashed lines locate depths up to which 50 and 80 percent of the fluorescence was generated. (B) Indicates that 50 percent of the detected fluorescence photons originated between the surface and 0.7 mm, and 80 percent up to 1.3 mm. The second simulations similarly indicated that 50 percent of the detected fluorescence photons originated between the surface and 0.3 mm, and 80 percent sampled up to 0.6 mm.

lesions. As is discussed in Chapter 3, monitoring PpIX photobleaching and blood oxygen saturation during therapy is guiding the fluence and fluence rate protocols for an anticipated low-irradiance clinical trial aimed at improving patient comfort during PDT while maintaining high treatment efficacy and short treatment duration. PDT delivered at high fluence rates, such as the current standard of  $150 \text{ mW cm}^{-2}$ , may deplete tissue oxygen levels and is painful, often necessitating conscious sedation for patients with large treatment fields or multiple lesions.

Fluorescence spectra acquired with this instrument are generated by the PDT treatment beam. Unlike the more common implementation in which shorter wavelengths are used to excite photosensitizer fluorescence, this approach has the advantages that the fluorescence necessarily originates in the same tissue volume that is being treated, and there is no treatment interruption during fluorescence acquisition. Only brief and infrequent interruptions allow reflectance spectroscopy. Additionally, using the treatment beam for fluorescence spectroscopy ensures that no unaccounted for PDT is delivered during spectroscopy.

As seen in Figure 2.13, the fluorescence spectra from sBCC lesions contained significant contributions from photoproduct I, which at peak levels reached

approximately 20% of the initial PpIX contribution. The dynamics of this photoproduct include a slow photobleaching during PDT, suggesting a possible role as a sensitizer. It is also notable that several of the fluorescence spectra which make up the basis set used in the SVD fitting of the sBCC data were derived from measurements made on the skin of ALA-sensitized rats (Finlay *et al.*, 2001). As seen in Figure 2.12, these basis spectra provide excellent fits to the measured spectra from human skin.

Further analysis is required to determine the exact treatment volume and to extract quantitative information on hemoglobin concentrations, though the determination of blood oxygen saturation appears to be robust. The contamination to the sBCC reflectance spectrum at 632.8 nm resulted primarily from laser light scattered from other lesions undergoing simultaneous treatment. There is a contribution to this peak from switch cross-talk, however, which cannot be eliminated by blocking the contribution from stray treatment light. Therefore, this contamination to the reflectance is best eliminated by deleting the data in a narrow range around 632.8 nm prior to reflectance analysis. Similarly, additional features show up in some reflectance spectra, which originate from fluorescent lights in the clinical theater. This contribution is minimized by dimming room lights and by using a bright white-light source

allowing short spectroscopic integrations. Any remaining room-light signature is removed in the fitting process, outlined above.

The instrument, along with the established and developing analysis techniques, provides a platform that will support improved treatment planning using lesion-specific optical properties to guide PDT dose prescription. This instrumentation demonstrates the potential for simultaneously monitoring sensitizer photobleaching, photoproduct kinetics, blood oxygenation, and changes to tissue optical properties non-invasively during PDT, which allows rigorous exploration of irradiance dependent photobleaching during clinical application of ALA-PDT of sBCC lesions, other cutaneous disease, and other spectroscopically-accessible tissues. Simple and automated instrumentation coupled with the ability to accurately analyze dose metrics throughout PDT suggests that it may be possible to build a feed-back driven system capable of optimizing fluence and fluence rate delivery, informed in real time by changes to sensitizer concentration and tissue optical properties.

## 2.5 References

- Adamson A.W. (1979). *Molecular Spectroscopy and Photochemistry*, A Textbook of Physical Chemistry, pages 789-848. Academic Press, Inc., New York.
- Bays R., Wagnieres G., Robert D., Braichotte D., Savary J.F., Monnier P., and vandenBergh H. (1997). Light dosimetry for photodynamic therapy in the esophagus. *Lasers Surg. Med.* **20**: 290-303.
- Boere I., de Bruijn R., Robinson D., van den Boogert J., Sterenborg H., de Bruin R., Tilanus H.W. (2002). Photodynamic therapy of the rat esophagus: Correlation between photobleaching and epithelial ablation. *Cancer Epidemiol. Biomarkers Prev.* **11**: 1184S.
- Boere I.A., Robinson D.J., de Bruijn H.S., van den Boogert J., Tilanus H.W., Sterenborg H.J.C.M., and de Bruin R.W.F. (2003). Monitoring *in Situ* dosimetry and protoporphyrin IX fluorescence photobleaching in the normal rat esophagus during 5-aminolevulinic acid photodynamic therapy. *Photochem. Photobiol.* **78**: 271-277.
- Cerniglia G.J., Wilson D.F., Pawlowski M., Vinogradov S., and Biaglow J. (1997). Intravascular oxygen distribution in subcutaneous 9L tumors and radiation sensitivity. *J. Appl. Physiol.* **82**: 1939-1945.
- Crilly R.J., Cheong W.F., Wilson B., and Spears J.R. (1997). Forward-adjoint fluorescence model: Monte Carlo integration and experimental validation. *Appl. Opt.* **36**: 6513-6519.

- Finlay J.C. (2003). Reflectance and Fluorescence Spectroscopies in Photodynamic Therapy. PhD Thesis. University of Rochester, New York.
- Finlay J.C., Conover D.L., Hull E.L., and Foster T.H. (2001). Porphyrin bleaching and PDT-induced spectral changes are irradiance dependent in ALA-sensitized normal rat skin *in vivo*. *Photochem. Photobiol.* **73**: 54-63.
- Finlay J.C., and Foster T.H. (2004). Hemoglobin oxygen saturations in phantoms and *in vivo* from measurements of steady-state diffuse reflectance at a single, short source-detector separation. *Med. Phys.* **31**: 1949-1959.
- Foster T.H., and Gao L. (1992). Dosimetry in photodynamic therapy - oxygen and the critical importance of capillary density. *Rad. Res.* **130**: 379-383.
- Foster T.H., Murant R.S., Bryant R.G., Knox R.S., Gibson S.L., and Hilf R. (1991). Oxygen-consumption and diffusion effects in photodynamic therapy. *Rad. Res.* **126**: 296-303.
- Georgakoudi I., and Foster T.H. (1998). Singlet oxygen- versus nonsinglet oxygen-mediated mechanisms of sensitizer photobleaching and their effects on photodynamic dosimetry. *Photochem. Photobiol.* **67**: 612-625.
- Henderson B.W., Busch T.M., Vaughan L.A., Frawley N.P., Babich D., Sosa T.A., Zollo J.D., Dee A.S., Cooper M.T., Bellnier D.A., Greco W.R., and Oseroff A.R. (2000). Photofrin photodynamic therapy can significantly deplete or preserve oxygenation in human basal cell carcinomas during treatment, depending on fluence rate. *Cancer Res.* **60**: 525-529.
- Hull E.L., Conover D.L., and Foster T.H. (1999). Carbogen-induced changes in rat mammary tumour oxygenation reported by near infrared spectroscopy. *Br. J. Cancer.* **79**: 1709-1716.

- Jacques S.L. (1992). Optical Methods for Tumor Treatment and Detection: simple optical theory for light dosimetry during PDT. *J. Opt. Soc. Am. A Opt. Image Sci. Vis.* **1645**: 155-165.
- Kienle A., and Patterson M.S. (1996). Determination of the optical properties of turbid media from a single Monte Carlo simulation. *Phys. Med. Biol.* **41**: 2221-2227.
- Langmack K., Mehta R., Twyman P., and Norris P. (2001). Topical photodynamic therapy at low fluence rates - theory and practice. *J. Photochem. Photobiol. B, Biol.* **60**: 37-43.
- Marijnissen J.P.A., and Star W.M. (2002). Performance of isotropic light dosimetry probes based on scattering bulbs in turbid media. *Phys. Med. Biol.* **47**: 2049-2058.
- Murrer L.H.P., Marijnissen J.P.A., Baas P., VanZandwijk N., and Star W.M. (1997). Applicator for light delivery and *in situ* light dosimetry during endobronchial photodynamic therapy: First measurements in humans. *Lasers Med. Sci.* **12**: 253-259.
- Nichols M.G., Hull E.L., and Foster T.H. (1997). Design and testing of a white-light, steady-state diffuse reflectance spectrometer for determination of optical properties of highly scattering systems. *Appl. Opt.* **36**: 93-104.
- Niedre M.J., Secord A.J., Patterson M.S., and Wilson B.C. (2003). *In vitro* tests of the validity of singlet oxygen luminescence measurements as a dose metric in photodynamic therapy. *Cancer Res.* **63**: 7986-7994.
- Nunn A., Linder K., and Strauss H.W. (1995). Nitroimidazoles and Imaging Hypoxia. *Eur. J. Nucl. Med.* **22**: 265-280.

- Peng Q., Warloe T., Berg K., Moan J., Kongshaug M., Giercksky K.E., and Nesland J.M. (1997). 5-aminolevulinic acid-based photodynamic therapy - Clinical research and future challenges. *Cancer*. **79**: 2282-2308.
- Press W.H., Vetterling W.T., Teukolsky S.A., and Flannery B.P. (1992). Modeling of Data. In Numerical Recipes in C, pages 656-706. Cambridge University Press, New York.
- Robinson D.J., de Bruijn, H.S., van der Veen N., Stringer M.R., Brown S.B., and Star W.M. (1998). Fluorescence photobleaching of ALA-induced protoporphyrin IX during photodynamic therapy of normal hairless mouse skin: The effect of light dose and irradiance and the resulting biological effect. *Photochem. Photobiol.* **67**: 140-149.
- Robinson D.J., de Bruijn H.S., van der Veen N., Stringer M.R., Brown S.B., and Star W.M. (1999). Protoporphyrin IX fluorescence photobleaching during ALA-mediated photodynamic therapy of UVB-induced tumors in hairless mouse skin. *Photochem. Photobiol.* **69**: 61-70.
- Star W.M., van Veen A.J., Robinson D.J., Munte K., de Haas E.R.M., and Sterenborg H.J.C.M. (2006). Topical 5-aminolaevulinic acid mediated photodynamic therapy of superficial basal cell carcinoma using two light fractions with a two-hour interval: Long-term follow-up. *Acta Derm. Venereol.* **86**: 412-417.
- Thompson M.S., Johansson A., Johansson T., Andersson-Engels S., Svanberg S., Bendsoe N., Svanberg K. (2005). Clinical system for interstitial photodynamic therapy with combined on-line dosimetry measurements. *Appl. Opt.* **44**: 4023-4031.



- van Veen R.L.P., Aalders M.C.G., Pasma K.L., Siersema P.D., Haringsma J., van de Vrie W., Gabeler E.E.E., Robinson D.J., and Sterenborg H.J.C.M. (2002). *In situ* light dosimetry during photodynamic therapy of Barrett's esophagus with 5-aminolevulinic acid. *Lasers Surg. Med.* **31**: 299-304.
- vanStaveren H.J., Keijzer M., Keesmaat T., Jansen H., Kirkel W.J., Beek J.F., and Star W.M. (1996). Integrating sphere effect in whole-bladder-wall photodynamic therapy. Fluence multiplication, optical penetration and light distribution with an eccentric source for human bladder optical properties. *Phys. Med. Biol.* **41**: 579-590.
- Vinogradov S.A., Lo L.W., Jenkins W.T., Evans S.M., Koch C., and Wilson D.F. (1996). Noninvasive imaging of the distribution in oxygen in tissue *in vivo* using near-infrared phosphors. *Biophys. J.* **70**: 1609-1617.
- Wang L.H., Jacques S.L., and Zheng L.Q. (1995). Mcml - Monte-Carlo Modeling of Light Transport in Multilayered Tissues. *Comput. Methods and Programs Biomed.* **47**: 131-146.
- Wu J., Feld M.S., and Rava R.P. (1993). Analytical Model for Extracting Intrinsic Fluorescence in Turbid Media. *Appl. Opt.* **32**: 3585-3595.

## Chapter 3

### **Clinical assessment of irradiance-dependent photobleaching and pain in $\delta$ -aminolevulinic acid-photodynamic therapy of superficial basal cell carcinoma**

#### **3.1 Introduction**

As noted in Chapter 2, topically-administered aminolevulinic acid-photodynamic therapy (ALA-PDT) is a therapy in which the prodrug ALA is converted into the photosensitizer protoporphyrin IX (PpIX) in the skin *via* the heme cycle. This therapy is enjoying clinical acceptance for the treatment of a variety of conditions, particularly non-melanoma skin cancers such as superficial basal cell carcinoma (sBCC), largely resulting from tumor selectivity (Wennberg *et al.*, 2000), favorable cosmetic outcomes compared to surgical

extirpation and cryogenic therapy (Wang *et al.*, 2001), high complete response rates (Zeitouni *et al.*, 2003), and easy delivery (Morton *et al.*, 2002).

Acute pain associated with ALA-PDT is the therapy's primary side-effect, which can last for several hours (Holmes *et al.*, 2004), and has been noted to depend on light source, irradiance (van Oosten *et al.*, 2006), lesion location (Grapengiesser *et al.*, 2002), and number and size of treatment locations (Grapengiesser *et al.*, 2002; Sandberg *et al.*, 2006). Pain management is therefore a significant hurdle to the clinical acceptance of this therapy, making it important to find treatment protocols which equal or exceed current efficacies while limiting patient discomfort and time in the clinic.

The study presented in this chapter investigated the pain during ALA-PDT at several different irradiances. Under current general protocol at Roswell Park Cancer Institute (RPCI) patients are treated using  $200 \text{ J cm}^{-2}$  of 632.8 nm light at  $150 \text{ mW cm}^{-2}$  and predominantly experience a stinging and burning sensation, which requires pain intervention and which is consistent with high-irradiance ALA-PDT-induced pain described by others (Algermissen *et al.*, 2003; Ericson *et al.*, 2004; Fritsch *et al.*, 1997; Grapengiesser *et al.*, 2002; Holmes *et al.*, 2004; Radakovic-Fijan *et al.*, 2005; Sandberg *et al.*, 2006; van Oosten *et al.*, 2006). For single small-area sBCC therapy, pain is often addressed with a local 1% xylocaine injection, though patients with multiple treatment locations or large

area treatments often require conscious sedation. This is a significant obstacle to the general clinical acceptability of ALA-PDT, particularly with patients who are among the best candidates for PDT, such as those with nevoid basal cell carcinoma syndrome. These patients may develop tens or even hundreds of sBCC lesions per year and often require multiple simultaneous treatments and large treatment fields. Some investigators have noticed less pain associated with ALA-PDT delivered at lower fluence rates (Algermissen *et al.*, 2003; van Oosten *et al.*, 2006) and excitation wavelengths that do not coincide with PpIX absorption peaks (Fritsch *et al.*, 1997), which is consistent with anecdotal evidence at RPCI that pain reduces with lower irradiance.

Current RPCI protocol yields a high clinical response (CCR) of > 93% for sBCC (Zeitouni *et al.*, 2003). However, since treatment duration for a constant fluence is inversely proportional to irradiance, lowering irradiance may cause an unacceptable increase in treatment duration beyond the 22 minutes required to deliver  $200 \text{ J cm}^{-2}$  at  $150 \text{ mW cm}^{-2}$ . For this trial we therefore adopted a two-irradiance protocol during which we assessed treatment progression using the surrogate dose metric of PpIX fluorescence photobleaching. PDT was initially delivered at low-irradiance until 90% of the PpIX was photobleached; the remainder of the fluence was then delivered at  $150 \text{ mW cm}^{-2}$ . Pain was monitored during the entire course of therapy every 5 minutes using a visual

analog scale (VAS) score between 0 and 10 in order to assess any irradiance-dependent changes in pain experienced during PDT.

This trial established the irradiance-dependence of patient tolerability to ALA-PDT of sBCC and a pain-threshold irradiance, below which patients did not experience significant pain or require anesthetic. The irradiance-dependence of PpIX fluorescence photobleaching was also used to determine an optimal irradiance that maximized treatment efficiency.

## **3.2 Materials and methods**

### **3.2.1 Patients**

Lesion selection criteria included sBCC measuring at least 5 mm but not greater than 20 mm in diameter. No patient contributed more than 2 lesions to the study, and no effort was made to select patients for skin tone, lesion pigmentation, lesion location or other criteria. In accordance with the United States Food and Drug Administration guidelines, patients were informed of the investigational nature of this study and signed a consent form. The Office of Research Subject Protection & Scientific Integrity at RPCI in Buffalo, NY USA approved this study. SBCC was confirmed for these lesions by histological biopsy two weeks prior to treatment, allowing the site to heal prior to therapy.

### **3.2.2 ALA administration**

ALA (DUSA Pharmaceuticals, Vahalla, NY) was freshly prepared at a 20% (w/w) concentration in an oil-in-water cream (Moisturel, Westwood Pharmaceuticals). The ALA was covered by an occlusive bandage and opaque material to prevent photo-activation prior to therapy. Following application, the ALA remained on the skin for  $4 \text{ h} \pm 15\%$ . The area was cleaned with normal saline prior to irradiation to remove any residual cream. After the 4 h incubation period, the presence of PpIX was confirmed visually using fluorescence excited from a 405 nm LED flashlight. Visual inspection revealed lesion-to-lesion variation in initial PpIX fluorescence, which was subsequently confirmed with fluorescence spectroscopy measurements made during the therapy.

### **3.2.3 Irradiation**

Six irradiances were used in this study: 10, 20, 40, 50, 60, and  $150 \text{ mW cm}^{-2}$ . PDT treatment was delivered in two parts: the initial therapy was delivered at low irradiance until the fluorescence contribution from PpIX in the lesion bleached by 90% of its initial value, at which point the treatment was continued at  $150 \text{ mW cm}^{-2}$  until  $200 \text{ J cm}^{-2}$  was delivered. This protocol allowed treatment to be completed in a reasonable timeframe.

Similarly to Chapter 2, MC simulations were run in order to assess likely PDT treatment depths under normal conditions. Simulations were run at lower- and upper-bound physiological scattering and absorption parameters and modeled the tissue as a uniform semi-infinite slab. The lower-bound simulation used  $\mu'_s = 1 \text{ mm}^{-1}$  and  $\mu_a = 0.1 \text{ mm}^{-1}$ , and the upper-bound simulation used  $\mu'_s = 1.5 \text{ mm}^{-1}$  and  $\mu_a = 0.5 \text{ mm}^{-1}$ . The resulting fluence distributions and on-axis results are shown in Figure 3.1. The absorption and scattering values used for the lower-bound simulation are likely representative for the skin types in this study when treated with 632.8 nm light. This simulation indicated 50 percent of the fluence was delivered between the surface and depth of 1.3 mm and 80 percent by 3.0 mm. Similarly, the upper-bound simulations indicated 50 percent of the fluence was delivered between the surface and depth of 0.5 mm and 80 percent by 1.1 mm.

### **3.2.4 Pain assessment**

Pain experienced as a result of the therapy was determined with a VAS score, wherein a score of 0 represents no pain, 10 represents unbearable pain, and 4 represents moderate pain, requiring anesthetic;  $\text{VAS} \leq 3$  did not require intervention. Each patient was questioned about pain every 5 minutes and encouraged to notify the staff about changes in pain between these intervals. A

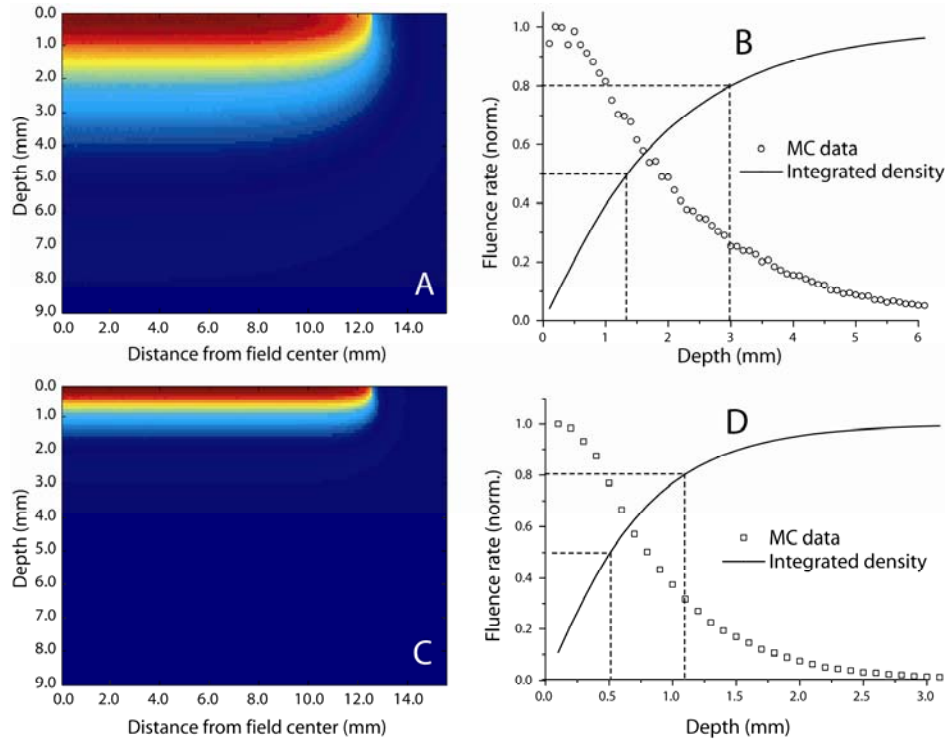


Figure 3.1: MC-modeled fluence distribution of PDT therapy. The simulations used the probe geometry specified in Chapter 2 and tissue scattering and absorption parameters of (A,B)  $\mu'_s = 1 \text{ mm}^{-1}$  and  $\mu_a = 0.1 \text{ mm}^{-1}$ , and (C,D)  $\mu'_s = 1.5 \text{ mm}^{-1}$  and  $\mu_a = 0.5 \text{ mm}^{-1}$ . A and C show resulting fluence distribution maps. B and D show the relative fluence along the treatment field's center axis. MC data use open symbols and solid lines represent the integrated fluence up to that depth. Dashed lines locate depths to which 50 and 80 percent of the fluence was deposited. In the clinical experiments it is likely that (B) 50 percent of the fluence was delivered between the surface and 1.3 mm, and 80 percent was deposited up to 3.0 mm. Highly pigmented perfused regions may have had (D) 50 percent of the fluence delivered between the surface and 0.5 mm, and 80 percent deposited up to 1.1 mm.



pain score of 4 or above was treated by injections around the treatment site with 1% xylocaine. A stopping rule was employed such that if two patients had VAS scores of 4 or greater at a given irradiance then therapy at a higher initial irradiance would not be performed. Instead, an irradiance midway between that irradiance and the previous irradiance would be evaluated. After the irradiance was increased to  $150 \text{ mW cm}^{-2}$ , pain was assessed immediately and then every 5 minutes as before. Pain was not assessed during the continuous  $150 \text{ mW cm}^{-2}$  treatment as it had previously been established that treatment at this irradiance generally required pain intervention and had a VAS score above 5. Pain was mediated in this group by conscious sedation or 1% xylocaine injection prior to therapy, repeated as necessary, and by fan cooling.

### **3.2.5 Clinical follow up**

Lesions were evaluated clinically at 3 and 6 months, and then approximately every 6 months. Complete clinical responses were determined at  $\geq 6$  months.

### **3.2.6 Instrumentation**

PpIX photobleaching, mediated predominantly by the same photochemistry as dose deposition, was explored as a surrogate dose metric and as a way to assess efficiency without explicitly monitoring treatment parameters in the treatment

volume. Photobleaching at each irradiance was measured using instrumentation and data reduction described in Chapter 2.

During PDT, fluorescence and reflectance data in both regions were acquired at intervals of between 0.3 and 3 J cm<sup>-2</sup> and between 2 and 18 J cm<sup>-2</sup>, respectively, depending on which irradiance was used. Spectra were saved to file and analyzed in real time using an SVD analysis Matlab (The MathWorks, Natick, MA USA) routine developed by our lab and called by our LabVIEW system control software. After 90% photobleaching was detected in the lesion, the instrument automatically switched to 150 mW cm<sup>-2</sup> irradiance and delivered the remainder of the fluence, which was calculated by the LabVIEW program.

### **3.2.7 Data analysis**

In order to obtain intrinsic tissue fluorescence, spectra were corrected for tissue absorption and scattering. These corrections were made with an empirical technique explored by Wu *et al.* (1993) in which the measured spectrum was divided by the white-light reflectance spectrum measured in the same geometry and in the same spectral window, as described in Chapter 2. The corrected fluorescence spectra were analyzed using a singular-value decomposition (SVD) linear fitting algorithm in a LabVIEW-called Matlab routine, which incorporated NIST-traceable, calibrated fluorescence basis spectra for PpIX, the primary

fluorescent photoproduct of PpIX (photoproduct I), and tissue and fiber autofluorescence. A Fourier series was also included in the spectral basis library to identify unaccounted-for contributions in the measured spectra and any possible autofluorescence changes induced by the therapy (Finlay *et al.*, 2001). In the subsequent post-treatment analysis of the data, the fluence at which 80% of the initial PpIX had bleached ( $D_{80}$ ) was used to determine bleaching efficiency. This point was chosen because bleaching in the perilesion margin field was found experimentally to proceed more slowly than in the monitored lesion field.  $D_{80}$  therefore represented a comparable bleaching metric available in each data set.  $D_{80}$  was determined by linear interpolation of the calculated fluorescence contribution curve for each lesion and margin. Photobleaching and photoproduct data were normalized to the PpIX fluorescence intensity at the start of treatment. Reflectance spectra were fit using a downhill simplex fitting algorithm (Press *et al.*, 1992) based on scaled Monte Carlo simulations (Kienle and Patterson, 1996). This algorithm incorporated the known absorption from oxyhemoglobin, deoxyhemoglobin, and melanin, and the tissue scattering spectrum. Fits to the reflectance spectra reported blood oxygen saturations.

### 3.2.8 Statistics

Fisher's exact test was used to compare the clinical responses from the 10-60 mW cm<sup>-2</sup> irradiances to results of the prior trial at 150 mW cm<sup>-2</sup>.

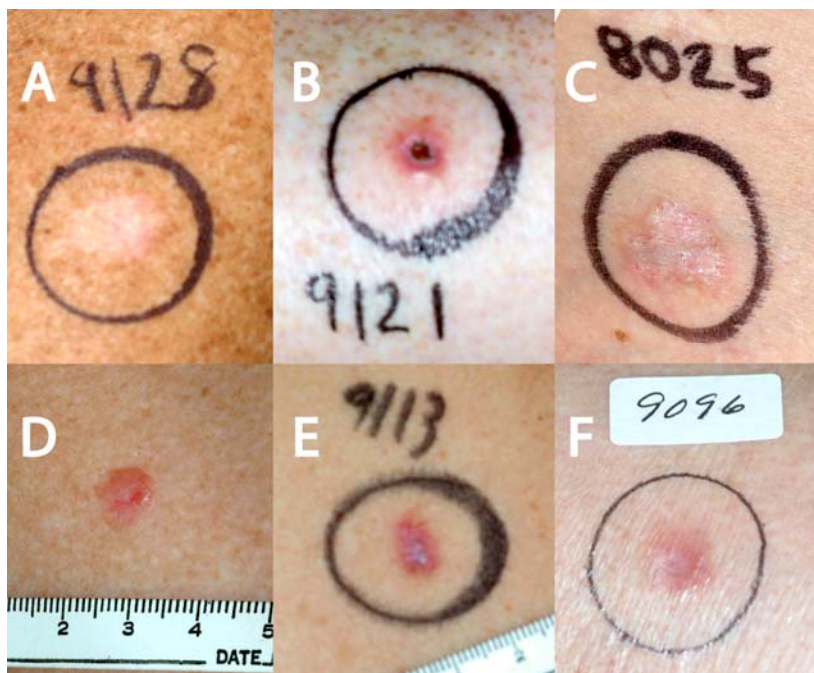


Figure 3.2: Representative sBCC lesions and treatment fields included in this study show significant lesion and perilesion heterogeneity.

### 3.3 Results

#### 3.3.1 Lesions and Patients

This study involved 31 superficial basal cell carcinoma lesions in 29 patients, 13 male and 16 female, including seven lesions at  $150 \text{ mW cm}^{-2}$ , five each at 60, 50, 40, and  $10 \text{ mW cm}^{-2}$ , and four at  $20 \text{ mW cm}^{-2}$ . Lesion locations included face, arm, back, and chest. Photographs of representative lesions are shown in Figure 3.2. One patient included in this study had nevoid basal cell carcinoma syndrome. In two lesions (at 20 and  $40 \text{ mW cm}^{-2}$ ) optical data were not available due to equipment malfunction, but pain scores were evaluated. Additionally, one margin was excluded because of weak PpIX signal strength. Clinical response data  $\geq 6$  months after treatment currently are available for all lesions except those treated at  $50 \text{ mW cm}^{-2}$ .

#### 3.3.2 PpIX Photobleaching

SVD analysis performed on each measured spectrum during the course of a treatment reports the relative amplitudes of the fluorophores represented in the fit. A representative fluorescence spectrum obtained from an ALA-sensitized sBCC lesion treated at  $50 \text{ mW cm}^{-2}$  and analyzed with SVD is shown in Figure 2.11. PpIX and photoproduct I contributions from the same lesion are shown in Figure 2.12.

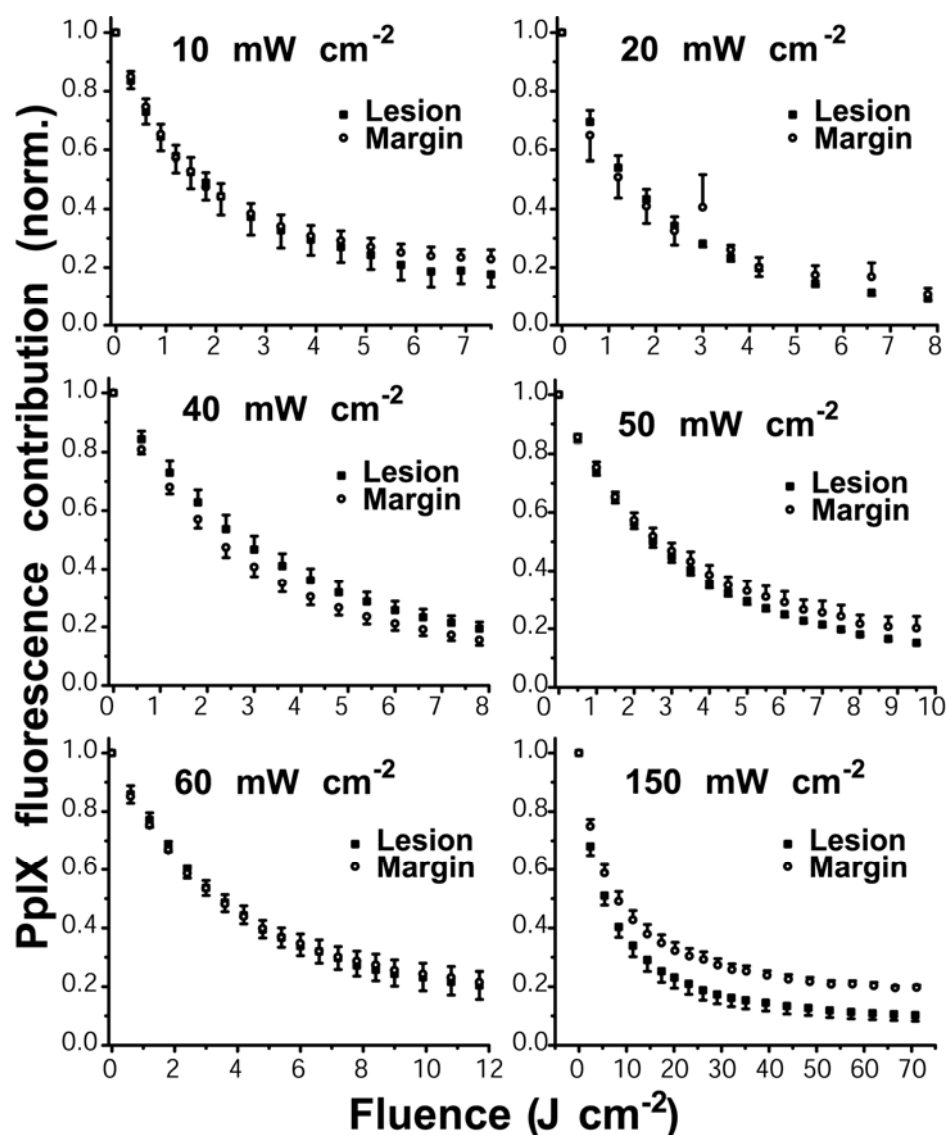


Figure 3.3: Comparison of the averaged  $\pm$  SEM, normalized PpIX contribution to the corrected fluorescence as a function of total fluence between lesion and margin fields for 10, 20, 40, 50, 60, and 150 mW cm<sup>-2</sup> irradiances. PpIX contribution shows fluorescence photobleaching of PpIX during irradiation and suggests comparable bleaching trends between margin and lesion in the lower irradiance groups as well as a clear separation between average bleaching curves at 150 mW cm<sup>-2</sup>.

Bleaching curves paired by lesion and perilesion margin for each of the different irradiance groups (Figure 3.3) demonstrate similar trends for all low-irradiance groups but diverge at  $150 \text{ mW cm}^{-2}$ , where the normal skin bleached more slowly than the lesion. The normal skin PpIX did not fall below 20% of its initial value, consistent with oxygen depletion limiting singlet oxygen production. The reported PpIX fluorescence is the average  $\pm$  SEM for measurements made on each lesion and normalized to the initial PpIX fluorescence amplitude in that lesion. There was no correlation between the initial fluorescence and the subsequent photobleaching curves (data not shown). The variation in normalized PpIX fluorescence excited in the 31 lesions and in the perilesion margins during the initial irradiation interval is summarized in Figure 3.4. The initial photobleaching, determined from the slope between the first two points in the bleaching data, occurred more efficiently at lower irradiance, consistent with the work of other investigators (Ericson *et al.*, 2004; Finlay *et al.*, 2001; Robinson *et al.*, 1998; Robinson *et al.*, 1999). Initial photosensitizer bleaching was rapid, with the lesions in the least efficient group ( $150 \text{ mW cm}^{-2}$ ) bleaching by 80% in  $28.7 \pm 7.1 \text{ J cm}^{-2}$ , representing less than 20% of the  $200 \text{ J cm}^{-2}$  prescribed fluence (Table 3.1). For each irradiance level we see no significant difference between the initial bleaching rates of the lesion and the margin ( $P > 0.17$ ). Single factor ANOVA demonstrated that the initial bleaching rates in lesions and margins for treatments conducted at 10 and

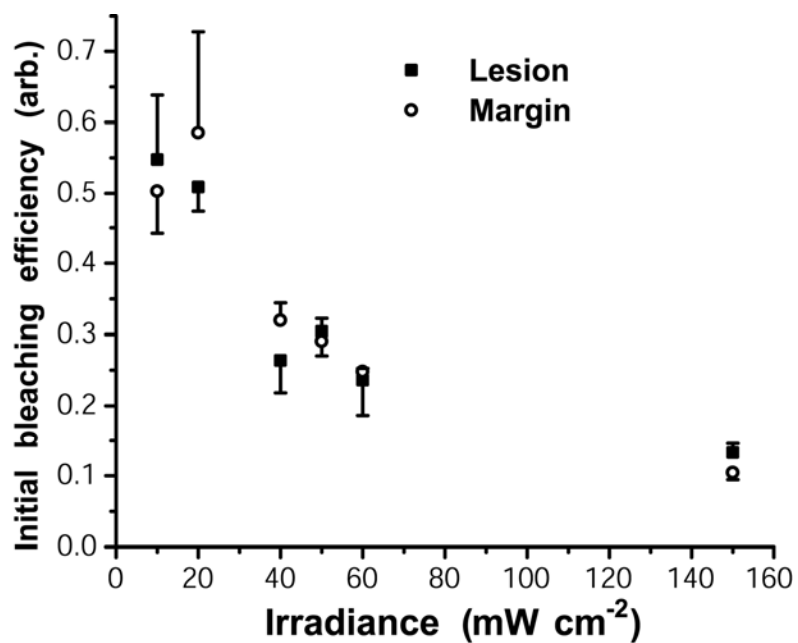


Figure 3.4: Averaged  $\pm$  SEM PpIX initial bleaching rate during ALA-PDT of sBCC at 10, 20, 40, 50, 60, and 150 mW cm<sup>-2</sup>. Bleaching rate was determined by the change in PpIX contribution to fluorescence between the first and second measurements, divided by the fluence increment between those same measurements.



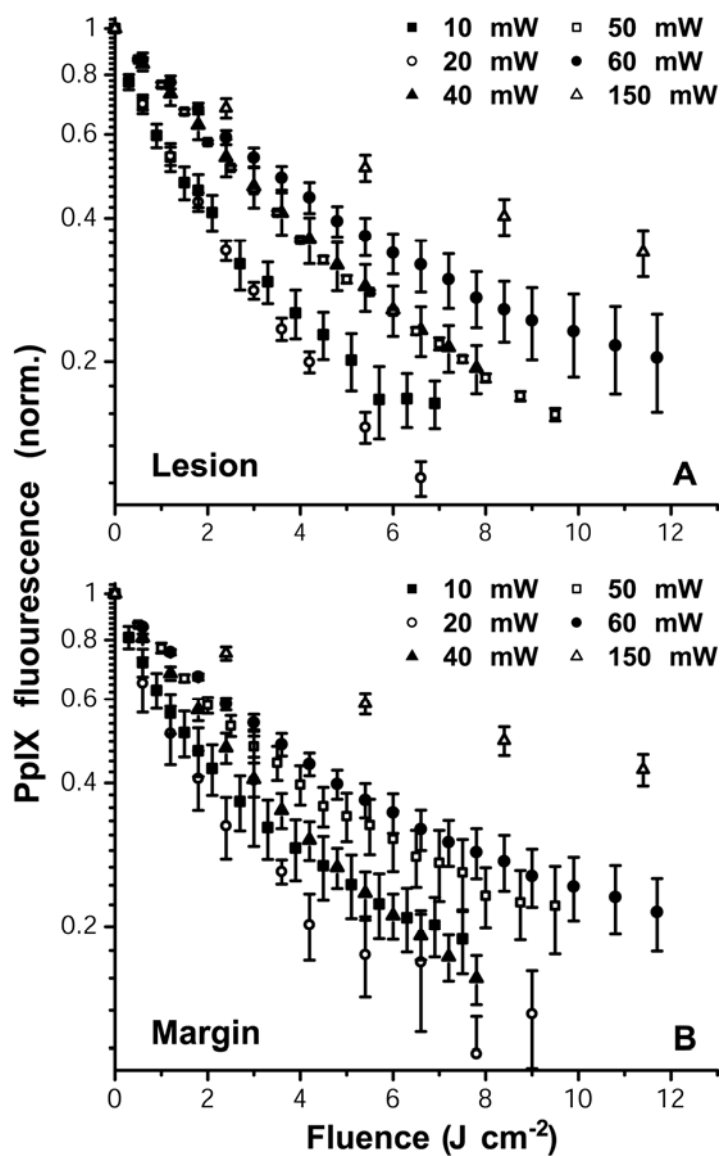


Figure 3.5: Averaged  $\pm$  SEM, normalized PpIX contribution to the corrected fluorescence as a function of delivered fluence from the (A) lesion and (B) margin fields during ALA-PDT of 31 sBCC lesions. The entire treatment field was irradiated with 632.8 nm laser light at six different irradiances: 10, 20, 40, 50, 60, and 150 mW cm<sup>-2</sup>.

20 mW cm<sup>-2</sup> were statistically similar ( $P > 0.7$ ). PDT performed at irradiances of 40, 50, and 60 mW cm<sup>-2</sup> also produced initial bleaching rates that were statistically indistinguishable ( $P > 0.38$ ). When data from these two statistically similar treatment groups were pooled, statistical significance emerged between initial photobleaching rates observed at 10 and 20 mW cm<sup>-2</sup> vs. those lesions and margins treated at irradiances of 40-60 mW cm<sup>-2</sup> ( $P < 0.01$ ). Similarly, the bleaching rates for the lesions and margins subjected to PDT at 40-60 mW cm<sup>-2</sup> were significantly greater than that measured for PDT at 150 mW cm<sup>-2</sup> ( $P < 0.01$ ). PpIX bleaching curves, as shown in Figure 2.11, were used to determine  $D_{80}$  for each irradiance using linear interpolation of the data points for each individual lesion. As shown in Figure 3.6,  $D_{80}$  increased slowly as a function of irradiance for irradiances greater than 20 mW cm<sup>-2</sup>. The  $D_{80}$  fluence between lesion and margin were similar for all of the low-irradiance groups. A two-tailed t-test showed that  $D_{80}$ 's between lesion and margin were significantly different only at 150 mW cm<sup>-2</sup> ( $P < 0.03$ ).

Bleaching efficiency in terms of the time required to deliver the  $D_{80}$  fluence was also considered; the time required to bleach PpIX by 80% ( $T_{80}$ ) was calculated by dividing  $D_{80}$  by the irradiance (Figure 3.6). The lesion  $T_{80}$ 's were remarkably consistent for 20, 40, 50, 60 and 150 mW cm<sup>-2</sup>, ranging from

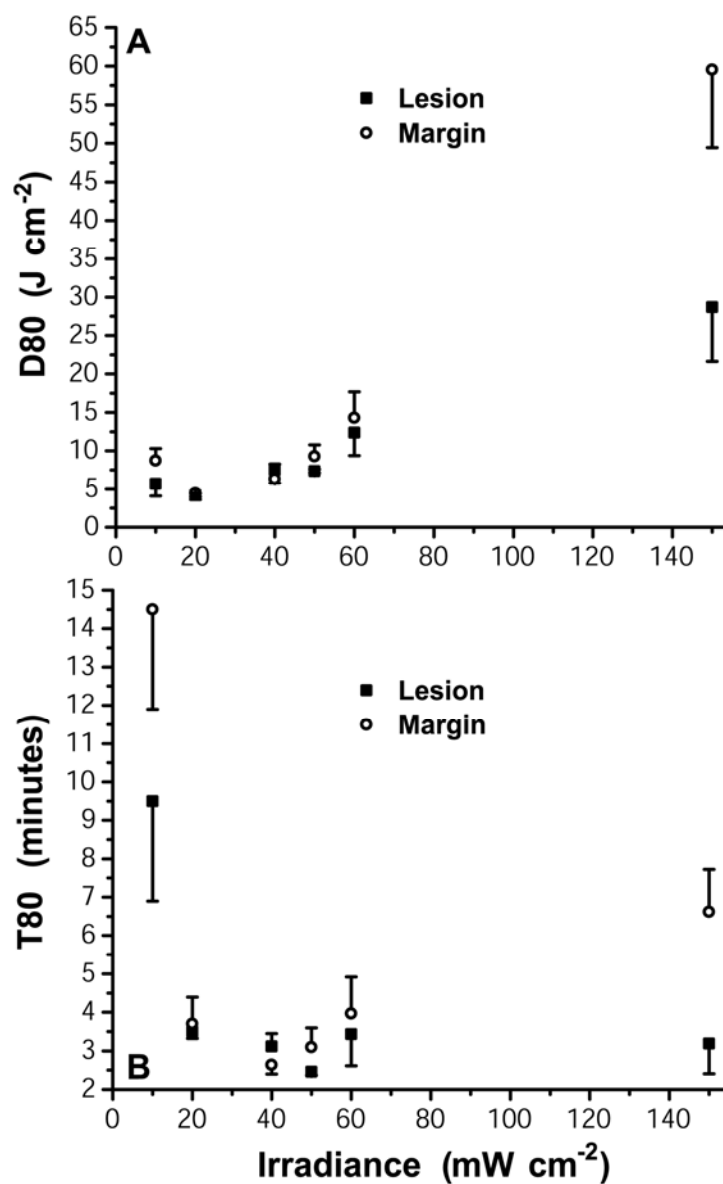


Figure 3.6: (A)  $D_{80} \pm \text{SEM}$  for irradiances of 10, 20, 40, 50, and 60  $\text{mW cm}^{-2}$ , showing a  $D_{80}$  increase with increased irradiance  $>20 \text{ mW cm}^{-2}$ . (B)  $T_{80} \pm \text{SEM}$  for irradiance groups illustrating bleaching-equivalent treatment times for 20, 40, 50, 60, and 150  $\text{mW cm}^{-2}$  irradiances in the lesion. A two-tailed t-test showed that  $D_{80}$  between lesion and margin was significantly different only at 150  $\text{mW cm}^{-2}$  ( $P < 0.03$ ).  $D_{80}$ 's and  $T_{80}$ 's are summarized in Table 3.2.

Fluence Rate (mW cm <sup>-2</sup> )	Lesion D <sub>80</sub> ± SEM (J cm <sup>-2</sup> )	Lesion T <sub>80</sub> ± SEM (min)	Low +high irradiance time (min)	Margin D <sub>80</sub> ± SEM (J cm <sup>-2</sup> )	Margin T <sub>80</sub> ± SEM (min)
10	5.7 ± 1.6	9.5 ± 2.6	31.20	8.7 ± 1.6	14.5 ± 2.6
20	4.2 ± 0.2	3.5 ± 0.2	25.26	4.4 ± 0.8	3.7 ± 0.7
40	7.5 ± 0.8	3.1 ± 0.3	24.51	6.3 ± 0.7	2.6 ± 0.3
50	7.4 ± 0.3	2.5 ± 0.1	23.86	9.3 ± 1.5	3.1 ± 0.5
60	12.4 ± 3.0	3.4 ± 0.8	24.28	14.3 ± 3.4	4.0 ± 0.9
150	28.7 ± 7.1	3.2 ± 0.8	22.22	59.5 ± 10	6.6 ± 1.1

Table 3.1: The D<sub>80</sub> fluence and T<sub>80</sub> time required for each of the low-irradiance groups to bleach PpIX by 80%, the time to reach the bleaching-equivalent fluence currently provided by the 150 mW cm<sup>-2</sup>/200 J cm<sup>-2</sup> protocol, and the delivery time required to treat at low-irradiance to D<sub>80</sub> and then deliver the remainder of 200 J cm<sup>-2</sup> at 150 mW cm<sup>-2</sup>.

$2.5 \pm 0.1$  minutes at  $50 \text{ mW cm}^{-2}$  to  $3.5 \pm 0.2$  minutes at  $20 \text{ mW cm}^{-2}$ . The  $10 \text{ mW cm}^{-2}$  irradiance exhibited a significantly larger  $T_{80}$  of  $9.5 \pm 2.6$  minutes. The time required for our two-irradiance protocol, wherein  $D_{80}$  is delivered at low-irradiance and then the remainder of the fluence is delivered at  $150 \text{ mW cm}^{-2}$ , is also presented in Table 3.1. Under this proposed protocol only modest increases to treatment time are required for initial irradiances  $\geq 20 \text{ mW cm}^{-2}$ . Clinically, 18 of 21 evaluable lesions treated with the two irradiance protocol were complete clinical responses  $\geq 6$  months after PDT (86%). This is not significantly different from the single treatment 93% CCR rate for a larger study at  $150 \text{ mW cm}^{-2}$  ( $p = 0.373$ ). There was no correlation between the initial PpIX fluorescence levels or shape of photobleaching curves and the rates of successes and failures (data not shown).

### 3.3.3 Pain

Pain was scored on a VAS scale for 27 lesions treated at 10, 20, 40, 50, and  $60 \text{ mW cm}^{-2}$  initial irradiance. Lesions treated at an initial irradiance of  $150 \text{ mW cm}^{-2}$  were excluded from pain measurements because of a previously established VAS score of above 5.

Pain experienced during the therapy  $\pm$  standard error about the mean (SEM) is listed in Table 3.2. Pain increased with escalating irradiance, shown in

<b>Irradiance (mW cm<sup>-2</sup>)</b>	<b>Low irradiance VAS ±SEM</b>	<b>High irradiance VAS ±SEM</b>
10 (n = 5*)	0.70 ± 0.46	1.75 ± 0.73
20 (n = 6)	0.25 ± 0.11	0.58 ± 0.23
40 (n = 6)	1.67 ± 0.78	1.92 ± 0.71
50 (n = 5)	0.90 ± 0.45	1.40 ± 0.51
60 (n = 5)	2.90 ± 1.48	1.20 ± 0.58**

Table 3.2: Irradiance-dependent pain experienced during ALA-PDT of sBCC, demonstrating overall low VAS scores at low-irradiance. No pain intervention was required for patients treated at 10-50 mW cm<sup>-2</sup> before or after changeover.

\*Number of lesions.

\*\*Two patients had VAS scores > 4 and were given a 1% xylocaine injection.

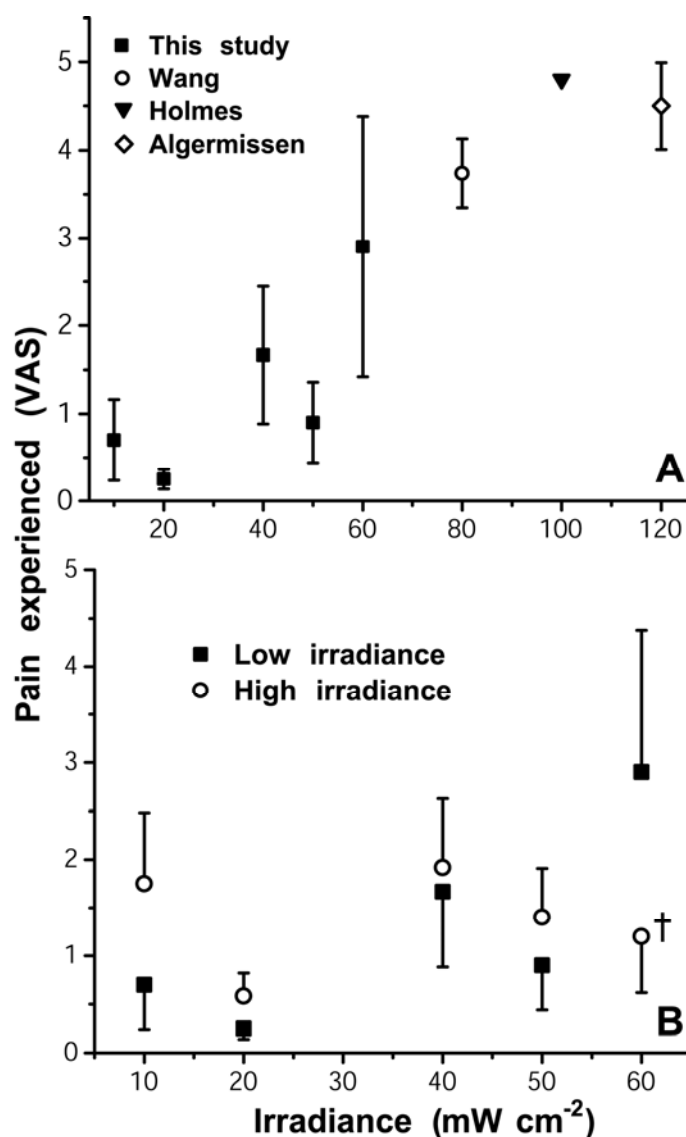


Figure 3.7: (A) VAS pain scores  $\pm$  SEM experienced with ALA-PDT of sBCC measured in this study along with results from Wang *et al.* (2001), Algermissen *et al.* (2003), and Holmes *et al.* (2004), measured at higher irradiances. (B) VAS pain scores  $\pm$  SEM during low-irradiance delivery and following changeover to 150 mW cm<sup>-2</sup> during ALA-PDT of sBCC in our study, showing only moderate increases. <sup>†</sup>Two individuals in group received 1% xylocaine injections after reporting a VAS > 4.

Figure 3.7, as anticipated by pilot evidence and supported by the literature (Algermissen *et al.*, 2003; Holmes *et al.*, 2004; Wang *et al.*, 2001). In this study, a pain threshold was established at an irradiance where two or more patients reported a VAS score of 4 or above, requiring pain intervention. This threshold was found to be  $60 \text{ mW cm}^{-2}$ , at which two out of five patients reported VAS scores of 6 and 7.

As previously mentioned, after the initial PpIX fluorescence contribution in the lesion had bleached by 90%, treatment irradiance was increased to  $150 \text{ mW cm}^{-2}$  and the treatment continued until  $200 \text{ J cm}^{-2}$  was delivered. Figure 3.7 shows the resulting change in average VAS score  $\pm$  SEM resulting from the increased irradiance. Only modest increases of less than 0.5 were noted in the 20, 40, and  $50 \text{ mW cm}^{-2}$  groups. The decrease in VAS score at  $150 \text{ mW cm}^{-2}$  for the  $60 \text{ mW cm}^{-2}$  group was primarily the result of the single 1% xylocaine injection given to the patients who reported VAS scores of 6 and 7 during the low-irradiance interval. Patients treated at  $10 \text{ mW cm}^{-2}$  reported an average VAS increase of approximately 1. Again, there was no correlation between initial PpIX levels as determined by fluorescence and pain levels (data not shown).



### 3.3.4 Reflectance

Reflectance spectra between 475 nm and 775 nm were also collected separately for both lesion and perilesion and were used to correct fluorescence spectra.

Figure 3.8 shows representative reflectance measured in one lesion treated at 150 mW cm<sup>-2</sup> before PDT and after 36 J cm<sup>-2</sup> fluence was delivered. Data between 625 and 640 nm is excluded due to bleed-through of the treatment laser into the reflectance channel. The nonlinear fitting algorithm, described in Chapter 2, determined that the blood oxygen saturations in the lesion were 77 and 75 percent pre- and post-PDT and in the margin were 76 and 69 percent pre- and post-PDT.

The fits derived from the reflectance spectra taken from each lesion and margin prior to irradiation show a mean blood oxygen saturation, SO<sub>2</sub>, of 80.6 ± 2.3 and 77.5 ± 2.4 percent, respectively. Single-factor ANOVA showed that these differences were not statistically significant ( $P > 0.36$ ). Figure 3.9 shows the mean SO<sub>2</sub> ± SEM measured at each fluence in each irradiance group from prior to the start of therapy to D<sub>80</sub> or greater. Statistical analysis using ANOVA showed no significant difference between the SO<sub>2</sub> in the lesion and the margin, with  $P > 0.44$  in all comparisons. Similarly, ANOVA was performed on SO<sub>2</sub> values for lesion and margin within each irradiance group and showed no significant change in SO<sub>2</sub> during the course of therapy for all groups ( $P > 0.88$ ).

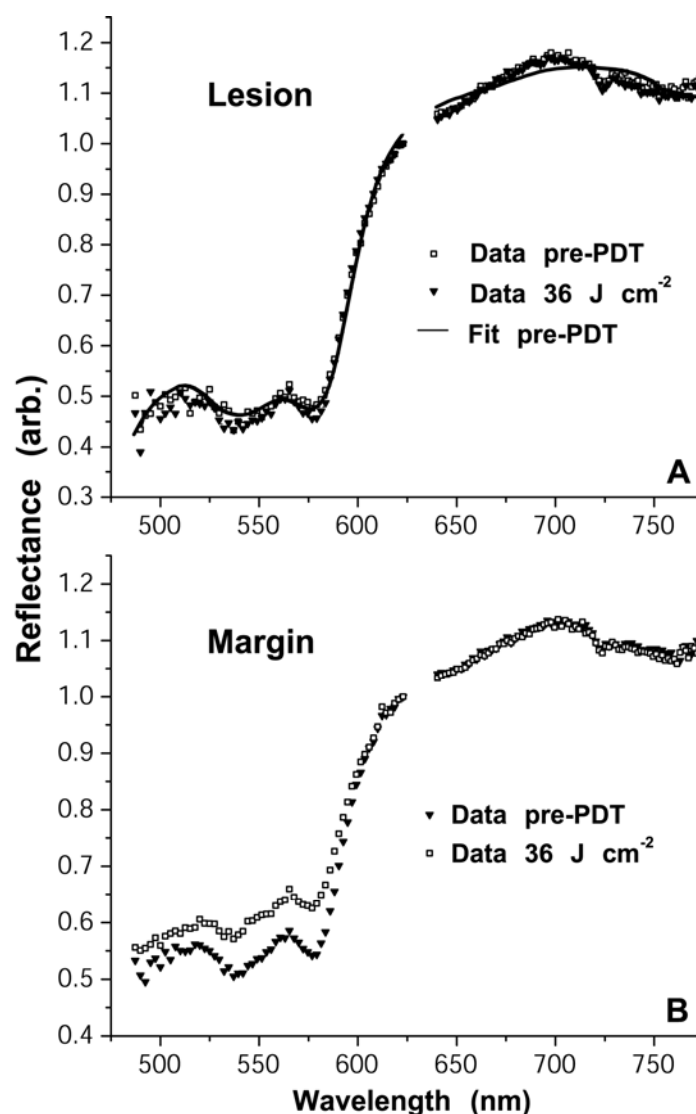


Figure 3.8: Representative reflectance spectra taken from an sBCC (A) lesion and (B) margin undergoing ALA-PDT at  $150 \text{ mW cm}^{-2}$ , taken prior to and after  $36 \text{ J cm}^{-2}$  PDT was delivered. A nonlinear fitting algorithm was used to extract blood oxygen saturations in the lesion of 77 and 75 percent pre- and post-PDT and in the margin of 76 and 69 percent pre- and post-PDT. Data between 625 and 640 nm is excluded due to bleed-through of the treatment laser into the reflectance channel.

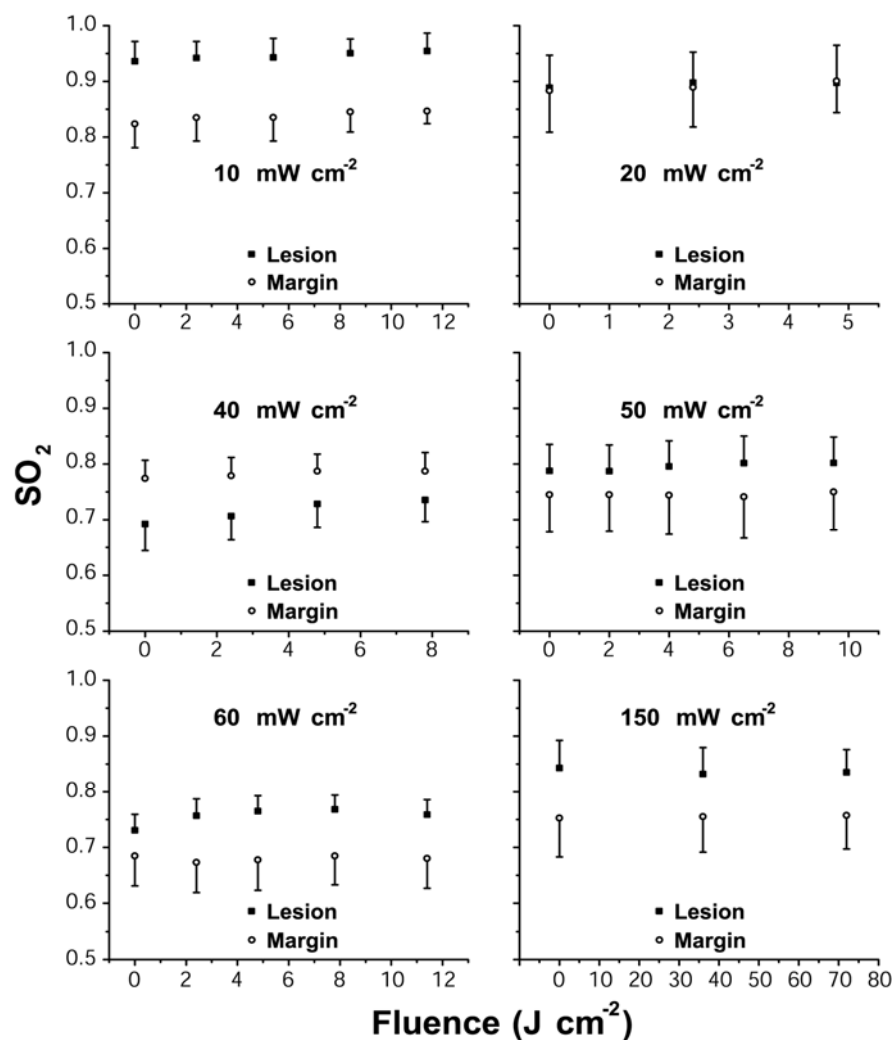


Figure 3.9: Blood oxygen saturation ( $SO_2$ )  $\pm$  SEM during the course of ALA-PDT for each irradiance group. The mean  $SO_2 \pm$  SEM measured at each fluence in each irradiance group from prior to the start of therapy to  $D_{80}$  or greater. Statistical analysis using ANOVA showed no significant difference between the  $SO_2$  in the lesion and the margin, with  $P > 0.44$  in all comparisons. Similarly, ANOVA was performed on  $SO_2$  values for lesion and margin within each irradiance group and showed no significant change in  $SO_2$  during the course of therapy for all groups ( $P > 0.88$ ).

Figure 3.10 shows the treatment-induced change to PpIX fluorescence measured at  $150 \text{ mW cm}^{-2}$  for the lesion and margin. Possible changes to blood flow induced by therapy were also examined using a comprehensive numerical model, which incorporates pharmacological and dynamic effects (Wang *et al.*, 2007). This model was able to fit modeled bleaching curves to the experimental data by adjusting only blood flow in the sampled volume. For these fits in both the lesion and margin, blood velocity was assumed to be  $300 \mu\text{m s}^{-1}$  within the vessels of the measurement region at the start of therapy. A good fit to the lesion data was found by decreasing the velocity to  $137.5 \mu\text{m s}^{-1}$  at  $8 \text{ J cm}^{-2}$ , and by further decreasing blood velocity to  $116 \mu\text{m s}^{-1}$  at  $26 \text{ J cm}^{-2}$ . Similarly, in the margin a good fit to the data was found by decreasing the velocity to  $112.5 \mu\text{m s}^{-1}$  at  $6 \text{ J cm}^{-2}$ , and by further decreasing blood velocity to  $102.5 \mu\text{m s}^{-1}$  at  $40 \text{ J cm}^{-2}$ . The model assumes a homogenous tissue with inter-capillary spacing of  $130 \mu\text{m}$ , characteristic capillary length of  $350 \mu\text{m}$ , and capillary radii of  $5.5 \mu\text{m}$ . With these parameters and an initial blood oxygen saturation of 80%, the model predicts a drop in  $\text{SO}_2$  in the lesion to 57% at  $8 \text{ J cm}^{-2}$  and 49% at  $26 \text{ J cm}^{-2}$  from the PpIX bleaching curves, and correspondingly a perilesion drop to 51% at  $6 \text{ J cm}^{-2}$  and 39% at  $40 \text{ J cm}^{-2}$ .

From the representative reflectance data presented here, we calculated similar average blood oxygen saturations in the lesions and perilesion margins for all

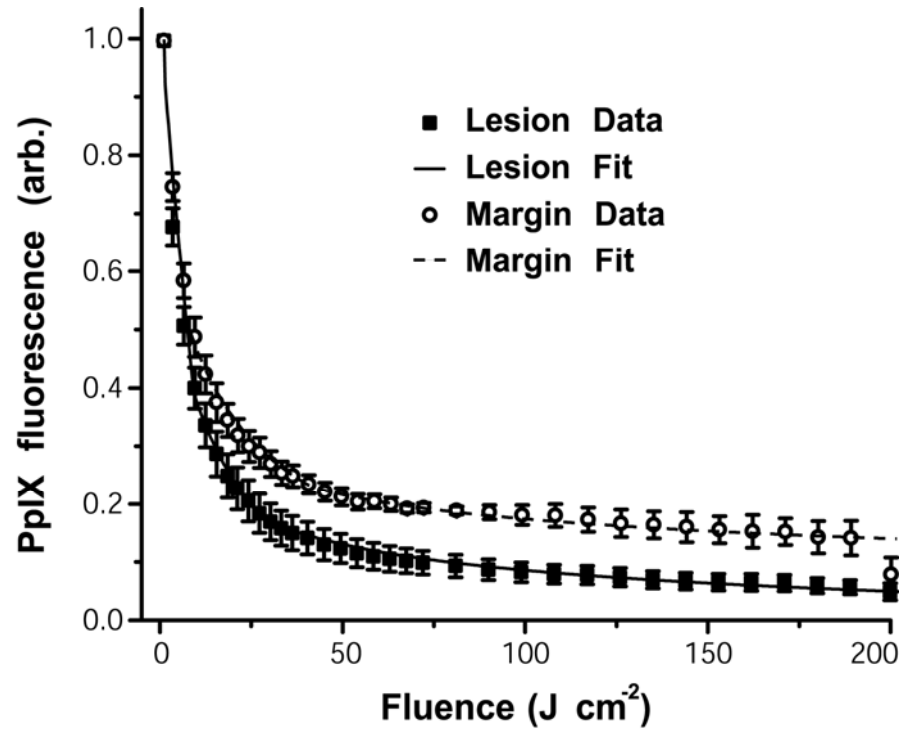


Figure 3.10: Treatment-induced change to PpIX fluorescence measured at  $150 \text{ mW cm}^{-2}$  for the lesion and margin. These fluorescence curves have been fit with a model incorporating blood flow (Wang *et al.*, 2007). In both the lesion and margin, blood velocity was assumed to be  $300 \text{ } \mu\text{m s}^{-1}$  within the vessels of the measurement region at the start of therapy. A good fit to the lesion data was found by decreasing the velocity to  $137.5 \text{ } \mu\text{m s}^{-1}$  at  $8 \text{ J cm}^{-2}$ , and by further decreasing blood velocity to  $116 \text{ } \mu\text{m s}^{-1}$  at  $26 \text{ J cm}^{-2}$ . Similarly, in the margin a good fit to the data was found by decreasing the velocity to  $112.5 \text{ } \mu\text{m s}^{-1}$  at  $6 \text{ J cm}^{-2}$ , and by further decreasing blood velocity to  $102.5 \text{ } \mu\text{m s}^{-1}$  at  $40 \text{ J cm}^{-2}$ .

irradiances. It is well known, however, that a singlet oxygen-mediated mechanism dominates bleaching of PpIX. One aspect of the analysis that may influence this apparent discrepancy relates to the volume-sensitivity of measurement.  $SO_2$  measurements are inherently a direct measure of blood oxygen and not tissue oxygenation. The dependence of local tissue oxygen concentration is related to  $SO_2$  by the Hill equation,

$$SO_2 = \frac{(pO_2)^n}{(pO_2)^n + (p_{50})^n}, \quad [3.1]$$

where  $pO_2$  is the partial pressure of oxygen,  $p_{50}$  is the partial pressure of oxygen at which 50% of the heme is bound to oxygen, typically 26 Torr, and  $n$  is the Hill parameter, typically 2.8. The bulk of the vasculature in the skin, however, is located in the underlying dermis layer, and it has been shown that the resulting contribution of oxygen to skin layers in the upper 400  $\mu\text{m}$  comes from atmospheric oxygen (Stucker *et al.*, 2002).

The Monte Carlo simulations run using the probe geometry outlined in Chapter 2 (Figure 2.10) assumed physiologically realistic lower-bound scattering and absorption of  $\mu'_s = 1 \text{ mm}^{-1}$  and  $\mu_a = 0.1 \text{ mm}^{-1}$ . These simulations determined that 50 percent of the detected photons sampled a depth of less than 0.5 mm. Similarly, the upper-bound simulation indicated that 50 percent of the detected photons sampled a depth of only 0.19 mm. This suggests that the

reflectance measurements made in this geometry may only be moderately sensitive to the blood oxygen saturation of the vascular bed.

### 3.4 Discussion

This trial represented the first systematic clinical investigation of the effect of irradiance on PpIX photobleaching efficiency and pain, and established the irradiance-dependence of patient tolerability to ALA-PDT of sBCC. Following topical ALA application, PpIX accumulates in the carcinoma, normal epidermis, and cutaneous nerve endings. Subsequent illumination causes the formation of singlet oxygen, which consumes ground state oxygen supplied from the upper and mid-dermal capillaries and from diffusion from the atmosphere (Stucker *et al.*, 2002). At sufficiently high PDT dose rates, this can lead to oxygen depletion with loss of treatment efficiency. It is, however, difficult to directly measure singlet oxygen production in patients during treatment. Furthermore, given the high complete response rates and consequent need for large sample sizes, it is not clinically feasible to carry out clinical trials of a wide range of irradiances despite the limited data available on appropriate light doses, particularly at low irradiances.

Several researchers have previously investigated implicit dosimetry in PDT (Robinson *et al.*, 1998; Robinson *et al.*, 1999). This method uses a surrogate

measure of dose, such as PpIX photobleaching, which is optically-accessible *via* fluorescence. To the extent that it results from self-sensitized reactions with singlet oxygen, photobleaching is a measure of singlet oxygen production, and the rate of bleaching is a measure of treatment efficiency. Photosensitizer photobleaching can be predictive of therapeutic outcome, and has demonstrated increased efficiency with lower irradiance (Finlay *et al.*, 2001; Robinson *et al.*, 1998; Robinson *et al.*, 1999). During this investigation, the initial slopes (beyond  $10 \text{ mW cm}^{-2}$ ) of the photobleaching curves increase with irradiance, indicating limited oxygen even at relatively low PDT dose rates. The  $D_{80}$  also increased with irradiance, as shown in Figure 3.6, illustrating less efficient bleaching at high-irradiance therapy and providing a rational way to determine a bleaching-equivalent fluence for a given treatment protocol.

Prior investigation at high irradiances, however, suggests a sigmoid dose-response, with the upper knee of the curve around  $100\text{-}150 \text{ J cm}^{-2}$ . These studies provided the foundation for the RPCI standard protocol, which requires a light dose of  $200 \text{ J cm}^{-2}$  to each treated lesion. In accordance with that protocol we increased our light delivery rate to  $150 \text{ mW cm}^{-2}$  after 90% photobleaching was detected. In this way, we were able to deliver the required  $200 \text{ J cm}^{-2}$  without a significant time penalty. Advantageously, since most of the drug was consumed in the initial low-irradiance step, no significant increase in pain was noted after



switching to high irradiance. Under this protocol pain-free ALA-PDT was delivered for initial irradiances of 20-50 mW cm<sup>-2</sup> with a modest increase in treatment time of less than 14%.

In an alternative treatment protocol PDT may be delivered at low irradiance until a bleaching-equivalent dose has been delivered. For example, 200 J cm<sup>-2</sup> delivered at 150 mW cm<sup>-2</sup> is approximately 7 times the D<sub>80</sub> fluence at that fluence rate. We may therefore expect a bleaching-equivalent, and similarly efficacious, fluence to be deposited by 7 times the D<sub>80</sub> fluence for each of the lower irradiance steps. At the highest pain-free irradiance in this study, 50 mW cm<sup>-2</sup>, this corresponds to a fluence of 51.3 J cm<sup>-2</sup> and a treatment time of 17.1 minutes. Another substitute protocol might include pain-free low-irradiance treatment to D<sub>80</sub> and then high-irradiance therapy. This would be similar to the protocol followed during this investigation.

The mechanisms leading to discrepancies in D<sub>80</sub> between lesion and margin at 150 mW cm<sup>-2</sup> (Figure 3.6) are not fully understood, although there are several physiological differences between normal and cancerous regions. SBCC blood vessels, for example, are disorganized, occupy more tissue volume, are larger in diameter, and do not have the ability to contract due to the absence of smooth muscle (Newell *et al.*, 2003; Sitnik *et al.*, 1998; Stanton *et al.*, 2003). While

oxygenation changes have been studied in nodular BCC during PDT with systemically administered Photofrin (Henderson *et al.*, 2000), we are not aware of any experiments to date that have investigated blood perfusion during ALA-PDT in human subjects, although investigators have reported on perfusion in the lesion and perilesion margin before and following ALA-PDT of sBCC, showing dissimilar trends between these regions. It has been shown that prior to ALA-PDT, perfusion in the sBCC lesion was several times that found in the margin, and blood velocity was also elevated (Enejder *et al.*, 2000; Stanton *et al.*, 2003; Wang *et al.*, 2001; Wennberg *et al.*, 2000). Additionally, investigators have found an increase in the ratio of perfusion in the lesion compared to the margin immediately following PDT (Enejder *et al.*, 2000; Wang *et al.*, 2001). During PDT, nitric oxide depletion can result in vascular constriction and local hypoxia in normal skin but not to the same extent in the sBCC tumor, as has been found in mouse models (Henderson and Fingar, 1989; Sitnik *et al.*, 1998). This suggests that perfusion variations existing between lesion and margin may play a role in oxygen availability for PDT and should be investigated further.

White-light reflectance measurements can provide estimates of blood oxygen saturation and can be used to correct fluorescence spectra. In order to make reflectance measurements in this trial, the treatment irradiation was periodically paused and white-light was transmitted through the treatment fiber. These

interruptions were brief and infrequent in order to prevent the complication of fractionation effects; acquisition times were on the order of 1 second and the duty cycle was less than 10%. The differences in initial efficiency of photobleaching shown in Figure 3.4 suggest that tissue deoxygenation was rapid and that the separation of the bleaching curves at high fluence was likely the result of a slower physiological response such as vasospasm, consistent with gradual loss of perfusion. From the reflectance data presented here, we calculated similar blood oxygen saturation in the lesion and a perilesion margin which were maintained during ALA-PDT. Hemoglobin oxygen saturation during PDT is influenced by photochemical oxygen consumption, changes in blood flow, proximity to oxygen sources, and changes in metabolic oxygen consumption. The reflectance measurements in this study may not have been acquired frequently enough to capture initial treatment transients. Additionally, modeled reflectance sampling depth in our probe geometry suggests a preferential sampling of the upper layers of the epidermis and carcinoma.

The influences of several oxygenation factors are being investigated using a newly developed comprehensive PDT model (Wang *et al.*, 2007). This PDT model incorporates the spatial and temporal dynamics of oxygen consumption *in vivo*. Photobleaching curves which were fit using this model (Figure 3.10) suggest that a much greater reduction in  $SO_2$  should be observed that was noted

in our investigation and suggests that heterogeneities in both sensitizer distribution and oxygen availability play a large role in the deposition of therapeutic dose, and correspondingly, photobleaching. Additionally, PpIX distribution studies have demonstrated varying, but continuous, distributions of PpIX to the basal layer. Topical ALA-administration typically produces PpIX highly concentrated in the epidermis and stratum cornea (Gerscher *et al.*, 2001) where oxygenation is more dominantly supplied by the atmosphere. Though the current model incorporates physiologically relevant capillary structures, it does not account for the atmospheric source of oxygen which may play a significant role in the superficial dermal layers and may be considered in future investigations.

As summarized in Table 3.3, MC simulations were used to determine likely PDT treatment, fluorescence, and reflectance probed volumes with a treatment wavelength of 632.8 nm. As seen in Table 3.3, the simulation indicated 50 percent of the fluence was delivered within the upper 1.3 mm. Similarly, 80 percent was delivered in the upper 3.0 mm. These simulations were performed for the clinical probe geometry with  $\mu'_s = 1 \text{ mm}^{-1}$  and  $\mu_a = 0.1 \text{ mm}^{-1}$  or with  $\mu'_s = 1.5 \text{ mm}^{-1}$  and  $\mu_a = 0.5 \text{ mm}^{-1}$ . These parameters correspond to low- and

high-albedo conditions for long- and short-wavelengths in normal tissue, respectively. The low-albedo parameters are physiological for long wavelength

	$\mu_s'$ (mm <sup>-1</sup> )	$\mu_a'$ (mm <sup>-1</sup> )	50%-depth (mm)	80%-depth (mm)
<b>Treatment</b>	1.0	0.1	1.3	3.0
<b>Fluorescence</b>	1.0	0.1	0.7	1.3
<b>Reflectance (blue)</b>	1.5	0.5	0.2	0.3
<b>Reflectance (red)</b>	1.0	0.1	0.5	1.2

Table 3.3: Likely PDT treatment depth compared to sampling depths of reflectance and fluorescence spectroscopies. The MC analysis, which assumes a semi-infinite and homogenous tissue slab, shows a poor overlap between likely treatment and monitored volumes. There appears to be a reasonable agreement between the volumes sampled with fluorescence above 632.8 nm and reflectance sampled in with shorter wavelengths.

light, such as the treatment beam and monitored fluorescence. Similarly, the high-albedo parameters are physiological for short wavelength light, such as reflectance in the blue part of the spectrum and the absorption peaks of hemoglobin.

This MC analysis, which assumes a semi-infinite and homogenous tissue slab, shows a poor overlap between likely treatment and fluorescence/reflectance monitored volumes. There appears to be a reasonable agreement, however, between the volumes sampled by monitored fluorescence and reflectance sampled with shorter wavelengths. Additionally, the variation in sampling depths between the high- and low-albedo conditions suggests that reflectance fitting routines may benefit from considering analysis in a piecewise fashion. This would require fitting reflectance in smaller spectral ranges but would correspondingly reduce variation in tissue optical properties.

The majority of ALA-PDT studies cite reactive pain-mitigating techniques including analgesics, water spray, air streams, and conscious sedation (Algermissen *et al.*, 2003; Holmes *et al.*, 2004; Morton *et al.*, 2002; Sandberg *et al.*, 2006), yet limited work has been done on the relationship between PDT-induced pain and various treatment parameters. In this study, which examined

treatment fields 25 mm in diameter during escalating irradiance, irradiances below  $60 \text{ mW cm}^{-2}$  alleviated the majority of discomfort associated with ALA-PDT and allowed delivery without requiring pain intervention.

Several investigators have attributed the pain experienced during PDT to light-source generated heat, often of 3 or more degrees centigrade at  $100 \text{ mW cm}^{-2}$ , though Orenstein showed that irradiation similar to that used under PDT protocols did not cause pain in normal, non-sensitized skin even with temperature increases of 5 or more degrees (Orenstein *et al.*, 1995). Algermissen similarly showed that there was no correlation between ALA-PDT-induced pain changes and changes in temperature (Algermissen *et al.*, 2003). During this study treatments were kept acceptably short by using a two-irradiance therapy. Typically, however, little change in pain score was experienced during delivery of the high-irradiance portion of the therapy, and though this study did not explicitly measure temperature during PDT, it was assumed that the thermal increase after increasing irradiance to  $150 \text{ mW cm}^{-2}$  was similar to that experienced for the group receiving only  $150 \text{ mW cm}^{-2}$ . This suggests that temperature increase is not the direct cause of pain and that pain is caused by an alternative mechanism such as PpIX accumulation in and photodynamic damage to cutaneous nerve endings. This is consistent with the low VAS scores after the switch to high-irradiance when the majority of the sensitizer had already

bleached. Based on the pain assessments in this study, irradiances using a 632.8 nm laser below  $60 \text{ mW cm}^{-2}$  are good candidates for a low-irradiance treatment protocol. Many investigators, however, perform PDT using white-light lamps and sources operating off the main absorption peak of (Brancaleon and Moseley, 2002). As demonstrated by Ericson *et al.* (2004), for a given irradiance these sources are less efficient at exciting PpIX and they therefore have a lower effective irradiance than a laser source operating near peak PpIX absorption, as was used in this study. This suggests that alternative irradiation sources operating below  $60 \text{ mW cm}^{-2}$  would also be below the pain threshold for sBCC lesions of comparable size. Since pain is expected to increase with irradiated areas, even lower irradiances may be necessary in some clinical situations. Note that PDT dose rate can be decreased by lowering either irradiance or PpIX concentration (e.g. with short application times). Both will decrease pain and increase efficiency. However, because of loss of PpIX through photobleaching, the use of low PpIX risks destroying the sensitizer before oxidative damage sufficient to cure the lesion is caused.

This trial investigated the irradiance-dependence of PpIX fluorescence photobleaching and patient tolerability to ALA-PDT of sBCC. One of the goals of our study was to determine the optimal fluence which would maximize treatment efficiency without sacrificing patient comfort. Based on therapy



efficiency, determined by bleaching, and the establishment of a pain threshold at  $60 \text{ mW cm}^{-2}$ , we conclude that  $\sim 50 \text{ mW cm}^{-2}$  at 632.8 nm may represent an optimal irradiance for ALA-PDT of sBCC, motivating a low-irradiance trial investigating efficacy at this irradiance. Assessment of treatment efficacy, durability, and cosmetic outcome is continuing for all irradiance groups. While we have not found a significant change in efficacy, PDT responses depend on both direct cell kill and host inflammatory and immune responses; it is not evident how these vary with irradiance in patients. In addition to the low-irradiance clinical trial, we are working on models of PDT dose deposition in skin and also anticipate studies assessing blood perfusion in sBCC during ALA-PDT.

In consideration of employing the proposed protocols, it should also be noted that the pain threshold established in this trial may need to be adjusted when considering the treatment of large or multiple lesions. Similarly, PpIX photobleaching efficiency at each irradiance step (Figure 3.3) was established by averaging the normalized bleaching curves for each lesion. The uncertainties are much greater than those shown for the individual lesion bleaching curves (Figure 2.11). This suggests that variances are dominated by biological and patient-to-patient differences. Optimal patient outcomes may therefore require continuous monitoring.

### 3.5 References

- Algermissen B., Osterloh D., Philipp C.M., and Berlien H.P. (2003).  
Management of ALA-PDT induced pain sensations. *Med. Laser Appl.* **18**:  
57-64.
- Brancaleon L., and Moseley H. (2002). Laser and non-laser light sources for  
photodynamic therapy. *Lasers Med. Sci.* **17**: 173-186.
- Enejder A.M.K., af Klinteberg C., Wang I., Andersson-Engels S., Bendsoe N.,  
Svanberg S., and Svanberg K. (2000). Blood perfusion studies on basal cell  
carcinomas in conjunction with photodynamic therapy and cryotherapy  
employing laser-Doppler perfusion imaging. *Acta Derm. Venereol.* **80**: 19-  
23.
- Ericson M.B., Sandberg C., Stenquist B., Gudmundson F., Karlsson M., Ros  
A.M., Rosen A., Larko O., Wennberg A.M., and Rosdahl I. (2004).  
Photodynamic therapy of actinic keratosis at varying fluence rates:  
assessment of photobleaching, pain and primary clinical outcome. *Br. J.*  
*Dermatol.* **151**: 1204-1212.
- Finlay J.C. (2003). Reflectance and Fluorescence Spectroscopies in  
Photodynamic Therapy. PhD Thesis. University of Rochester, New York.
- Finlay J.C., Conover D.L., Hull E.L., and Foster T.H. (2001). Porphyrin  
bleaching and PDT-induced spectral changes are irradiance dependent in  
ALA-sensitized normal rat skin *in vivo*. *Photochem. Photobiol.* **73**: 54-63.

- Fritsch C., Stege H., Saalman G., Goerz G., Ruzicka T., and Krutmann J. (1997). Green light is effective and less painful than red light in photodynamic therapy of facial solar keratosis. *Photodermatol. Photoimmunol. Photomed.* **13**:181-185.
- Gerscher S., Connelly J.P., van Henegouwen G.M.J.B., MacRobert A.J., Watt P., and Rhodes L.E. (2001). A quantitative assessment of protoporphyrin IX metabolism and phototoxicity in human skin following dose-controlled delivery of the prodrugs 5-aminolaevulinic acid and 5-aminolaevulinic acid-n-pentylester. *Br. J. Dermatol.* **144**: 983-990.
- Grapengiesser S., Gudmundsson F., Larko O., Ericson M., Rosen A., and Wennberg A.M. (2002). Pain caused by photodynamic therapy of skin cancer. *Clin. Exp. Dermatol.* **27**: 493-497.
- Henderson B.W., Busch T.M., Vaughan L.A., Frawley N.P., Babich D., Sosa T.A., Zollo J.D., Dee A.S., Cooper M.T., Bellnier D.A., Greco W.R., and Oseroff A.R. (2000). Photofrin photodynamic therapy can significantly deplete or preserve oxygenation in human basal cell carcinomas during treatment, depending on fluence rate. *Cancer Res.* **60**: 525-529.
- Henderson B.W., and Fingar V.H. (1989). Oxygen Limitation of Direct Tumor-Cell Kill During Photodynamic Treatment of A Murine Tumor-Model. *Photochem. Photobiol.* **49**: 299-304.
- Holmes M.V., Dawe R.S., Ferguson J., and Ibbotson S.H. (2004). A randomized, double-blind, placebo-controlled study of the efficacy of tetracaine gel (Ametop<sup>®</sup>) for pain relief during topical photodynamic therapy. *Br. J. Dermatol.* **150**: 337-340.

- Kienle A., and Patterson M.S. (1996). Determination of the optical properties of turbid media from a single Monte Carlo simulation. *Phys. Med. Biol.* **41**: 2221-2227.
- Morton C.A., Brown S.B., Collins S., Ibbotson S., Jenkinson H., Kurwa H., Langmack K., McKenna K., Moseley H., Pearse A.D., Stringer M., Taylor D.K., Wong G., and Rhodes L.E. (2002). Guidelines for topical photodynamic therapy: report of a workshop of the British Photodermatology Group. *Br. J. Dermatol.* **146**: 552-567.
- Newell B., Bedlow A.J., Cliff S., Drysdale S.B., Stanton A.W.B., and Mortimer P.S. (2003). Comparison of the microvasculature of basal cell carcinoma and actinic keratosis using intravital microscopy and immunohistochemistry. *Br. J. Dermatol.* **149**: 105-110.
- Orenstein A., Kostenich G., Tsur H., Kogan L., and Malik Z. (1995). Temperature monitoring during photodynamic therapy of skin tumors with topical 5-aminolevulinic acid application. *Cancer Lett.* **93**: 227-232.
- Press W.H., Teukolsky S.A., Vetterling W.T., and Flannery B.P. (1992). *Numerical Recipes in C*. Cambridge University Press, New York.
- Radakovic-Fijan S., Blecha-Thalhammer U., Kittler H., Honigsmann H., and Tanew A. (2005). Efficacy of 3 different light doses join the treatment of actinic keratoses with 5-aminolevulinic acid photodynamic therapy: A randomized, observer-blinded, inpatient, comparison study. *J. Am. Acad. Dermatol.* **53**: 823-827.

- Robinson D.J., de Bruijn H.S., van der Veen N., Stringer M.R., Brown S.B., and Star W.M. (1998). Fluorescence photobleaching of ALA-induced protoporphyrin IX during photodynamic therapy of normal hairless mouse skin: The effect of light dose and irradiance and the resulting biological effect. *Photochem. Photobiol.* **67**: 140-149.
- Robinson D.J., de Bruijn H.S., van der Veen N., Stringer M.R., Brown S.B., and Star W.M. (1999). Protoporphyrin IX fluorescence photobleaching during ALA-mediated photodynamic therapy of UVB-induced tumors in hairless mouse skin. *Photochem. Photobiol.* **69**: 61-70.
- Sandberg C., Stenquist B., Rosdahl I., Ros A.M., Synnerstad I., Karlsson M., Gudmundson F., Ericson M.B., Larko O., and Wennberg A.M. (2006). Important factors for pain during photodynamic therapy for actinic keratosis. *Acta Derm. Venereol.* **86**: 404-408.
- Sitnik T.M., Hampton J.A., and Henderson B.W. (1998). Reduction of tumour oxygenation during and after photodynamic therapy *in vivo*: effects of fluence rate. *Br. J. Cancer.* **77**: 1386-1394.
- Stanton A.W.B., Drysdale S.B., Patel R., Mellor R.H., Duff M.J.B., Levick J.R., and Mortimer P.S. (2003). Expansion of microvascular bed and increased solute flux in human basal cell carcinoma *in vivo*, measured by fluorescein video angiography. *Cancer Res.* **63**: 3969-3979.
- Stucker M., Struk A., Altmeyer P., Herde M., Baumgartl H., and Lubbers D.W. (2002). The cutaneous uptake of atmospheric oxygen contributes significantly to the oxygen supply of human dermis and epidermis. *J. Physiol.* **538**: 985-994.

- van Oosten E.J., Kuijpers I.M., and Thissen. M.R.T.M. (2006). Different pain sensations in photodynamic therapy of nodular basal cell carcinoma: Results from a prospective trial and a review of the literature. *Photodiagn. Photodyn. Ther.* **3**: 61-68.
- Wang I., Bendsoe N., Klinteberg C.A.F., Enejder A.M.K., Andersson-Engels S., Svanberg S., and Svanberg K. (2001). Photodynamic therapy vs. cryosurgery of basal cell carcinomas: results of a phase III clinical trial. *Br. J. Dermatol.* **144**: 832-840.
- Wang K.K.H., Mitra S., and Foster T.H. (2007). A comprehensive mathematical model of microscopic dose deposition in photodynamic therapy. *Med. Phys.* **34**: 282-293.
- Wennberg A.M., Larko O., Lonnroth P., Larson G., and Krogstad A.L. (2000). Delta-aminolevulinic acid in superficial basal cell carcinomas and normal skin - a microdialysis and perfusion study. *Clin. Exp. Dermatol.* **25**: 317-322.
- Wu J., Feld M.S., and Rava R.P. (1993). Analytical Model for Extracting Intrinsic Fluorescence in Turbid Media. *Appl. Opt.* **32**: 3585-3595.
- Zeitouni N.C., Oseroff A.R., and Shieh S. (2003). Photodynamic therapy for nonmelanoma skin cancers - current review and update. *Mol. Immunol.* **39**: 1133-1136.

# **Chapter 4**

## **Multi-modality imaging and scattering spectroscopy**

### **4.1 Introduction**

In this chapter, we report the design, construction, and initial characterization of two optical systems used for cellular scattering measurements: a forward scattering white-light spectroscopy system used to characterize lysosomal refractive index and a multifunctional scattering and fluorescence microscope that exploits an angle-resolved forward-scattering geometry. These instruments

significantly extend the capabilities of forward-scattering Fourier-optics-based scattering microscopes that have been described in the literature (Boustany *et al.*, 2001; Valentine *et al.*, 2001).

The multifunctional scattering and fluorescence microscope employs brightfield, Fourier-filtered darkfield, direct imaging of the Fourier plane, angle-resolved scattering, and white-light scattering spectroscopy while preserving a fluorescence imaging channel. Additionally, advanced designs for the scattering microscope were modeled and evaluated for the next generation instrumentation.

## **4.2 Darkfield microscope scattering spectroscopy for subcellular observation**

### **4.2.1 Darkfield scattering spectrometer instrumentation**

The initial instrumentation for darkfield scattering spectroscopy measurements was developed using a method similar to that described by Curry (2005). The system was build on a standard Nikon Diaphot inverted microscope with an oil-immersion darkfield condenser ( $NA = 1.43 - 1.2$ ) and a 20x,  $NA = 0.75$ , objective. The light source consisted of a 50 W filament lamp used for brightfield illumination in the microscope. A 1-inch-diameter lens tube was



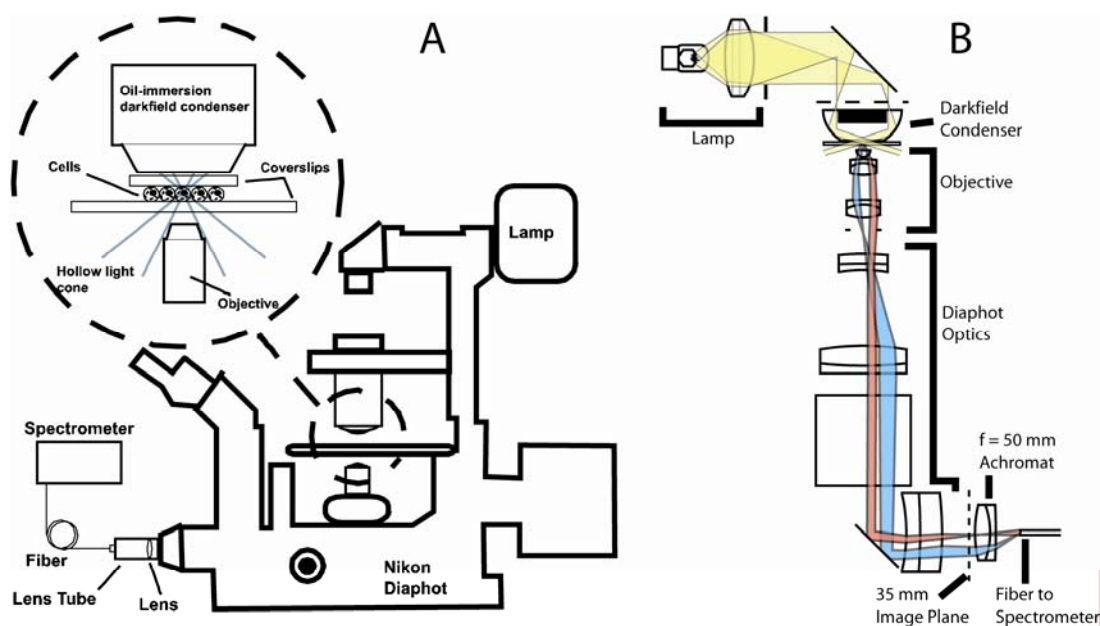


Figure 4.1: (A) Schematic of the darkfield spectrometer. This instrument was built using a standard inverted microscope with a spherical/cardioid darkfield condenser. The oil-immersion darkfield condenser formed a hollow light cone outside of the numerical aperture the microscope objective. (B) The optical paths through the darkfield spectrometer. Light scattered from the cell monolayer into a fixed angular range was collected by the objective. This light was transmitted through the remaining microscope optical chain to the 35 mm camera port. It was then collected by an optical fiber *via* a lens mounted inside a lens tube. Scattered light was spectrally resolved using a commercial spectrometer.

mounted at the 35 mm camera port of the microscope with a Nikon bayonet-to-C-mount adapter (B&H Photo Video #GBCMN, New York, NY). Light scattered into the microscope objective was imaged into the auxiliary 35 mm image plane. A 50 mm achromatic doublet (NT32-323, Edmund Optics, Barrington, NJ) mounted in the lens tube and proximal to the microscope formed a Fourier plane of the scattered-light image. This Fourier plane corresponds to the image of the back focal plane of the microscope objective. Light was then coupled into a 200  $\mu\text{m}$  core, 0.22 NA multimode fiber mounted at the Fourier plane. Light collected by that fiber was spectrally resolved with a resolution of 3 nm and digitized at 16 bits using a commercial off-the-shelf (COTS) spectrometer (BWtek BTL111-OEM, Newark, DE). Figure 4.1 shows a schematic of this setup.

#### **4.2.2 Sample preparation and measurement**

Prior to darkfield spectral measurements, 25 mm round coverslips were prepared using standard cell culture techniques (Wilson *et al.*, 2007). For measurement, these coverslips were placed cell-side down on a second 43x50 mm square No. 1 thickness coverslip to form a slide. Approximately 10  $\mu\text{l}$  of Hank's Balanced Salt Solution (HBSS) was placed between these two coverslips. The slide was then placed on the stage and brought into focus under darkfield using the

eyepiece, as shown in Figure 4.1. A spectrum of the field was then taken with an integration time between 3 and 5 s.

The darkfield spectra were corrected for dark counts and the system spectral response. For each measurement, a dark spectrum was acquired and subtracted from the data. This spectrum was acquired by measuring a coverslip without cells using the aforementioned method. The spectral response of the system was measured by removing the reflective darkfield condenser, and measuring spectra from a slide, as described above, with a scattering sample of MgO in water (Lakowicz, 1999).

### **4.2.3 Analysis**

The darkfield spectrum was a wavelength-resolved measurement of light scattered from the sample and into the objective. The NA range of the oil-immersion darkfield condenser was 1.43-1.2, which corresponded to an air-equivalent NA of 0.95-0.8. The microscope objective had an NA of 0.75, and the size of the Fourier plane at the focus of the 50 mm collection lens was approximately 1.0 mm in diameter. The 200  $\mu\text{m}$  core diameter fiber, therefore, corresponded to an effective collection NA of 0.15. This indicated that the smallest angle into which light could be scattered from the sample and into the

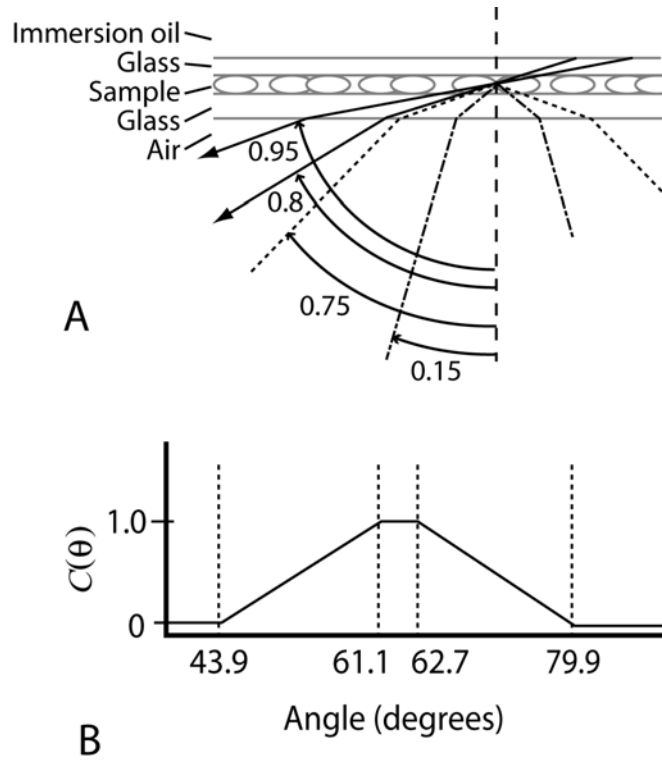


Figure 4.2: (A) Relative numerical apertures (NAs) of darkfield condenser (NA = 0.8-0.95), collection objective (NA = 0.75), and fiber collector (NA = 0.15). (B) Correction function  $C(\theta)$  accounting for the overlap of the finite scattering angular range.

spectrometer was  $43.9^\circ$ , and the largest angle was  $79.9^\circ$ , as shown in Figure 4.2. The lens was selected for approximate NA matching between the Fourier image and the optical fiber, though we did not rigorously address NA matching. We assumed an evenly illuminated and homogenous sample plane and therefore small mismatches would only affect collection efficiency.

The collected signal was essentially an integration of the angularly-resolved measurements performed in our lab (Wilson and Foster, 2005). Additionally, however, a corrective term accounting for the convolution between the finite angular ranges had to be included, as illustrated in Figure 4.2B. Thus we could model the darkfield scattering spectrum,  $I(\lambda)$ , as,

$$I(\lambda) = A \int_{43.9^\circ}^{79.9^\circ} P_{\text{total}}(\theta, \lambda) C(\theta) \sin(\theta) d\theta, \quad [4.1]$$

where  $A$  is a constant,  $P_{\text{total}}$  is as written in Equation 1.9, and

$$C(\theta) = \begin{cases} 0.058\theta - 2.55 & 43.9 < \theta < 61.1 \\ 1 & 61.1 \leq \theta \leq 62.7 \\ -0.058\theta + 4.65 & 62.7 < \theta < 79.9 \end{cases}. \quad [4.2]$$

#### 4.2.4 Experimental verification

The functionality of the instrument was verified with *in vitro* experiments on EMT6 mouse mammary sarcoma cells. Briefly, for darkfield scattering

spectroscopy measurements, EMT6 cells were grown on 25 mm round No. 1 thickness coverslips. They were incubated for 24 h in  $50 \mu\text{g ml}^{-1}$  NPe6 in complete media. The cells were kept in the dark for the incubation period and were washed in HBSS prior to measurement (Wilson *et al.*, 2007). Darkfield scattering spectra were acquired for these cells with and without incubation with  $50 \mu\text{g ml}^{-1}$  NPe6. Representative spectra are shown in Figure 4.3.

As stated in Equation 4.1, a darkfield spectrum is derived from wavelength-resolved measurements of scattering integrated over a range of angles defined by the NAs of the illumination and detection optics. The two representative spectra are identical from approximately 480 nm to 560 nm. Beyond 580 nm, control cells scatter noticeably more light than cells loaded with NPe6. At wavelengths corresponding to the laser lines used in the angularly-resolved study, the darkfield spectra reveal that control cells scatter the same amount of light into the objective at 488 nm, roughly 4% more light at 632.8 nm, and 6% more light at 658 nm. The feature near 670 nm that appears in the scattering spectrum of NPe6-loaded cells is fluorescence emission.

The darkfield spectra provided by this instrument were used with angularly resolved goniometric measurements to establish the relationship between

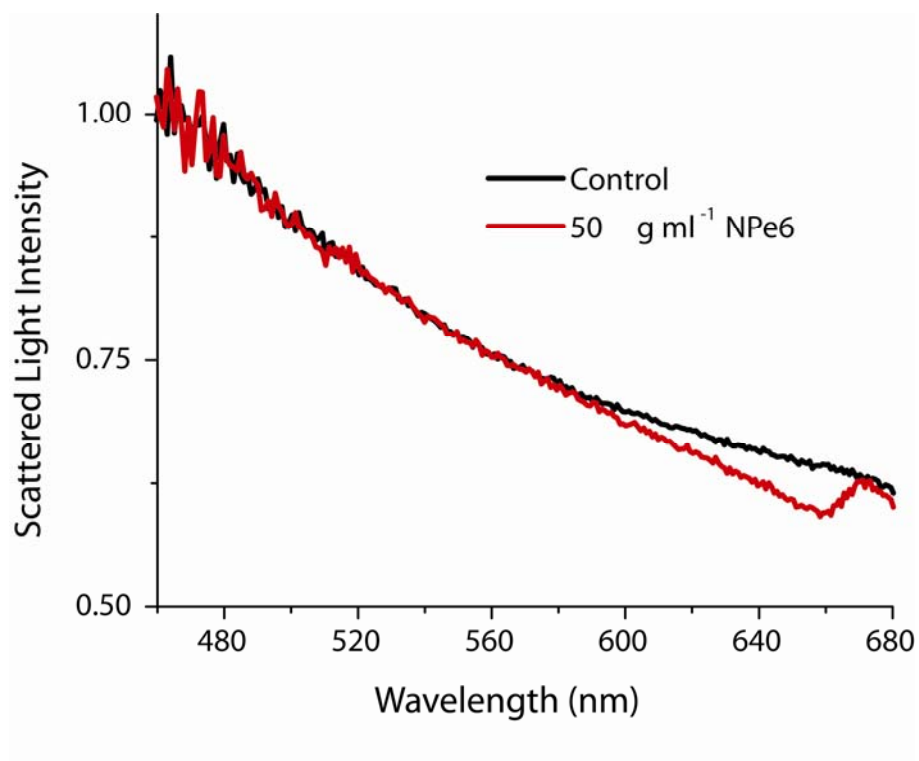


Figure 4.3: Darkfield spectra for NPe6-loaded (red) and control (black) cells. These curves were normalized to 1 at 480 nm. The feature near 680 nm is fluorescence emission from NPe6.

scattering changes and NPe6 absorption. These experiments and the resulting analysis subsequently characterized the refractive index of intact lysosomes. Additional detail on these experiments can be found in Wilson *et al.* (2007).

#### **4.2.4 Discussion**

Light scattering measurements represent an important tool for studying morphology in cell biology. This scattering spectroscopy darkfield microscope described above provided images correlated to qualitative spectroscopic data, which supported the organelle-specific dye experiments described above and elsewhere (Wilson *et al.*, 2007). The instrument, however, was limited in that it could not ensure spectroscopic data corresponded to the entire image plane and additionally did not allow collection from a target region or specific groups of cells. Furthermore, the collected Fourier signal represented integration over a wide angular range, which effectively washed out important analysis features needed for quantitative analysis. A new microscope system was therefore designed and constructed to expand the capabilities of the instrument and allow additional studies and quantitative analyses.



### **4.3 Inverted scattering microscope**

In this section of the chapter we present the design, construction, and initial characterization of a multifunctional imaging and scattering spectroscopy system built around a commercial inverted microscope platform. This instrument built on many of the basic concepts outlined above and enables co-registered brightfield, Fourier-filtered darkfield, and fluorescence imaging, monochromatic angle-resolved scattering measurements, and white-light wavelength-resolved scattering spectroscopy from the same field of view. A fiber-based illumination system provided illumination-wavelength flexibility and a good approximation to a point-source. The performance of the system in its various data acquisition modes was modeled and experimentally verified using fluorescent microspheres. This multifunctional instrument provided a platform for studies on adherent cells from which the biophysical implications of sub-cellular light scattering could be studied in conjunction with sensitive fluorescence-based techniques. A modified design form is also presented, which provides similar functionality with improved optical performance.

#### **4.3.1 Instrumentation**

A Nikon Diaphot inverted microscope served as the platform for the instrument design, which is shown in Figure 4.4. The standard illumination for a Nikon

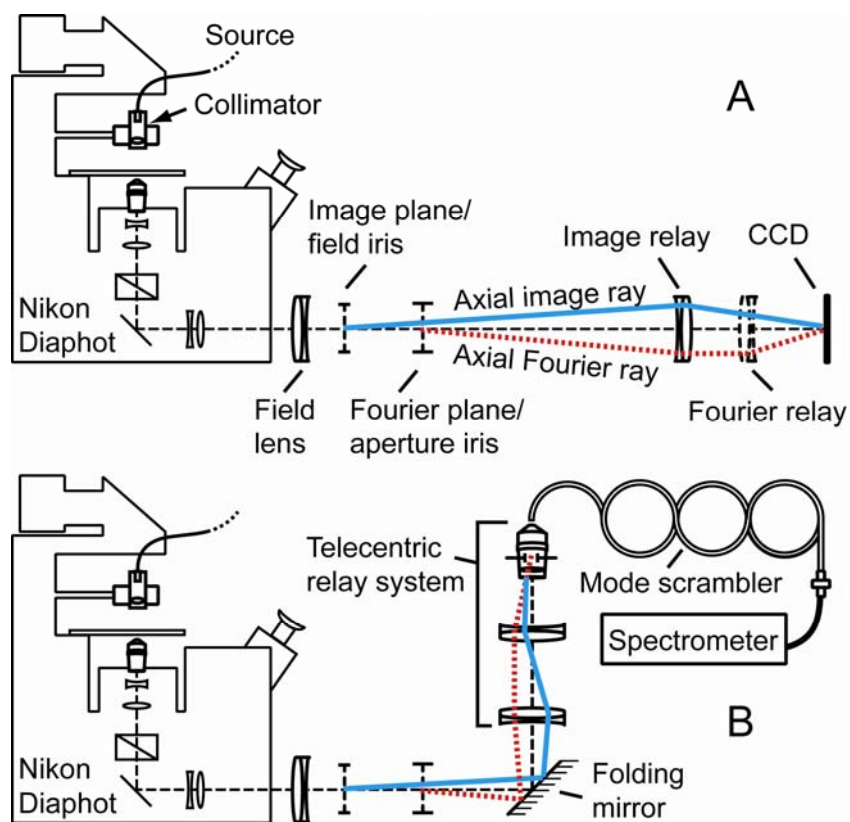


Figure 4.4: Scattering microscope in imaging (A) and spectroscopy (B) modes. Dotted and solid lines represent axial rays for Fourier and image planes in the system, respectively.

Diaphot microscope consists of a filament lamp assembly followed by an optical condenser. For our system, a fiber-based collimated illumination system replaced the incandescent lamp and was attached to the condenser mount of the microscope with a custom-machined dovetail housing and a 1-inch lens tube assembly. For monochromatic illumination, the lens tube assembly included an FC-terminated single-mode fiber that was coupled to one of several laser sources and connected to the lens tube *via* an FC chuck. The fiber output was collimated with a 5x, 0.12 NA microscope objective mounted in the lens tube. During white-light illumination, we used a similar assembly with an SMA-terminated 200  $\mu\text{m}$  core multimode fiber coupled to a tungsten halogen source (Avantes, Avalight HAL-S, Broomfield, CO). The angular divergence of the monochromatic and white-light beams were less than 1 and 3.5 mrad, respectively, and therefore approximated a collimated point source. The output beam was approximately 5 mm in diameter, thereby overfilling the sample field and maintaining a flat illumination beam profile across the object field, with intensity variations of less than 2%. The collimated illumination beam from either the white or laser sources impinged on the sample at normal incidence and both forward-scattered and non-scattered light from the sample plane was collected within the aperture of the objective. The sample plane was conjugate to the 35 mm camera port on the front of the microscope.

The optical prescription for the Nikon Diaphot imaging optics was deduced from limited vendor information, previous investigations in our laboratory (Bigelow *et al.*, 2001), and reasonable assumptions made through reverse engineering techniques. This included physical measurements of several optical elements and modeling assumptions based on the measured optical responses of the Diaphot lenses. It was determined that the imaging arm of the Diaphot between the object and the 35 mm image plane was comprised of a cover slip, microscope objective, two achromatic doublets, a directing prism, and a negative lens group prior to the 35 mm imaging plane. The first achromatic doublet is seated approximately 10 mm behind the shoulder of the objective mount and has a focal length of approximately -138.6 mm. This lens images the sample plane to infinity and collimates the beam in order to be compatible with a filter cube in the optical path. The second doublet is positioned approximately 75 mm behind the first lens and has a focal length of 138.9 mm. It sits approximately 16 mm from the prism and works with the negative group to form the 35 mm image just outside of the microscope (Figure 4.4).

In order to image the sample, a demagnifying image relay was built to re-image the 35 mm image plane onto an existing 10.8 mm CCD. To form the image relay and operate the microscope in imaging mode, a 200 mm focal length field lens (Thorlabs, AC508-200-A1, Newton, NJ) was placed approximately 1.5 cm

upstream of the 35 mm image plane of the microscope. This lens formed a real image of the rear focal (Fourier) plane of the microscope objective approximately 38 cm behind the field lens. This lens additionally worked together with a 175 mm achromat (Edmund Optics, NT32-884, Barrington, NJ) placed approximately 14 cm behind the Fourier plane to form the image relay with a magnification of approximately 0.5x. Resulting images were captured with a thermoelectrically (TE)-cooled CCD (Diagnostic Instruments, Inc., 9.0 Monochrome-6, Sterling Heights, MI). A 1.5-inch field iris was placed at the intermediate 35 mm image plane and was used with the translating microscope stage to discriminate specific regions of interest within the object field. A binary mask was positioned on a kinematic mount at the Fourier plane of the microscope objective. This allowed control over the angular content of the detected light. The mask consisted of a calibrated iris (Thorlabs, SM1D12C) and a central obscuration constructed by sputtering a thick layer of indium and gold with an optical density of approximately 6 onto a 1 mm diameter spot at the center of a 25 mm round microscope cover glass. The mask was then centered on the optical axis and adjacent to the calibrated iris. The central obscuration blocked highly forward-scattered and directly transmitted light and generated darkfield images. The outside iris similarly allowed direct control over the NA of the system and could be used to vary the range of scattering angles measured. The microscope functioned in brightfield mode by toggling the binary mask out

of the optical axis and also functioned in epifluorescence mode by using the Diaphot's mercury arc lamp and an appropriate microscope filter set (optical path not illustrated).

In order to image the Fourier plane of the system and gather scattering angle data, an auxiliary 75 mm focal length doublet (Edmund Optics, NT32-325) on a kinematic mount (Thorlabs, FM90) was toggled into place approximately 18 cm behind the imaging doublet. In this mode, the rear focal plane of the objective was imaged onto the CCD at a magnification of approximately 0.45x. Both imaging and Fourier setups are illustrated in Figure 4.4.

The 200 mm field lens was placed outside the microscope. This imaged the objectives back focal plane approximately 38 cm behind the lens. The focal plane and mask assembly position was located by directing a collimated 639 nm laser beam into the 10x microscope objective, which had been brought into focus using the eyepiece and a blank sample. The mask was located where the 200 mm lens brought that beam to its best focus. In order to position the 175 mm doublet, field iris, and CCD, the objective and the -138.6 mm achromat were removed and the same collimated beam was directed through the remaining elements. The field iris was positioned at the focus of the beam, adjacent to the field lens. The imaging doublet was located approximately

52 cm behind the 35 mm image plane and the CCD was centered on the image plane, which was again found using the best focal point of the beam. Similarly, the 75 mm doublet was positioned by replacing the objective and doublet and then directing the collimated beam through the system. The location of the 75 mm lens was optimized so that the best focal point of the beam was centered and in focus on the CCD. The resulting image plane was approximately 18 mm in diameter and overfilled the CCD, while the Fourier plane was approximately 8 mm in diameter such that the entire scattering-angle range was captured.

During spectroscopic acquisition, a kinematic mounted mirror is toggled into place and directs the signal along a second arm of the system (Figure 4.4b). The scattering spectroscopy arm of the instrument consisted of a 175 mm focal length lens (Edmund Optics, NT32-884) placed approximately 55 cm after the 35 mm image plane. This was followed by a 100 mm focal length lens (Thorlabs, AC254-100-A1) placed 25 cm behind the first. In addition an infinity-corrected 20x, 0.5 NA microscope objective was located approximately 10 cm behind the 100 mm lens (Figure 4.4). The two doublet lenses were arranged such that the intermediate image plane was conjugate to infinity prior to the 20x objective and the Fourier plane was imaged to the back focal plane of the objective. The combination of these lenses therefore formed a telecentric image relay which imaged the intermediate image onto the core of a 1.5 mm

core-diameter 0.51 NA acrylic fiber (Edmund Optics, NT02-535). By using a very large core, high NA fiber, the entire optical signal was captured and the telecentricity obviated spectroscopy calibration as a function of field location. The spectroscopic arm was brought into focus by back illuminating the acrylic fiber and imaging the fiber surface into the microscope eye piece. The optical signal in the acrylic fiber was then mode-scrambled by using mandrel wrapping (Cherin *et al.*, 1982). The signal at the distal end of the large-core acrylic fiber was sampled using a butt-coupled 200  $\mu\text{m}$  core-diameter 0.22 NA fiber and spectrally resolved and monitored with a TE-cooled 16-bit spectrometer (BWTek, BTC111-OEM, Newark, DE).

The pupil relay lens and Fourier plane masks were mounted on single-axis micrometer translation stages. This allowed simplified substitution of microscope objectives, which had various rear focal plane locations, requiring compensation. Alignment of the system for each objective was accomplished by directing a collimated laser beam into the objective, locating the best focus in the Fourier plane using the Foucault knife edge test, and then imaging the knife edge onto the CCD by adjusting a pupil relay lens translator. The image plane required no adjustment as the intermediate 35 mm image plane was fixed when the microscope was in focus.



Angular calibrations, flat-field corrections, and background measurements were generated on an objective-by-objective basis. The angular response of the system in Fourier imaging mode was calibrated by using a 30 line-pairs  $\text{mm}^{-1}$  Ronchi ruling in the object plane under collimated monochromatic illumination. The resulting Fourier pattern was imaged onto the CCD in both vertical and horizontal orientations, and CCD pixels are calibrated for angle using Bragg's law,

$$\sin(\theta_{\text{scatt}}) = \frac{m\lambda}{n_{\text{water}}d}, \quad [4.9]$$

where  $\theta_{\text{scatt}}$  is the scattering angle,  $m$  is the diffraction order,  $\lambda$  is the wavelength,  $n_{\text{water}}$  is the refractive index of water (1.3387), and  $d$  is the slit width of the ruling. To correct for stray light, CCD dark counts, and background scattering, a measurement was taken using a sample of distilled water at the same exposure time and subtracted from the data. Flat-field correction terms were generated by measuring the response of the system to an approximated Lambertian source comprised of a 7-mm-thick sample of a scattering emulsion. Under these conditions, photons in the medium were sufficiently randomized, and the emulsion-coverslip interface emits isotropically and uniformly over the entire field. Division of acquired data by this correction accounted for pixel-by-pixel response, variations in the excitation beam profile, and the optical response of the system.

For studies made using microsphere samples, slides were assembled by pipetting 10  $\mu\text{l}$  of microspheres in suspension onto a 45 x 45 mm square No. 1 thickness coverslip and covering the liquid with a round 25 mm No. 1 coverslip.

### 4.3.2 Results

We demonstrated the functionality of the instrument in each mode of operation by measuring samples of fluorescent polystyrene microspheres (Molecular Probes, F-8859, Eugene, OR) suspended in distilled water. These spherical scattering centers had a narrow size distribution ( $4.0 \pm 0.014 \mu\text{m}$ ), a refractive index of 1.59 at 500 nm (Ma *et al.*, 2003), and were both absorbing and fluorescent, providing a model system that could be exploited by every data acquisition mode of the instrument. To enhance the demonstration of the instrument's angle-resolved scattering mode, we also used a sample of  $2 \pm 0.08 \mu\text{m}$  polystyrene microspheres. For monochromatic illumination, we used the 457.9 nm line from an  $\text{Ar}^+$  laser, and for collection, a 10x, 0.45 NA water immersion objective. Representative data sets are shown in Figure 4.5. In imaging mode, there was excellent spatial agreement in (A) brightfield, (B) darkfield, and (C) fluorescence modes. In Fourier-plane imaging mode (D), we saw the far-field diffraction pattern from the spheres. Annular binning of the

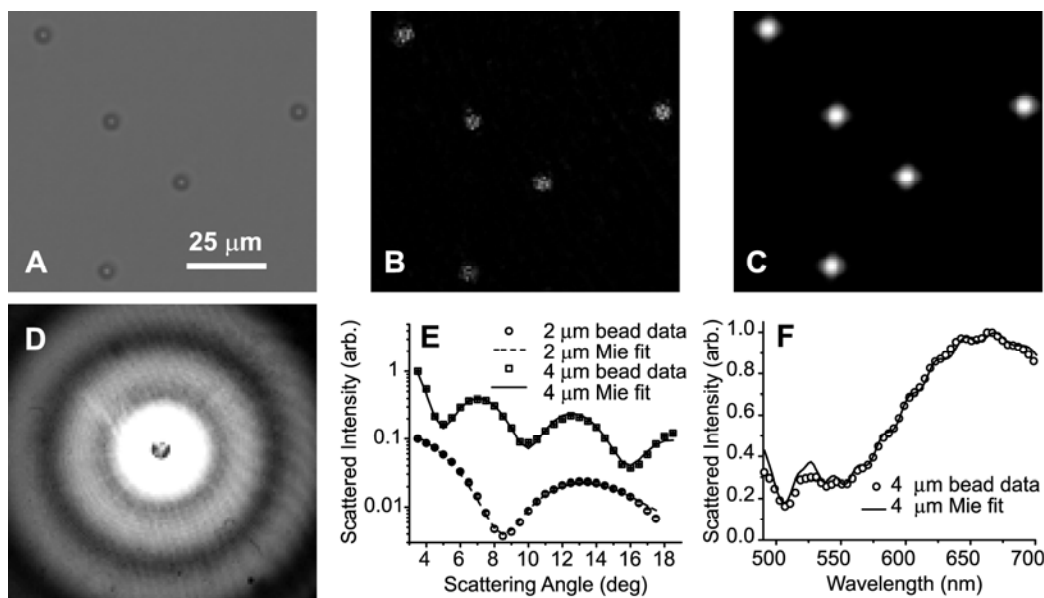


Figure 4.5: Representative data from 4  $\mu\text{m}$  diameter fluorescent polystyrene microspheres. Brightfield (A), darkfield (B), and fluorescence images (C) of the same field of view and the corresponding Fourier-plane image (D) illustrate unprocessed CCD data. Annular binning of the Fourier image results in an angle-resolved scattering measurement that can be fit by Mie theory (E), where data and Mie fits for 4 and 2  $\mu\text{m}$  beads are shown (offset for clarity). In spectroscopy mode, a wavelength-resolved scattering spectrum and absorbing-sphere Mie fit (F) are shown.

Fourier image provided an angle-resolved measurement (E) that could be fit with a Mie theory model. Here our fit predicted the size distribution to be  $4.05 \pm 0.001 \mu\text{m}$ . Shown on the same axis (offset for clarity) are data from the  $2 \mu\text{m}$  polystyrene spheres mentioned above with a Mie theory fit that predicted a diameter of  $2.01 \pm 0.10 \mu\text{m}$ . Spectroscopic data from the  $4 \mu\text{m}$  spheres are shown in Figure 4F. These data were fit using an absorbing-sphere Mie theory model in which the wavelength-dependent absorption is accounted for explicitly using a basis spectrum that was measured by fluorescence excitation. The free parameters were the mean and standard deviation of the particle size, fluorophore concentration, and particle refractive index. The fit, displayed as a solid line, predicts  $3.93 \pm 0.02 \mu\text{m}$  diameter particles. The fit was extremely sensitive to refractive index, predicting 1.599, while changing the refractive index by 0.01 degraded  $\chi^2$  by 50%.

The ability of our instrument to measure fluorescence and angle-resolved scattering from the same field of an adherent cell monolayer is shown in Figure 4.6. EMT6 mouse mammary tumor cells were grown on coverslips and incubated with the photodynamic therapy sensitizer Pc 4 at a concentration of 250 nM overnight in the dark. Upon irradiation in cells, Pc 4 undergoes enhanced fluorescence emission and at low photodynamic doses induces scattering changes consistent with mitochondrial swelling (Wang *et al.*, 2007).

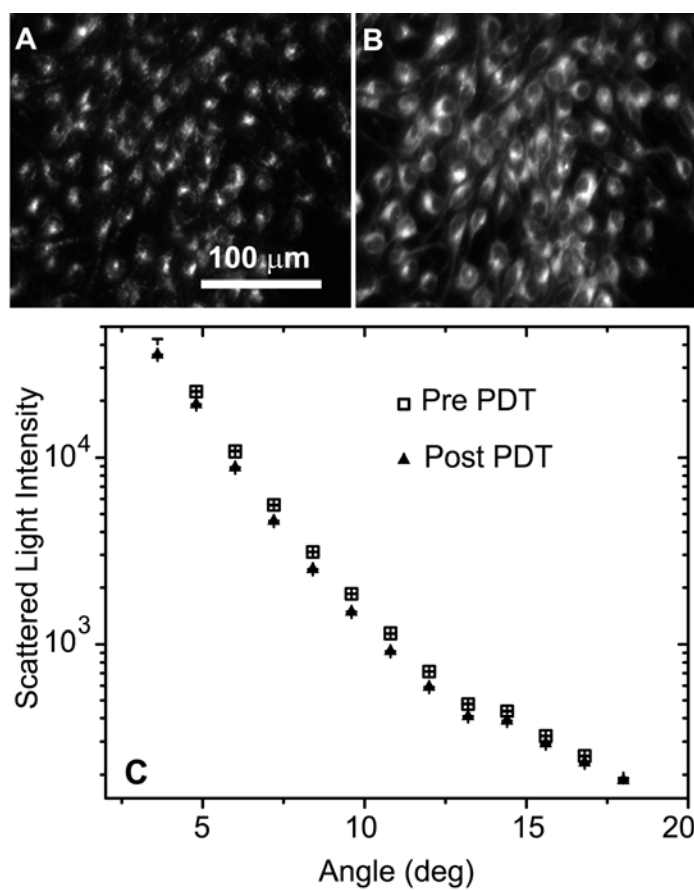


Figure 4.6: Fluorescence images of EMT6 cell monolayers following overnight incubation with 250 nM Pc 4 pre- (A) and post-PDT (B) with  $600 \text{ mJ cm}^{-2}$  irradiation at 667 nm. Angularly resolved light scattering data (C) from the binned Fourier plane images for these same cell populations.

The cells were imaged on the microscope in fluorescence mode and in Fourier imaging mode using light from a 658 nm diode laser. They were then irradiated on the stage of the microscope with  $600 \text{ mJ cm}^{-2}$  at 667 nm, and the measurements were repeated. As expected, the fluorescence intensity of Pc 4 (Figure 4.6) was significantly lower pre- (A) vs. post-irradiation (B). The reduction in scattering in the treated cells in the angular range 3- 15 degrees was consistent with mitochondrial swelling (Wang *et al.*, 2007; Wilson *et al.*, 2005).

The optical performance of the imaging arm in both image and Fourier modes was modeled using CodeV (Pasadena, CA) and identified highly aberrated images. The primary aberrations in imaging mode were spherical and coma (Figure 4.7). This can be attributed primarily to the COTS achromats, which were optimized for infinite conjugate use and not the 0.5 reduction in our system. In addition, a large amount of coma can be seen in the spot diagrams and was identified in the edge of the image field (not shown). In Fourier mode, the aberrations resulting from the external doublets were also large and dominated by astigmatism. These aberrations were qualitatively verified using the Foucault knife edge test. The demonstrated aberrations in the Fourier imaging mode, however, were observed to be even greater than modeled and had a significant amount of spherical aberration. It was determined by later design considerations that these aberrations likely resulted from the internal

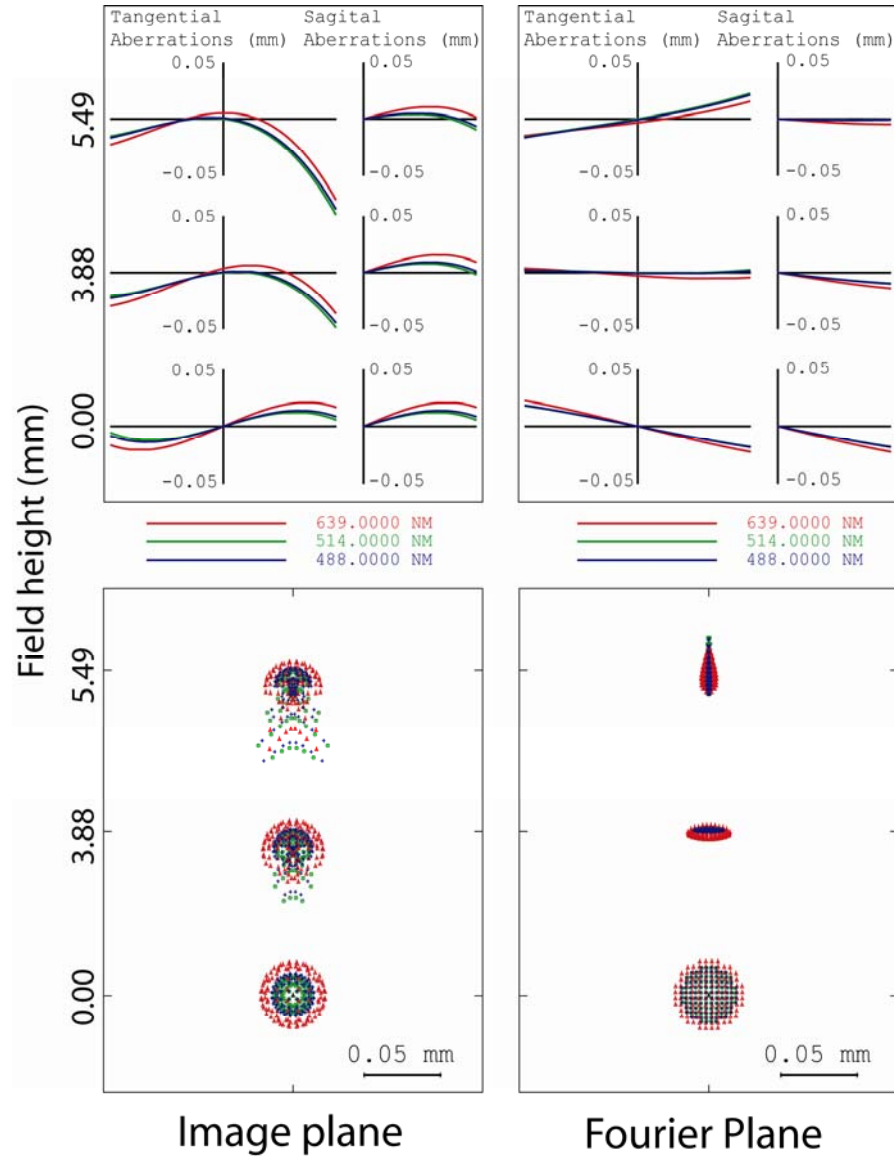


Figure 4.7: (top) Ray intercept plots and (bottom) spot diagrams of the optical response of the external optics in both the image and Fourier modes of the scattering microscope. This model reveals that spherical aberration and coma dominate in imaging mode and astigmatism dominates in Fourier mode.

optics of the microscope being optimized for image relay and thus were not adequately designed to operate at the conjugates required during Fourier plane imaging.

### 4.3.3 Design considerations

We have considered an upgrade to the system which would make use of the side imaging port of the microscope and would allow high-quality imaging as well as the advanced spectroscopy and Fourier imaging techniques to be employed. We employ a design which includes a zoom lens module which would allow variation of the system magnifications for both the image and Fourier planes and also allows minor adjustments to the focal plane location. For this design, we modeled the first-order optical prescriptions for the objective and Diaphot lenses with aberration free CodeV lens modules, specified in Table 4.1. According to the modeled microscope system, the side-port image plane is located approximately 10 cm behind the prism and is approximately 15 mm in diameter, consistent with earlier findings (Bigelow *et al.*, 2001). The internal microscope optics form an imaginary image of the objective's rear focal plane approximately 360 mm in front of the image plane with a diameter of approximately 26 mm. For the first-order design we selected an effective focal length (EFL) of 100 mm for the field lens positioned at the intermediate image of the side port. This formed a real image of the Fourier plane with a diameter



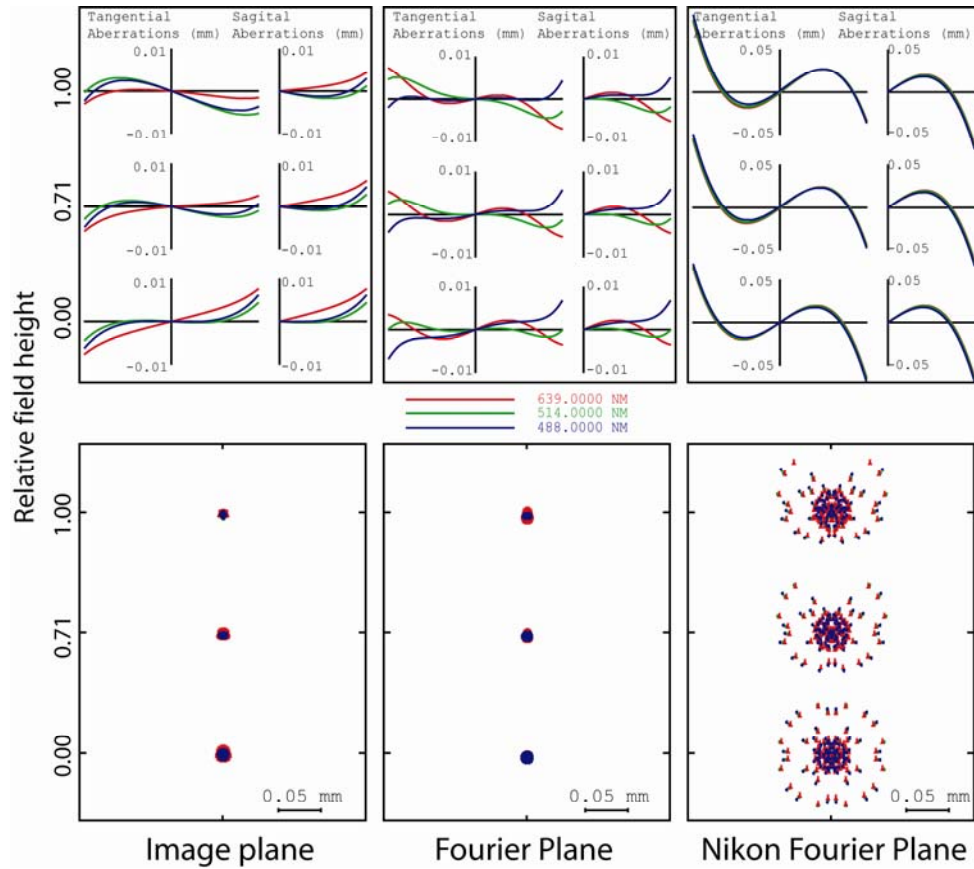


Figure 4.8: (top) Ray intercept plots and (bottom) spot diagrams for the optics in image and Fourier modes, including Nikon side-port optics of the instrument. This model revealed that the aberration contribution in the imaging lens design is dominated by spherochromatism and the Fourier lens is dominated by higher order spherical and spherochromatism. Similarly, the aberrations introduced by using the Nikon Diaphot optics at different conjugates are dominated by spherical.

of approximately 9 mm located 13 cm from the lens. Similarly, in order to form the image plane in this same location, a negative achromat was designed with an EFL of -118 and located approximately 80 mm from the Fourier plane. This allowed for the addition of a COTS macro zoom lens with a working distance of 9 cm and a magnification range of 0.7-4.5x (Edmunds, VZM 450). Achromatic doublet lenses were designed using standard techniques (Laikin, 2006) using BK7-SF5. The positive achromat was optimized using CodeV for imaging the Fourier plane. The negative achromat was similarly optimized to image the sample plane while the positive field lens was in place. Therefore, high quality images of the sample or Fourier planes could be formed at the CCD and optimized with the zoom lens for a specific sub-field of interest. The expected aberrations from this design are shown in Figure 4.8. Additionally, we used the CodeV model to approximate the aberrations that may be introduced into the Fourier plane from the internal Nikon Diaphot optics (Figure 4.8) and which dominate the aberrations in the Fourier imaging configuration.

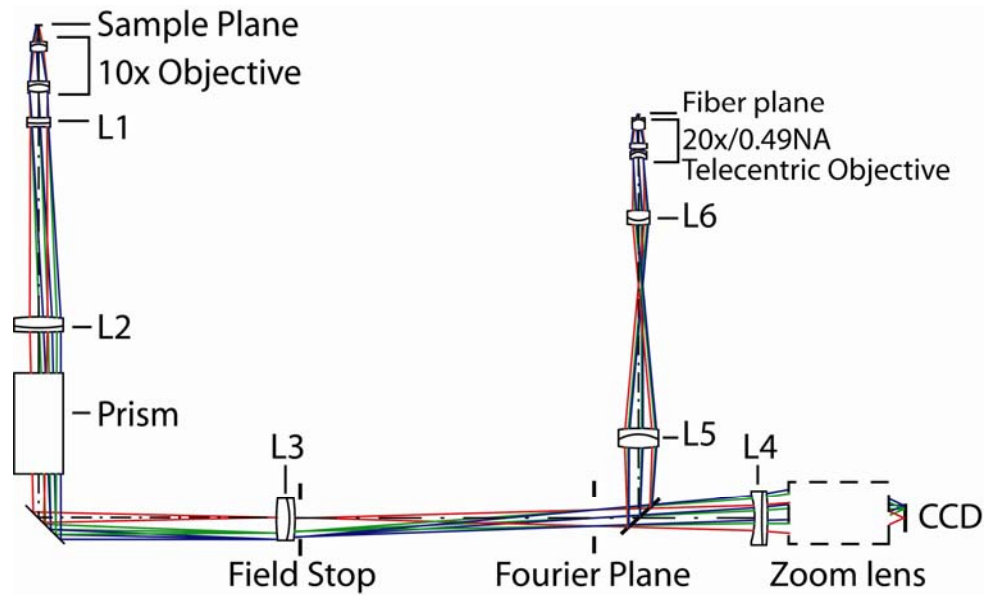


Figure 4.9: Ray trace through scattering microscope upgrade in imaging mode. The specifications for the optical elements used in the model are listed in Table 4.1.

Element	Specification (length in mm)	
<b>10x Objective</b>	CodeV Lens Module (f = 16.6)	
<b>L1</b>	CodeV Lens Module (f = -138.6)	
<b>L2</b>	CodeV Lens Module (f = 138.9)	
<b>Prism</b>	Material = BK7 Length = 39.5	
<b>L3</b>	Material = BK7-SF5 thickness 1 = 6.34 thickness 2 = 2.99	radius 1 = 80.43 radius 2 = -37.37 radius 3.= -85.51
<b>L4</b>	Material = BK7-SF5 thickness 1 = 3.28 thickness 2 = 2.63	radius 1 = -45.30 radius 2 = 111.39 radius 3.= -449.01
<b>Zoom Lens</b>	CodeV Lens Module Magnification = 0.7 - 4.5X	
<b>L5</b>	Material = BAF10-SF10 thickness 1 = 6.344 thickness 2 = 2.756	radius 1 = 52.08 radius 2 = -19.25 radius 3.= -69.54
<b>L6</b>	Material = SF10-BAF10 thickness 1 = 2.10 thickness 2 = 4.75	radius 1 = 28.31 radius 2 = 9.41 radius 3.= -33.08

Table 4.1: Optical prescription for the scattering microscope, illustrated in Figure 4.9. The optical elements of the Nikon Diaphot were primarily modeled using CodeV lens modules. The remaining optical elements were designed as discrete achromatic doublets, which were optimized in CodeV.

The simple toggle-based design was maintained in order to switch between the Fourier and imaging modes in order to keep the design of the zoom lens simple and keep the overall system length small. Similarly, the spectroscopy arm was designed by modeling the microscope objective as a 20x/0.49 NA lens and optimizing a pair of BAF10-SF10 achromats. The resulting optical ray diagrams are shown in Figure 4.9 and the results are summarized in Table 4.1.

#### **4.3.4 Discussion**

The microscope in its present form represents a significant step forward in the field of organelle-specific light scattering. The design of this system extends the work of Boustany *et al.* (2001) and that of Valentine *et al.* (2001) by integrating all of the capabilities of both systems as well as adding a scattering spectroscopy mode. With the functionality of multimodal scattering data acquisition and multimodal imaging from the same field of view, the instrument enables several interesting lines of investigation. Motivated by the exquisite sensitivity of the spectroscopy arm to the index of refraction of absorbing particles, one can imagine a range of experiments in which different organelle populations are stained with high-extinction absorbing/fluorescent dyes, and their refractive indices are measured within an absorbing-particle model as presented above. As demonstrated by (Boustany *et al.*, 2004), fluorescence-based molecular imaging techniques combined with light scattering measurements can help researchers to

make connections between biochemical cellular signaling pathways and morphological changes measured with light scattering.

## 4.4 References

- Bigelow C.E., Harkrider C.J., Conover D.L., and Foster T.H. (2001). Retrofitted confocal laser scanner for a commercial inverted fluorescence microscope. *Rev. Sci. Instrum.* **72**: 3407-3410.
- Boustany N.N., Kuo S.C., and Thakor N.V. (2001). Optical scatter imaging: subcellular morphometry *in situ* with Fourier filtering. *Opt. Lett.* **26**: 1063-1065.
- Boustany N.N., Tsai Y.C., Pfister B., Joiner W.M., Oyler G.A., and Thakor N.V. (2004). BCL-x(L)-dependent light scattering by apoptotic cells. *Biophys. J.* **87**: 4163-4171.
- Cherin A.H., Head E.D., Lovelace C.R., and Gardner W.B. (1982). Selection of mandrel wrap mode filters for optical fiber loss measurements. *Fiber Int. Opt.* **4**: 49-66
- Curry A., Nusz G., Chilkoti A., and Wax A. (2005). Substrate effect on refractive index dependence of plasmon resonance for individual silver nanoparticles observed using darkfield micro-spectroscopy. *Opt. Express.* **13**: 2668-2677.
- Laikin M. (2006). Lens Design, 4<sup>th</sup> edition. CRC Press, New York.
- Lakowicz J.R. (1999). Principles of fluorescence spectroscopy. Plenum Press, New York.
- Ma X.Y., Lu J.Q., Brock R.S., Jacobs K.M., Yang P., and Hu X.H. (2003) Determination of complex refractive index of polystyrene microspheres from 370 to 1610 nm. *Phys. Med. Biol.* **48**: 4165-4172.

- MacDonald I.J., Morgan J., Bellnier D.A., Paszkiewicz G.M., Whitaker J.E., Litchfield D.J., and Dougherty T.J. (1999). Subcellular localization patterns and their relationship to photodynamic activity of pyropheophorbide-a derivatives. *Photochem. Photobiol.* **70**: 789-797.
- Pandey R.K., Sumlin A.B., Constantine S., Aoudia M., Potter W.R., Bellnier D.A., Henderson B.W., Rodgers M.A., Smith K.M., and Dougherty T.J. (1996). Alkyl ether analogs of chlorophyll-a derivatives. Synthesis, photophysical properties and photodynamic efficacy. *Photochem. Photobiol.*, **64**: 194-204.
- Reiners J.J., Caruso J.A., Mathieu P., Chelladurai B., Yin X.M., and Kessel D. (2002). Release of cytochrome c and activation of pro-caspase-9 following lysosomal photodamage involves bid cleavage. *Cell Death Differ.* **9**: 934-944.
- Valentine M.T., Popp A.K., Weitz D.A., and Kaplan P.D. (2001). Microscope-based static light-scattering instrument. *Opt. Lett.* **26**: 890-892.
- Wang K.K.H., Wilson J.D., Kenney M.E., Mitra S., and Foster T.H. (2007). Irradiation-induced enhancement of Pc 4 fluorescence and changes in light scattering are potential dosimeters for Pc 4-PDT. *Photochem Photobiol.* **83**: 1056-1062.
- Wilson J.D., Bigelow C.E., Calkins D.J., Foster T.H. (2005). Light scattering from intact cells reports oxidative-stress-induced mitochondrial swelling. *Biophys. J.* **88**: 2929-2938.



- Wilson J.D., Cottrell W.J., and Foster T.H. (2007). Index of refraction-dependant sub-cellular light scattering observed with organelle-specific dyes. *J. Biomed. Opt.* **12**: 014010.
- Wilson J.D., and Foster T.H. (2005). Mie theory interpretations of light scattering from intact cells. *Opt. Lett.* **30**: 2442-2444.

## Chapter 5

### **Focal flash photolysis instrument for *in vitro* $\text{Ca}^{2+}$ release studies**

#### **5.1 Introduction**

Intracellular calcium concentration  $[\text{Ca}^{2+}]_i$  signals are central to the mechanisms underlying fluid and protein secretion in pancreatic and parotid acinar cells. The signals in each cell type exhibit characteristic temporal and spatial properties, and although their general characteristics are similar, some important differences have been reported. The mechanisms which underlie these differences are not fully understood.

There are a variety of techniques to study  $\text{Ca}^{2+}$  dynamics. Local stimulation and monitoring is available using mechanical stimulations and patch clamps, respectively. Similarly, non-invasive techniques such as full-field molecular uncaging of messengers like inositol trisphosphate ( $\text{InsP}_3$ ) coupled with fluorescence  $\text{Ca}^{2+}$  monitoring allow minimal cellular disruption. It is important to note, however, that these measurements can be limiting: dialysis from the patch pipette will disrupt the native buffering of the cytoplasm and thus may influence the spatial and temporal properties of the signal. Similarly, under physiological conditions, cells are unlikely to experience spatially uniform increases in  $\text{InsP}_3$  as is the result of full-field photolysis.

$\text{Ca}^{2+}$  release was therefore studied in polarized cells following focal laser photolysis of caged molecules, using an instrument of our own design. A relatively simple means of locally releasing chemically caged molecules using focal laser photolysis was designed and constructed. This method, combined with the use of cell-permeable forms of caged- $\text{InsP}_3$  and caged- $\text{Ca}^{2+}$ , allowed local stimulation to be obtained in intact cells. Following intense, local stimulation using this instrumentation, the  $\text{Ca}^{2+}$  signals were monitored with fluo-4 fluorescence imaging. The resulting studies compared the mechanisms underlying the  $\text{Ca}^{2+}$  signal globalization in these individual exocrine cell types and under regional messenger release.

## **5.2 Materials and methods**

### **5.2.1 Design and characterization of focal laser photolysis instrument**

Focal photolysis instrumentation was built on a standard Nikon TE300 inverted microscope platform, accessed through the rear illumination port. Photolysis was performed using a UV laser (Innova Enterprise; Coherent, Santa Clara, CA), operating at 363.8 nm and coupled into the microscope through a dual-port UV flash condenser (Till-Photonics, Pleasanton, CA) as shown in Figure 5.1. The laser output was directed through a neutral density filter wheel (FW102; Thorlabs, Newton, NJ) and a mechanical shutter before being coupled into a single UV mode, 0.12 NA silica fiber (SM400N; Coastal Connections, Anaheim, CA) using an under filled 20x, 0.45 NA microscope objective. The single mode fiber was intentionally displaced along the optical axis by several hundred microns from best beam focus. This system was not power limited and this displacement increased throughput stability. Output from the distal end of the fiber was measured to ensure that this did not excite supported cladding modes in the fiber, which could have affected beam quality.

The output of the distal end of the fiber was relayed to an intermediate focus within the condenser system at the focal plane of the primary condenser lens, using a pair of aspheric lenses (C220TM, C280TM, Thorlabs). A dichroic beam

splitter allowed the UV beam to enter the condenser and preserved the functionality of a flash-lamp system already in place. The laser was roughly collimated by the condenser lens at a beam diameter of  $\sim 18$  mm, which slightly overfilled the entrance aperture of the same 40x objective used for imaging. A layer of fura-2 was placed between cover slips on the microscope stage. The location of the asphere illumination assembly was then adjusted along the optical axis such that the UV beam was focused in the sample plane when the microscope was monitoring fluorescence.

In order to evaluate the optical design and help with alignment, the system was modeled in CodeV (Pasadena, CA). Lens prescriptions for the aspheres used in the fiber relay and the prescription for the condenser doublet were provided by their respective manufacturers and are listed in Table 5.1. Lens prescriptions for microscope objectives are not generally available, and we were unable to obtain performance specifications on the 40x objective at 363.8 nm from the vendor.

In order to model the objective we therefore used a Nikon 40x, 1.3 NA immersion objective design form which was obtained through the United States Patent and Trademark Office (Furutake, 1998). The optical prescription in the patent was optimized for the visible spectrum using catalog glasses. The resulting complete optical system prescription is provided in Table 5.1 and illustrated in Figure 5.2A.

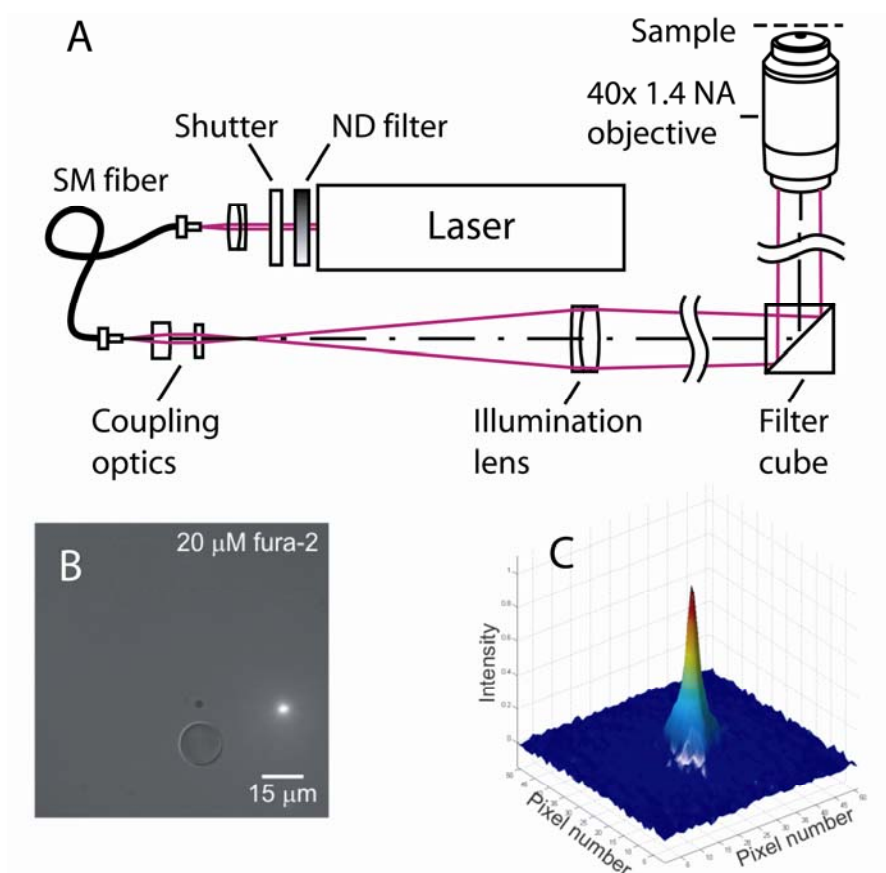


Figure 5.1: Experimental setup for focal laser photolysis and optical characterization. (A) A 363.8-nm laser is coupled through a single mode (SM) optical fiber into the illumination port of a Nikon TE300 inverted microscope and brought to a focus in the sample plane using the imaging objective. ND, neutral density; NA, numerical aperture. (B) Visualization of the laser spot size. The system was used to excite a field containing 20  $\mu\text{M}$  fura-2. The spot size is illustrated in relation to a 15- $\mu\text{m}$  polystyrene bead fixed on the cover-slip. (C) 3D graphical representation of the fluorescence intensity at the image plane of the CCD.

The model of the optical system specified in Table 5.1 allowed an assessment of the optimum performance of a well-aligned system (Figure 5.2). This model revealed that the limiting aberration was a small amount of third order spherical which resulted from optical elements within the microscope objective. The model also suggested that we should be able to obtain an on-axis point spread function less than  $1\text{ }\mu\text{m}$  full width at half maximum (FWHM). Similarly, the FWHM of the intensity profile along the optical axis (perpendicular to the sample plane) was determined to be approximately  $2.1\text{ }\mu\text{m}$ .

Following alignment, the beam focus in the sample plane was characterized. The edge spread function (ESF) was measured experimentally, as outlined below. The line spread function was then generated by taking the first order numerical derivative of the ESF. Using known Fourier techniques and assuming cylindrical symmetry of the optical system, the LSF was used to compute the experimental PSF (Marchand, 1964).

The experimental setup for measuring the ESF is shown in Figure 5.3. The edge of a stainless steel surgical blade was polished to an edge roughness of  $\sim 50\text{ nm}$  and mounted  $\sim 1\text{ mm}$  from the active region of a plastic encapsulated photodiode (OPT101; Texas Instruments, Dallas, TX), using transparent epoxy. This device was mounted to the electronic translation stage of the microscope and oriented

	Radius (mm)	Thickness (mm)	Material		Radius (mm)	Thickness (mm)	Material
1	Fiber tip	7.33	Air	18	-25.2	1.1	K1 China
2	Infinity	5.0	C0550 Corning	19	43.6	6.45	CAF2 Schott
3	-6.63*	7.0	Air	20	-9.56	1.85	SLAL8 Ohara
4	10.98**	2.2	C0550 Corning	21	-17.33	0.05	Air
5	Infinity	15.5	Air	22	20.31	7.05	CAF2 Schott
6	Infinity	102	Air	23	-15.09	1.3	KVC79 Sumita
7	139.7	2.5	LF5 Schott	24	-68.8	0.1	Air
8	39.8	5.3	FK5 Schott	25	13.31	7.3	CAF2 Schott
9	-66.8	300	Air	26	-22.19	1.1	PK2 China
10	12.09 <sup>†</sup>	1.7	TIF2 China	27	30.77	0.1	Air
11	20.79	0.1	Air	28	12.05	3.4	K1 China
12	12.09	3.75	PK2 China	29	47.07	0.1	Air
13	128.0	6.1	MTAF101 Hoya	30	6.15	3.35	K1 China
14	5.48	3.05	Air	31	9.9147	0.1	Air
15	-5.20	7.1	BAK1 China	32	3.5214	3.35	MTAF101 Hoya
16	-1999.5	4.85	K1 China	33	1.0508	0.65	BK7G18 Schott
17	-9.50	0.1	Air	34	Sample	0.4865	BK7

\* Conic constant = -0.55, 4<sup>th</sup> order =  $-4.4 \times 10^{-7}$ , 6<sup>th</sup> order =  $-3.8 \times 10^{-7}$

\*\* Conic constant = -0.54, 4<sup>th</sup> order =  $-4.5 \times 10^{-6}$ , 6<sup>th</sup> order =  $-4.9 \times 10^{-8}$

† System stop

Table 5.1: Optical prescription for focal flash photolysis system in CodeV. Lens prescriptions for the aspheres used in the fiber relay (elements 2-5) and the prescription for the condenser doublet (elements 7-9) were provided by their respective manufacturers. The Nikon 40x, 1.3 NA immersion objective (elements 10-33) was reverse engineered from United States Patent 5,982,559 (Fututake, 1998).



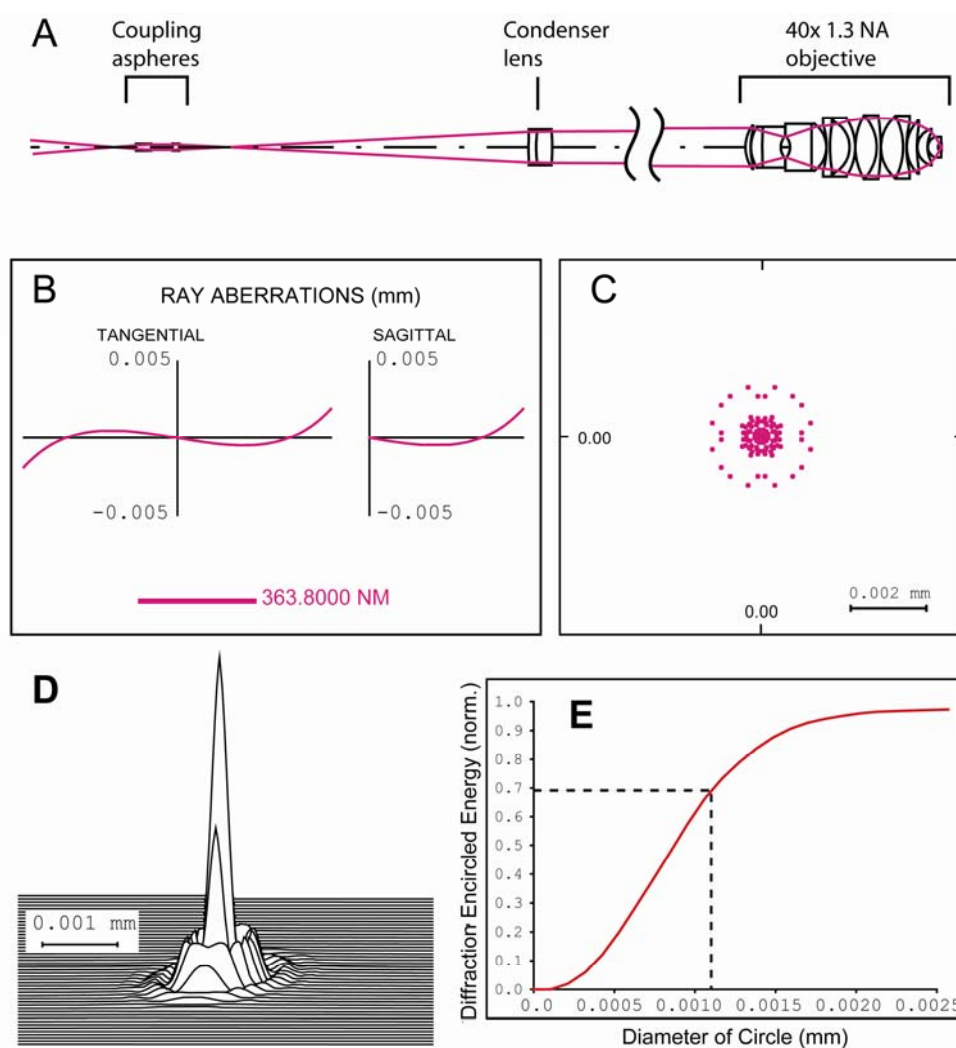


Figure 5.2: Modeled optical performance of (A) the focal flash photolysis instrument. The primary on-axis aberration at 363.8 nm is third-order spherical, determined from the characteristic (B) ray curves and (C) spot diagram. The model predicted that the (D) on-axis point spread function of the system at best focus would be  $< 1 \mu\text{m}$  FWHM and that (E) 70% of the energy would be contained in a spot  $1.1 \mu\text{m}$  in diameter.

such that the edge of the blade was at a slight angle,  $\theta$ , with respect to the direction of stage translation,  $Y$ . Therefore, as shown in Figure 5B, as the stage was translated along the  $y$ -axis, the edge translated through the beam a distance,  $X$ , equal to  $Y$  times the tangent of  $\theta$ . This technique was used to increase the spatial resolution of the measurement beyond that of the microscope stage. The power incident on the detector was recorded as the blade edge passed through the beam.

A sigmoid function of the form

$$\text{ESF}(x) = v_a \text{erf}(v_b x + v_c) + v_d x + v_e \quad [5.1]$$

was used to fit the ESF data using least squares, where  $v_a, v_b, v_c, v_d$ , and  $v_e$  were fit constants,  $\text{erf}$  is the Gaussian error function, and  $x$  is the edge translation: the stage translation multiplied by the tangent of the edge angle with respect to the stage translation axis. Representative ESF data and the corresponding sigmoid fit to Equation 5.1 are shown in Figure 5.3B. The first derivative of the ESF is the LSF. The Fourier transform of the LSF is equivalent to a slice through the two-dimensional Fourier transform of the PSF. Therefore, we can numerically find the two-dimensional PSF by taking the one-dimensional Fourier transform of the LSF, rotating it about the vertical axis, and taking the two-dimensional inverse Fourier transform.

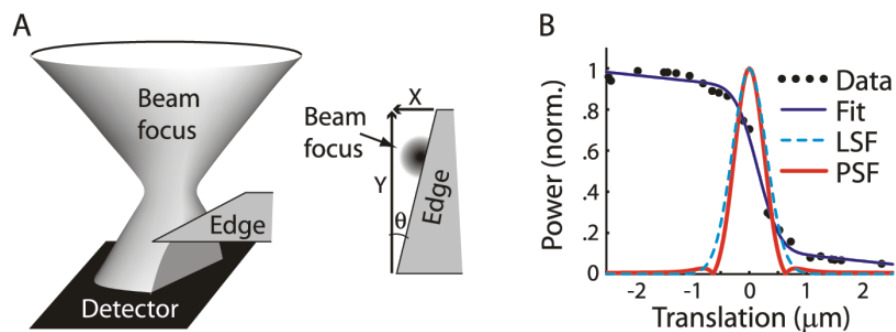


Figure 5.3: Experimental setup for focal laser photolysis PSF characterization. (A) The focus in the sample plane was characterized using a scanning edge detector to characterize the edge spread function of the system. (B) Representative edge spread function data, line spread function (LSF), and point spread function (PSF). The full width at half maximum (FWHM) of the PSF at best focus measured 0.65 and 0.74  $\mu\text{m}$  in the x- and y-axes of the sample plane, respectively. The modeled FWHM along the z-axis is 2.1  $\mu\text{m}$ .

The PSF-FWHM defines the spot size of the photolysis system as mentioned above. At best focus, the PSF-FWHM measured 0.65 and 0.74  $\mu\text{m}$  in the x- and y-axes, respectively. The slight asymmetry of the PSF was likely the result of unaccounted aberrations of the objective at the excitation wavelength and system misalignments. These results suggest that  $\sim 70\%$  of the optical power is contained inside a spot with a 1.1  $\mu\text{m}$  diameter, allowing precisely targeted molecular uncaging within a well-defined intense focal volume. The proper UV intensity for uncaging was determined empirically and corresponded to approximately 78  $\mu\text{W}$  output from the single mode fiber. The optical model suggested a low transmission throughput of approximately 30% through the entire optical chain, resulting from reflections and absorption by the optical elements. This indicates that the maximum intensity in the sample plane was approximately  $10^{-7} \text{ W } \mu\text{m}^{-2}$ .

### 5.2.2 Experimental setup

The experiments described in the sections below were carried out in the Yule laboratory at the University of Rochester and are described in detail by Hak Won *et al.* (2007). These experiments are described briefly in this section with representative data to illustrate the functionality of the aforementioned flash photolysis instrumentation. All experiments were reviewed, approved by, and carried out in compliance with policies of the University Committee on Animal

Resources at the University of Rochester. The investigation conforms to the Guide for the Care and Use of Laboratory Animals, published by the National Institutes of Health (NIH Publ. No. 85-23, revised 1996).

Both parotid and pancreatic cell types were harvested from NIH-Swiss mice (25 g) as previously described (Evans *et al.*, 1999; Williams *et al.*, 2006). Before experimentation, cell suspensions from pancreas or parotid were loaded by incubation with 4  $\mu$ M fluo-4-AM and either Ci-InsP<sub>3</sub>/PM (cell-permeable InsP<sub>3</sub>) or NP-EGTA-AM (cell-permeable caged-Ca<sup>2+</sup>). Cells were then seeded on coverslips and mounted on the stage of the Nikon TE300 inverted microscope. Solution changes were accomplished by selecting flow from a multi-chambered, valve-controlled, gravity-fed reservoir. [Ca<sup>2+</sup>]<sub>i</sub> imaging was performed essentially as described previously (Straub *et al.*, 2000; Wagner *et al.*, 2004; Hak Won and Yule, 2006) by using an inverted epifluorescence Nikon microscope with a 40x oil immersion objective lens (numerical aperture, 1.3). Fluorescence was excited at  $488 \pm 10$  nm using a monochromator (TILL Photonics), and fluorescence images were captured and digitized with a digital camera driven by TILL Photonics Vision software. Images were captured every 40–80 ms with an exposure of 10 ms and 2x2 pixel binning. Changes in fluo-4 fluorescence are expressed as  $\Delta F/F_0$ , where  $\Delta F$  is the difference between

fluorescence captured at two different times, and  $F_0$  is the mean of the initial 10 fluorescence images.

Before initiating experiments, the position of the UV focal volume was located in relation to the field of view by illuminating a fura-2 solution placed on the coverslip as shown in Figure 5B. Similarly, the beam was focused in the z-plane using a motorized z drive to obtain the brightest spot on the camera. The camera chip coordinates of the brightest pixel were recorded and regarded as the center of the spot illumination. Cells were positioned using the motorized stage such that the focal volume irradiated the desired region of the cell. Photolysis of caged compounds was accomplished following a brief (50 ms) shutter opening. In initial experiments it was determined empirically that a power density of  $\sim 10 \mu\text{W } \mu\text{m}^{-2}$  was sufficient to effectively uncage both NP-EGTA and Ci-InsP<sub>3</sub>. The energy resulting from this laser exposure did not have any obvious deleterious effects on  $[\text{Ca}^{2+}]_i$  in cells not incubated with cage but loaded with dye and was therefore used throughout the study.

### 5.3 Results

Representative cellular responses of photolysis of Ci-InsP<sub>3</sub> in parotid acinar cells are shown in Figure 5.4 (Hak Won *et al.*, 2007). This experiment monitored the

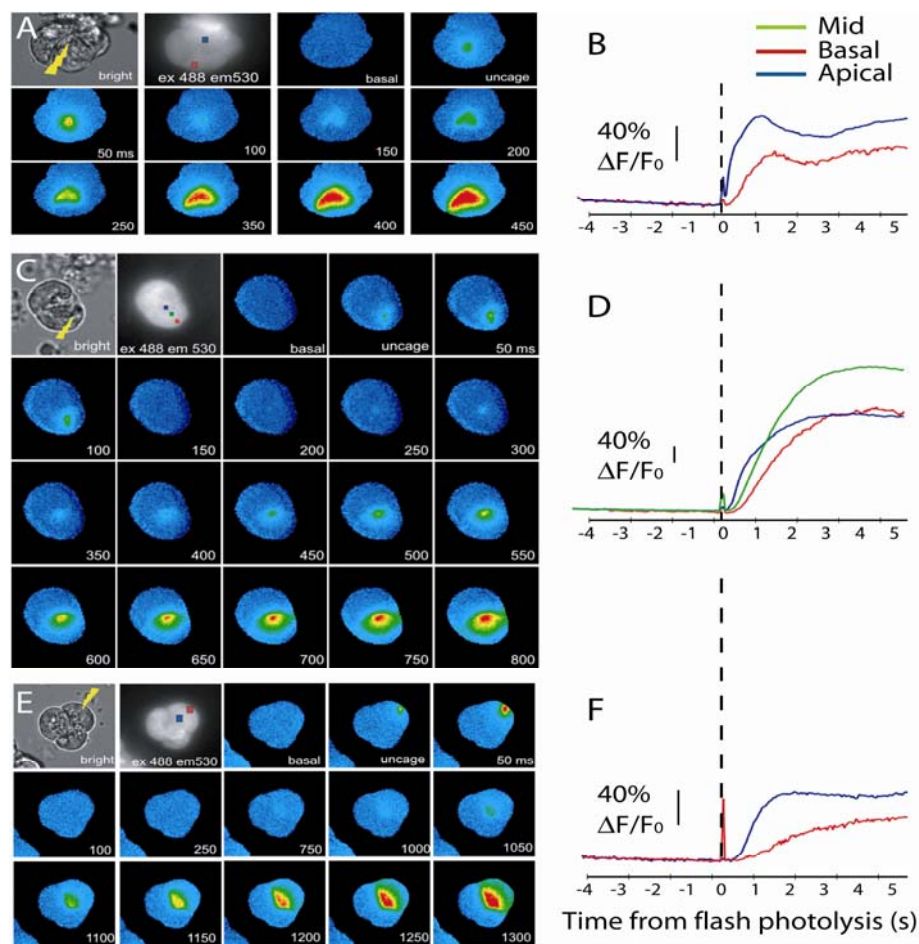


Figure 5.4: Photolysis of Ci-InsP<sub>3</sub> in parotid acinar cells. (A) Time course images of cells incubated with Ci-InsP<sub>3</sub> and fluo-4. Focal uncaging in the apical region of one cell (lightning bolt in bright field image). The images show the initiation Ca<sup>2+</sup> signal in the apical domain followed by propagation to the basal region. The corresponding kinetic recorded from an apical (blue box) or basal (red box) are shown in (B). Apical photolysis resulted in the rapid initiation of an apical-to-basal wave. (C) Images and (D) kinetics: photolysis performed at a central location showed limited increase in [Ca<sup>2+</sup>]<sub>i</sub> at the photolysis site followed by an apical-to-basal Ca<sup>2+</sup> wave. (E) Images and (F) kinetic: Photolysis in the basal pole of a pancreatic acinus. A limited Ca<sup>2+</sup> signal was observed at the photolysis site, followed by an apical-to-basal wave (Hak Won *et al.*, 2007).

spatial and temporal characteristics of the  $\text{Ca}^{2+}$  signals evoked by  $\text{InsP}_3$ . The resulting data helped define relative sensitivities of various subcellular regions to  $\text{InsP}_3$  and investigated the role of  $[\text{Ca}^{2+}]_i$  feedback to the observed signals. Representative  $[\text{Ca}^{2+}]_i$  time course data are also shown in Figure 5.4.

Previous reports have shown that the apical region of salivary gland acinar cells constitutes a “trigger zone” where  $\text{Ca}^{2+}$  signals are initiated following exposure to  $\text{InsP}_3$  or agonist stimulation. This was tested by focal photolysis at sites throughout small parotid acini. When the laser was positioned at the apical pole of the cell, photo release of  $\text{InsP}_3$  resulted in  $\text{Ca}^{2+}$  release at the spot site followed rapidly by extensive  $\text{Ca}^{2+}$  release from the trigger zone, as shown in Figure 5.4 (A,B). Following initiation, the  $\text{Ca}^{2+}$  propagated throughout the cell as a true  $\text{Ca}^{2+}$  wave. Next, photo release of  $\text{InsP}_3$  was performed in the mid-cellular region. As shown in Figure 5.4 (C,D), photo release in the mid region resulted in modest  $\text{Ca}^{2+}$  release at the site of photolysis but did not result in a propagating wave from the photolysis site. This suggests that this cytoplasmic region of the parotid acinar cell does not express sufficient density of IPR to support the initiation of a propagating wave. Following a brief interval, a  $\text{Ca}^{2+}$  wave was initiated at the trigger zone which propagated toward the basal pole of the cell. Additionally, no regenerative  $\text{Ca}^{2+}$  wave occurred at the



photolysis site in the extreme basal pole, as shown in Figure 5.4 (E,F). Instead, an apical-basal  $\text{Ca}^{2+}$  wave propagated after an interval.

In summary, focal photolysis and subsequent release of  $\text{InsP}_3$  in any region of the cell resulted only in a modest transient  $\text{Ca}^{2+}$  signal at the photolysis site followed by initiation of a  $\text{Ca}^{2+}$  wave from the extreme luminal pole of the cell, traveling at a fixed velocity in each particular cell type. Furthermore a latent period between photolysis and wave initiation was closely related to the distance between the photolysis site and the trigger zone. These observations are consistent with activation of an "all or none" process, a primary characteristic of a true propagating wave, which relies on the sequential recruitment of release sites throughout the cytoplasm.

## 5.4 Discussion

A system to deliver a small focal volume of intense UV laser illumination delivered through a high NA objective on a standard inverted microscope was designed and developed. The equipment facilitated experiments to locally photo release cell-permeable caged second messengers, allowing a comparison of the spatial and temporal characteristics of  $\text{Ca}^{2+}$  signaling events in two distinct but related polarized exocrine cells. The design of the apparatus was optically straightforward and was relatively inexpensive to construct and could be

duplicated by other investigators with similar experimental needs. The experimental paradigm was designed primarily to investigate signaling events in natively buffered intact cells and secondarily to more closely approximate local production of messengers likely to occur under physiological stimulation of the gland *in situ*. These studies revealed that the individual cell types exhibit both similar and divergent characteristics, which appear to occur largely as a consequence of utilizing common pathways.

## 5.5 References

- Giovannucci D.R., Bruce J.I., Straub S.V., Arreola J., Sneyd J., Shuttleworth T.J., and Yule D.I. (2002). Cytosolic  $\text{Ca}^{2+}$  and  $\text{Ca}^{2+}$ -activated  $\text{Cl}^-$  current dynamics: insights from two functionally distinct mouse exocrine cells. *J. Physiol.* **540**: 469–484.
- Hak Won J., Cottrell W.J., Foster T.H., and Yule D.I. (2007).  $\text{Ca}^{2+}$  release dynamics in parotid and pancreatic exocrine acinar cells evoked by spatially limited flash photolysis. *Am. J. Physiol. Gastrointest. Liver. Physiol.* **293**: G1166-G1177
- Lee M.G., Xu X., Zeng W., Diaz J., Wojcikiewicz R.J., Kuo T.H., Wuytack F., Racymaekers L, and Muallem S. (1997). Polarized expression of  $\text{Ca}^{2+}$  channels in pancreatic and salivary gland cells. Correlation with initiation and propagation of  $[\text{Ca}^{2+}]_i$  waves. *J. Biol. Chem.* **272**: 15765–15770.
- Leite M.F., Burgstahler A.D., and Nathanson M.H. (2002).  $\text{Ca}^{2+}$  waves require sequential activation of inositol trisphosphate receptors and ryanodine receptors in pancreatic acini. *Gastroenterology* **122**: 415–427.
- Li Q., Luo X., and Muallem S. (2004). Functional mapping of  $\text{Ca}^{2+}$  signaling complexes in plasma membrane microdomains of polarized cells. *J. Biol. Chem.* **279**: 27837–27840.
- Marchand E.W. (1964). Derivation of the point spread function from the line spread function. *J. Opt. Soc. Am. A* **54**: 915–919.

- Melvin J.E., Koek L., and Zhang G.H. (1991). A capacitative  $\text{Ca}^{2+}$  influx is required for sustained fluid secretion in sublingual mucous acini. *Am. J. Physiol. Gastrointest. Liver Physiol.* **261**: G1043–G1050.
- Nathanson M.H., Fallon M.B., Padfield P.J., and Maranto A.R. (1994). Localization of the type 3 inositol 1,4,5-trisphosphate receptor in the  $\text{Ca}^{2+}$  wave trigger zone of pancreatic acinar cells. *J. Biol. Chem.* **269**: 4693–4696.
- Thorn P, Lawrie A.M., Smith P.M., Gallacher D.V., and Petersen O.H. (1993). Local and global cytosolic  $\text{Ca}^{2+}$  oscillations in exocrine cells evoked by agonists and inositol trisphosphate. *Cell* **74**: 661–668.
- Tojyo Y., Tanimura A., and Matsumoto Y. (1997). Imaging of intracellular  $\text{Ca}^{2+}$  waves induced by muscarinic receptor stimulation in rat parotid acinar cells. *Cell Calcium* **22**: 455–462.
- Tsunoda Y., Stuenkel E.L., and Williams J.A. (1990). Characterization of sustained  $[\text{Ca}^{2+}]_i$  increase in pancreatic acinar cells and its relation to amylase secretion. *Am. J. Physiol. Gastrointest. Liver Physiol.* **259**: G792–G801.